Analysis of Square Spirals on

Planar Dielectric and Chiral Slabs

Ph. D. Thesis

in

Electrical and Electronics Engineering

University of Gaziantep

Supervisor

Prof. Dr. Savaş UÇKUN

By

Kemal DELİHACIOĞLU

FEBRUARY 2007

T.C.
GAZİANTEP UNIVERSITY
GRADUATE SCHOOL OF
NATURAL & APPLIED SCIENCES
ELECTRICAL AND ELECTRONICS ENGINEERING DEPARTMENT

Name of the thesis: Analysis of Square Spirals on Planar Dielectric and Chiral Slabs
Name of the student: Kemal DELİHACIOĞLU
Exam date: February 12, 2007

Approval of the Graduate School of Natural and Applied Sciences

Prof. Dr. Sadettin ÖZYAZICI
Director

I certify that this thesis satisfies all the requirements as a thesis for the degree of Doctor of Philosophy.

Assoc. Prof. Dr. Gülay TOHUMOĞLU
Head of Department

This is to certify that we have read this thesis and that in our opinion it is fully adequate, in scope and quality, as a thesis for the degree of Doctor of Philosophy.

Prof. Dr. Savaş UÇKUN
Supervisor

Examining Committee Members

Prof. Dr. Haluk TOSUN   _____

Prof. Dr. A. Hamit SERBEST   _____

Prof. Dr. L. Canan DÜLGER   _____

Prof. Dr. Savaş UÇKUN   _____

Assist. Prof. Dr. Gölge ÖĞÜCÜ   _____

ABSTRACT

ANALYSIS OF SQUARE SPIRALS ON
PLANAR DIELECTRIC AND CHIRAL SLABS

DELİHACIOĞLU, Kemal
Ph. D. in Electrical and Electronics Engineering
Supervisor: Prof. Dr. Savaş UÇKUN
February 2007, 104 Pages

In this thesis, the scattering characteristics of novel Frequency Selective Surfaces (FSSs) such as, L–shaped, One– and Two–turn square spiral elements are investigated theoretically on planar dielectric and chiral slabs for Transverse Electric (TE) and Transverse Magnetic (TM) incident plane waves. Assuming it to be infinitely thin and a perfect conductor, the FSS elements are placed periodically in the x–y plane. The Moment Method (MM) of Galerkin type is employed by expanding the current induced on the metallic surfaces in terms of overlapping Piecewise Sinusoidal (PWS) basis functions. The reflection and transmission coefficients due to FSS structures are obtained in terms of current coefficients.

The numerical results of reflection and transmission coefficients are plotted against frequency for freestanding and dielectric backed FSS elements. The variation of reflection coefficient with respect to frequency is presented for different values of parameters such as incident angle, slab thickness and dielectric constant. The co– and cross–polarized field equations due to chiral medium are written separately for TE and TM incident waves. The co– and cross–polarized reflection and transmission coefficients are plotted with respect to frequency for different values of medium parameters such as chirality admittance, slab thickness, incident angle and dielectric constant. At resonant frequency a maximum current is excited on the elements; for this reason, the current amplitude induced on the metallic FSSs is plotted against the stretched out wire length at resonant frequency.

Key words: Chiral, Frequency Selective Surface, Moment Method, Piecewise Sinusoidal, L–shaped, one–turn square spiral and two–turn square spiral.

ÖZET

DÜZLEMSEL DİELEKTRİK VE BAKIŞIMSIZ LEVHALAR ÜZERİNDEKİ KARE HELEZONLARIN ANALİZİ

DELİHACIOĞLU, Kemal
Doktora Tezi Elektrik Elektronik Mühendisliği Bölümü
Tez Yöneticisi: Prof. Dr. Savaş UÇKUN
Şubat 2007, 104 Sayfa

Bu tezde, L–şekilli, tek ve çift döngülü kare helezon gibi yeni Frekans Seçici Yüzey (FSY)' lerin saçılma karakteristikleri düzlemsel dielektrik ve bakışımsız levhaya dik gelen TE ve TM düzlem dalgaları için araştırılmıştır. Sonsuz ince ve mükemmel iletken kabul edilen FSY elemanları x–y düzlemine periyodik olarak yerleştirilmiştir. Metal yüzeylerde indüklenen bilinmeyen akım katsayıları üst üste çakışan parçalı sinüs temel fonksiyonları cinsinden genişletilip Galerkin tipi Moment Metodu kullanılmıştır. FSY yapılarından dolayı oluşan yansıma ve iletim katsayıları akım katsayıları cinsinden elde edilmiştir.

Havada asılı ve dielektrik levha ile desteklenen FSY elemanları için yansıma ve iletim katsayılarının frekansa göre grafikleri çizilmiştir. Yansıma katsayısının frekansa göre değişimi gelme açısı, levha kalınlığı ve dielektrik sabiti gibi parametrelerin farklı değerleri için sunulmuştur. Bakışımsız ortamdan dolayı, ortak– ve çapraz–kutupsal alan denklemleri TE ve TM düzlem dalgaları için elde edilmiştir. Ortak– ve çapraz– kutupsal yansıma ve iletim katsayılarının frekansa göre grafikleri ortamın bakışımsızlık admitansı, levha kalınlığı, gelme açısı ve dielektrik sabiti gibi farklı değerleri için çizilmiştir. Rezonans frekansında FSY elemanları üzerinde maksimum akım oluştuğundan dolayı metalik FSY'ler üzerinde indüklenen akımın grafiği iletkenin uzunluğuna göre rezonans frekansında çizilmiştir.

Anahtar Kelimeler: Bakışımsız, Frekans Seçici Yüzey, Moment Metod, Parçalı sinüs, L–şekilli, tek–döngülü kare helezon ve çift–döngülü kare helezon.

ACKNOWLEDGEMENTS

I would like to thank my supervisor Prof. Dr. Savaş UÇKUN and Prof. Dr. Tuncay EGE for their guidance and support throughout the study. I am very grateful their encouragement and motivation.

I also thank my family for their patience and support throughout the study.

TABLE OF CONTENTS

LIST OF FIGURES

NOMENCLATURE

List of Abbreviations

EFIE   Electric Field Integral Equation

FSS   Frequency Selective Surface

LCP   Left Circularly Polarized

MM   Moment Method

PWS   Piecewise Sinusoidal

RCP   Right Circularly Polarized

TE   Transverse Electric

TM   Transverse Magnetic

List of Symbols

F The vector Floquet mode function

p, q Indices for the location of elements (modes)

A Periodic cell area

$\boldsymbol{k}_{pq}$ Transverse propagation vector

ρ Position vector in the x–y plane

$\boldsymbol{\kappa}_{rpq}$ Unit vectors representing TM and TE waves

$\gamma_{pq}^{o}, \gamma_{pq}$ The modal propagation constants for the air and dielectric region

θ_i, ϕ_i Angle of incidence in spherical coordinates

$\varepsilon_o, \varepsilon$ Permittivity of free space and dielectric slab

ε_r Relative permittivity of dielectric or chiral slab

μ_o, μ Permeability of free space and dielectric slab

k_o, k Wave number of free space and dielectric slab

ω Angular frequency

$\boldsymbol{a}_x, \boldsymbol{a}_y, \boldsymbol{a}_z$ Unit vectors along the x–, y–, and z– axis

d	Thickness of the dielectric slab
d_1, d_2	Lattice vectors in x– and y– directions
β	Angle between lattice vectors
$\boldsymbol{E}_t^{inc}, \boldsymbol{H}_t^{inc}$	Total transverse incident electric and magnetic fields
R_{rpq}^{slab}	Reflection coefficient from dielectric slab
Y_o, Y	Admittances of free space and dielectric slab
Y_{rpq}^o, Y_{rpq}	Modal admittances for air and dielectric regions
Y_{rpq}^{eq}	Equivalent modal admittances
R_{rpq}	Reflection from the interface at z=d
$\boldsymbol{E}_t^-, \boldsymbol{H}_t^-$	Transverse electric and magnetic fields propagating in –z direction for z<0
$\boldsymbol{E}_t, \boldsymbol{H}_t$	Transverse electric and magnetic fields in dielectric slab
$\boldsymbol{E}_t^+, \boldsymbol{H}_t^+$	Transverse electric and magnetic fields propagating in +z direction for z>d
$a_{rpq}^-, a_{rpq}, b_{rpq}, b_{rpq}^+$	Unknown amplitudes for the electric field vectors
$\boldsymbol{J}(x, y)$	Current density
$\boldsymbol{f}_n(x, y)$	Expansion (basis) functions
w	Width of the square spiral
h_i	Length of the i'th segment
ξ	Chirality admittance of chiral slab
$k_{r,l}$	Wave numbers of RCP and LCP waves
$\gamma_{pq}^{r,l}$	Propagation constants of RCP and LCP waves
Y_{1pq}, Y_{2pq}	Modal admittances for TM and TE waves
$Y_{1pq}^{r,l}, Y_{2pq}^{r,l}$	TM and TE modal admittances for RCP and LCP waves
$\boldsymbol{E}_{inc}^{TM,TE}$	Total incident electric field to chiral slab
$E_o^{TM,TE}$	Magnitude of incident electric field for TM and TE waves
$\boldsymbol{E}, \boldsymbol{H}$	Electric and magnetic fields in chiral medium

$\boldsymbol{E}_2^{\pm}$ Sum of RCP and LCP electric fields in chiral medium propagating in +z and –z directions

$E_{100}^{TM}, E_{200}^{TE}$ Amplitude of co–polarized reflected waves from a chiral slab without FSS elements

$e_{100}^{TM}, e_{200}^{TE}$ Amplitude of cross–polarized reflected waves from a chiral slab without FSS elements

$E_{300}^{TM}, E_{300}^{TE}$ Amplitude of co–polarized transmitted waves from a chiral slab without FSS elements

$e_{300}^{TM}, e_{300}^{TE}$ Amplitude of cross–polarized transmitted waves from a chiral slab without FSS elements

$\boldsymbol{E}_{r1}, \boldsymbol{E}_{r2}$ Scattered reflected electric fields from chiral slab in region z<0

$\boldsymbol{E}_{t1}, \boldsymbol{E}_{t2}$ Scattered transmitted electric fields from chiral slab in region z>d

R_{co}^{TM}, T_{co}^{TM} Co–polarized reflection and transmission coefficients of chiral slab for TM wave

R_{cr}^{TE}, T_{cr}^{TE} Cross–polarized reflection and transmission coefficients of chiral slab for TM wave

R_{co}^{TE}, T_{co}^{TE} Co–polarized reflection and transmission coefficients of chiral slab for TE wave

R_{cr}^{TM}, T_{cr}^{TM} Cross–polarized reflection and transmission coefficients of chiral slab for TE wave

INTRODUCTION

The aim of this thesis is to investigate the reflection, transmission and resonance characteristics of novel square spiral Frequency Selective Surface (FSS) elements placed periodically on a chiral slab. First, square spiral element was reduced to sub–structures such as strip, L–shaped and one–turn square spiral elements, to go step by step. Later, we ended with a two–turn square spiral element. Adding more turn to square spiral will increase the inter–element spacings and the matrix dimension; however this is time consuming and more basis functions should be used. These FSS structures are analyzed on both planar dielectric and chiral slabs. The most important thing for square spiral element is to find suitable basis functions that will represent unknown current coefficients. The entire domain or subdomain basis functions are used to find surface currents in most of the FSS problems comprised of simple structures. It is difficult to find an entire domain basis functions for complex structures, i.e. two–turn or many–turn square spiral. Throughout this thesis the Moment Method (MM) of overlapping Piecewise Sinusoidal (PWS) basis functions are used to determine the unknown current coefficients. Since the square spiral is a curved structure, the PWS basis function at the corners is divided into two equal parts; one is in the vertical segment and the other is in the horizontal segment. Having computed the unknown current coefficients, the reflected and transmitted waves can readily be found.

Literature Review

The periodic structures constituted by metallic elements, which is called FSSs, have been studied for many years and their behavior is well known. The FSS elements can be either free standing or printed on a dielectric slab. The dielectric slab is used to support FSS elements and modify spectral response characteristics. FSSs for microwave systems are commonly fabricated in printed circuit technology where

the selectivity is determined by the shape and spacing of elements within the array of conducting elements. FSSs also depend on the constitutive parameters of the slab, angle of incidence and polarization of the incoming wave. FSSs have found wide use in various applications. They are designed to reflect or transmit electromagnetic waves with frequency discrimination. Scattering from the perfectly conducting arrays of different FSS structures have been analyzed and reported by many authors i.e. band stop filters, band pass filters, microwave multiband antennas, hybrid radomes, dichroic subreflectors [1,2,3]. Theoretical and experimental investigations on arrays of elements of different shapes such as dipole [4], crossed dipoles [5], tripoles [6], square loops [7], Jerusalem cross [8] and patch [9] have been carried out earlier. Some other applications of FSSs have been proposed in literature; for instance, millimeter and sub millimeter wave applications [10], spaceborne applications of reflector antenna [11], dual reflector antenna systems in order to provide multi–frequency capabilities [12], rectangular patch FSS mounted on uniaxial anisotropic substrate [13], in dielectric radomes design to reduce reflections [3]. The circular ring FSS elements both double screen and single screen designs are generated for tri–band system that reflects the X–band signal while transmitting through the S– and Ku–band signals [14]. In antenna and microwave filter applications, periodic arrays of conducting elements are also used for Photonic Bandgap structures which prohibit the electromagnetic wave propagation within a certain frequency range [15].

Chiral media are known as optically active media. The special property of optically active media is that the polarization plane of linearly polarized electromagnetic wave is rotated as wave passes through the medium. The amount of rotation depends on the distance traveled by the wave in the medium and on the difference between the two wave numbers, which is a consequence of the degree of chirality [16]. The optical activity of the chiral medium is commonly represented by a scalar parameter, ξ, which is called chirality admittance of the medium [17]. Chiral materials have a great importance in electromagnetic field applications with ongoing progress. A considerable amount of experimental and analytical works have been devoted to the application of chiral materials over the last couple decades [18]. In microwave and antenna engineering, chiral materials can be used to build novel devices and structures such as, polarization transformers [19], reduction of target

radar cross–section RCS [20], periodic achiral–chiral interfaces [21], chirowaveguides [22], anti–reflection coatings [23], microstrip antennas [24], chiro–phase shifter [25] and chiral absorbing material [26]. FSS elements, comprised of periodically arranged metallic structures of dipole, cross dipole, square patch, circular and square rings on a chiral slab are analyzed in [27].

The present thesis gives the results of three novel FSSs which are made up of perfectly conducting elements of L–shaped, one– and two–turn square spirals placed periodically on planar dielectric and chiral slabs. The unknown current induced by the incident wave on the metallic FSSs can be found by expanding the current density in terms of overlapping PWS basis functions [28] and then using the MM [29] of Galerkin type. In [28], the numerical analysis algorithm for the square spiral antennas is developed by expanding the current distribution in PWS basis function. A computer program is developed to find the reflection and transmission coefficients due to dielectric and chiral backed FSS elements. The results are presented in graphical form for the current amplitude, reflection and transmission coefficients.

Thesis Overview

The presentation of the work done in this thesis is organized as follows: Chapter 1 gives the necessary equations corresponding to electric and magnetic fields derived for the FSS elements on planar dielectric slab. The detailed analyses of MM and PWS basis functions are given. The Electric Field Integral Equation (EFIE) is obtained using the boundary conditions and the inner products with the use of overlapping PWS basis functions. The reflection and transmission coefficients are plotted with respect to frequency for freestanding and dielectric backed FSSs at different values of medium parameters. The current amplitude versus stretched out length is plotted at resonant frequency of the three FSS elements.

Chapter 2 is devoted to the L–shaped, one– and two–turn square spiral FSS elements backed by chiral slab. The necessary electric and magnetic fields are written in terms of the modal fields [30] for the chiral slab and free spaces

corresponding to TE and TM wave incidences. The co– and cross–polarized reflection and transmission coefficients are obtained in terms of the induced current coefficients and medium parameters for the propagating modes. The co– and cross–polarized reflection and transmission coefficients are plotted with respect to frequency for FSS elements of strip, L–shaped, one– and two–turn square spirals. The current coefficients induced on the conductors are plotted against the stretched out length of the structure at resonant frequency.

Finally, in Chapter 3, conclusions and recommendations for additional work are proposed. In the appendix the full expressions for the coefficients of TM and TE wave on a chiral slab are given.

CHAPTER 1

DIELECTRIC BACKED FSSs

1.1 Introduction

The focus of this dissertation is to investigate the reflection, transmission and resonance characteristics of L–shaped, one– and two–turn square spiral FSSs placed periodically on x–y plane and composed of infinitely thin electrical conductors, backed by planar dielectric and chiral slabs. Firstly, we analyzed dielectric backed FSS by using Modal analysis method with the PWS basis functions MM. The dielectric and chiral slabs are placed between two free spaces, with infinite transverse dimensions on either side. The FSS array is illuminated by a monochromatic plane wave of arbitrary polarization (either TM or TE incident) from the free space region. The amplitude of the incident electric field is set to unity (1 V/m). The periodicities (inter–element spacing) d_1 and d_2 are in the x– and y– directions, respectively. The slab has a thickness d and a relative permittivity ε_r. The Modal analysis method was applied to expand the scattered field as a summation of modes near the array of perfect conductor with unknown coefficients, where each mode satisfies Floquet's Theorem [31]. By requiring the total electric field vanish on the conducting element, an integral equation for the unknown current on each element is obtained. This integral equation can be solved by using MM converting the integral equation into simultaneous linear equation through numerical approximations, and into a matrix equation that can be solved numerically on computer by matrix inversion. In the MM, we expand the unknown currents into finite series in terms of basis functions. There are two classes of basis functions. The first class is defined over the entire solution domain and hence is called the entire–domain basis functions. For most electromagnetic problems, the solution domain is complicated, and it is difficult to find entire–domain basis functions that can form approximately a complete set over the domain. For this reason, the entire–domain basis functions have limited use. The second class is defined over small parts of the solution domain and is called the subdomain basis functions. Although the unknown function over the entire solution domain can be complicated and cannot be represented by simple functions, its
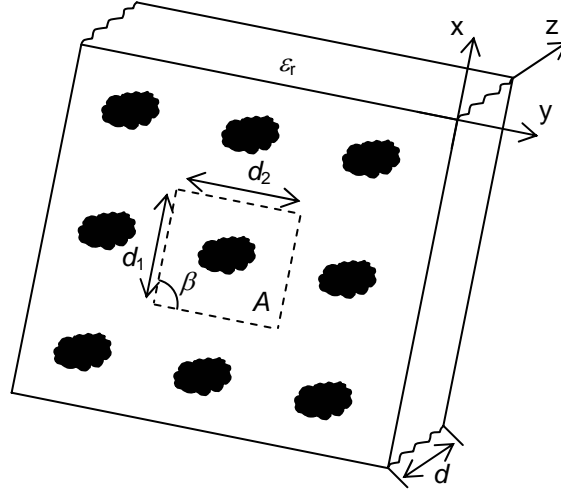
Figure 1.1 FSSs composed of infinite doubly periodic arbitrary conductors printed on a dielectric slab

behavior over a sufficiently small region can be rather simple and hence is representable with simple functions. For this reason, the subdomain basis functions are widely used in the MM for a variety of electromagnetic problems. In the solution domain of this thesis, the basis (expansion) function was chosen as PWS when implementing the MM to determine the reflection and transmission coefficients which depend on the current coefficients.

1.2 Analysis of FSSs Backed by Dielectric Slab

The dielectric slab is assumed to be linear, isotropic and homogeneous. All the elements in the array are assumed to be identical, infinitely thin and perfectly conducting. The array is periodic and extends to infinity in both the x– and y– directions. This allows us to expand the fields in three regions, i.e., inside the dielectric slab and in the air on either side, into Floquet modes. The Floquet mode theorem provides a means of describing the array in terms of complete orthogonal set of modes so that mutual coupling between the array elements is taken into account. The incident field, i.e., the field produced by the incident plane wave in the absence of scatterers, is just the field produced by the incident wave in the presence of dielectric slab. It therefore contains only the zero order Floquet modes. Scattered fields, on the other hand, are produced by the current distribution $\mathbf{J}(x, y)$ on the scatterers. It is assumed that a monochromatic plane wave of arbitrary polarization, with unity electric field intensity is incident from free space upon a dielectric slab.

6

Arbitrary periodic excitations can be studied by decomposing the incident field into its TE and TM components and then further decomposing each component into its Floquet expansion. When expanding the fields, we recognize that we can use the vector Floquet modes with the $e^{j\omega t}$ time dependence omitted:

$$\boldsymbol{F}_{rpq} = A^{-1/2} e^{-j\boldsymbol{k}_{pq}\cdot\boldsymbol{\rho}} e^{-j\gamma_{pq}z} \boldsymbol{\kappa}_{rpq} \tag{1.1}$$

where $\boldsymbol{F}_{rpq}$ designate the electric and magnetic field at the (p,q)'th periodic cell. The first subscript $r = 1$ or $r = 2$ is used to stand for TM and TE modes, respectively. Throughout this thesis, boldface letters have been used to denote vectors. The vector $\boldsymbol{k}_{pq}$ is the propagation vector along the tangential direction (x–y plane) and it is defined as

$$\boldsymbol{k}_{pq} = \left(k\sin\theta\cos\phi + \frac{2\pi}{d_1}p\right)\boldsymbol{a}_x + \left(k\sin\theta\sin\phi - \frac{2\pi p}{d_1\tan\beta} + \frac{2\pi q}{d_2\sin\beta}\right)\boldsymbol{a}_y \tag{1.2}$$

where $\boldsymbol{\rho} = x\boldsymbol{a}_x + y\boldsymbol{a}_y$ is a vector in the x–y plane and $\{\theta,\phi\}$ are the spherical coordinate angles defining the direction of propagation of the incident field. $\boldsymbol{d}_1$ and $\boldsymbol{d}_2$ are lattice vectors. The area of the unit cell in Figure 1.1 is denoted by A ($A = |\boldsymbol{d}_1 \times \boldsymbol{d}_2| = d_1 d_2 \sin\beta$).

The propagation along the transverse direction (the z–direction) is defined as

$$\gamma_{pq} = \begin{cases} \sqrt{k^2 - |\boldsymbol{k}_{pq}|^2} & k \geq |\boldsymbol{k}_{pq}| \\[2ex] -j\sqrt{|\boldsymbol{k}_{pq}|^2 - k^2} & k \leq |\boldsymbol{k}_{pq}| \end{cases} \tag{1.3}$$

$$k = \omega\sqrt{\varepsilon\mu_o}$$

The explicit definition for the unit vector $\boldsymbol{\kappa}_{rpq}$ is:

$$\boldsymbol{\kappa}_{1pq} = \frac{\boldsymbol{k}_{pq}}{|\boldsymbol{k}_{pq}|}, \qquad \text{TM modes}$$

$$\boldsymbol{\kappa}_{2pq} = \boldsymbol{a}_z \times \boldsymbol{\kappa}_{1pq}, \qquad \text{TE modes} \qquad p,q = -\infty,\cdots,-2,-1,0,1,2,\cdots\infty$$

For $\theta_i = p = q = 0$, $\boldsymbol{k}_{pq} = 0$. In order to avoid a $\dfrac{0}{0}$ singularity when $\theta_i = p = q = 0$, the limit of $\boldsymbol{\kappa}_{rpq}$ must be taken for $\theta_i \to 0$. The result of such a limit is $\boldsymbol{\kappa}_{100} = \cos\phi_i \boldsymbol{a}_x + \sin\phi_i \boldsymbol{a}_y$ and $\boldsymbol{\kappa}_{200} = -\sin\phi_i \boldsymbol{a}_x + \cos\phi_i \boldsymbol{a}_y$. The location of the elements is defined by the indices of arbitrary integers $\{p, q\}$. The modal propagation constant, γ_{pq} is positive real value for propagating modes and negative imaginary for the exponentially decaying (evanescent) modes in (1.3). Rather than using the compact notation of (1.1), we will write the Floquet modes explicitly in order to properly account for the direction of propagation.

The total transverse incident electric and magnetic fields in the region z≤0 in the absence of the scatterers is given by [32],

$$\boldsymbol{E}_t^{inc} = \sum_{r=1}^{2} [e^{-j\gamma_{00}^o z} + R_{r00}^{slab} e^{j\gamma_{00}^o z}] b_r^{inc} e^{-j\boldsymbol{k}_{00}\cdot\boldsymbol{\rho}} \boldsymbol{\kappa}_{r00} \tag{1.4}$$

$$\boldsymbol{H}_t^{inc} = \sum_{r=1}^{2} Y_{r00}^o [e^{-j\gamma_{00}^o z} - R_{r00}^{slab} e^{j\gamma_{00}^o z}] b_r^{inc} e^{-j\boldsymbol{k}_{00}\cdot\boldsymbol{\rho}} \boldsymbol{a}_z \times \boldsymbol{\kappa}_{r00} \tag{1.5}$$

where the subscript t indicates the transverse field component and b_r^{inc} is the amplitude of incident field. The modal admittances of the free space in the region z≤0 and z≥d are given by,

$$Y_{1pq}^o = \frac{k_o Y_o}{\gamma_{pq}^o}, \qquad Y_{2pq}^o = \frac{\gamma_{pq}^o Y_o}{k_o}, \qquad Y_o = \sqrt{\varepsilon_o / \mu_o}, \qquad k_o = \omega\sqrt{\varepsilon_o \mu_o},$$

$$\gamma_{00}^o = \begin{cases} \sqrt{k_o^2 - |\boldsymbol{k}_{00}|^2} & k_o \geq |\boldsymbol{k}_{00}| \\ \\ -j\sqrt{|\boldsymbol{k}_{00}|^2 - k_o^2} & k_o \leq |\boldsymbol{k}_{00}| \end{cases} \qquad \varepsilon_o = \frac{10^{-9}}{36\pi} F/m \qquad \mu_o = 4\pi 10^{-7} H/m$$

where ε_o, μ_o are the permittivity and permeability of the free space. The reflection coefficient, R_{rpq}^{slab} at the boundary at z = 0, due to the dielectric slab is given by

$$R_{rpq}^{slab} = \frac{2Y_{rpq}^o - Y_{rpq}^{eq}}{Y_{rpq}^{eq}} \tag{1.6}$$

where Y_{rpq}^{eq} is the equivalent modal admittance given as

$$Y_{rpq}^{eq} = Y_{rpq}^{o} + Y_{rpq}\left(\frac{1 - R_{rpq}}{1 + R_{rpq}}\right), \quad Y_{1pq} = \frac{kY}{\gamma_{pq}}, \quad Y_{2pq} = \frac{\gamma_{pq}Y}{k}, Y = \sqrt{\varepsilon/\mu}$$

$$R_{rpq} = \left[\frac{Y_{rpq} - Y_{rpq}^{o}}{Y_{rpq} + Y_{rpq}^{o}}\right]e^{-j2\gamma_{pq}d}$$

Equation (1.6) is found in a straightforward manner by matching the tangential electric and magnetic fields at z = 0 and z = d.

The incident wave induces current on the scatterers. Radiation from the current and scattering from the dielectric slab yield the electromagnetic fields. The scattered fields in region $1(z \le 0)$, $2(0 < z < d)$ and $3(z \ge d)$ are represented by $\{E_1, H_1\}$, $\{E_2, H_2\}$ and $\{E_3, H_3\}$, respectively. For z≤0, we have

$$E_1 = \sum_{r=1}^{2}\sum_{p=-\infty}^{\infty}\sum_{q=-\infty}^{\infty}a_{rpq}^{-}e^{j\gamma_{pq}^{o}z}\cdot e^{-j\boldsymbol{k}_{pq}\cdot\boldsymbol{\rho}}\boldsymbol{\kappa}_{rpq} \qquad (1.7)$$

$$H_1 = -\sum_{r=1}^{2}\sum_{p=-\infty}^{\infty}\sum_{q=-\infty}^{\infty}Y_{rpq}^{o}a_{rpq}^{-}e^{j\gamma_{pq}^{o}z}\cdot e^{-j\boldsymbol{k}_{pq}\cdot\boldsymbol{\rho}}(\boldsymbol{a}_z \times \boldsymbol{\kappa}_{rpq}) \qquad (1.8)$$

In the region 0<z≤d,

$$E_2 = \sum_{r=1}^{2}\sum_{p=-\infty}^{\infty}\sum_{q=-\infty}^{\infty}[b_{rpq}e^{-j\gamma_{pq}z} + a_{rpq}e^{j\gamma_{pq}z}]\cdot e^{-j\boldsymbol{k}_{pq}\cdot\boldsymbol{\rho}}\boldsymbol{\kappa}_{rpq} \qquad (1.9)$$

$$H_2 = \sum_{r=1}^{2}\sum_{p=-\infty}^{\infty}\sum_{q=-\infty}^{\infty}Y_{rpq}[b_{rpq}e^{-j\gamma_{pq}z} - a_{rpq}e^{j\gamma_{pq}z}]\cdot e^{-j\boldsymbol{k}_{pq}\cdot\boldsymbol{\rho}}(\boldsymbol{a}_z \times \boldsymbol{\kappa}_{rpq}) \qquad (1.10)$$

For z ≥ d

$$E_3 = \sum_{r=1}^{2}\sum_{p=-\infty}^{\infty}\sum_{q=-\infty}^{\infty}b_{rpq}^{+}e^{-j\gamma_{pq}^{o}z}\cdot e^{-j\boldsymbol{k}_{pq}\cdot\boldsymbol{\rho}}\boldsymbol{\kappa}_{rpq} \qquad (1.11)$$

$$H_3 = \sum_{r=1}^{2}\sum_{p=-\infty}^{\infty}\sum_{q=-\infty}^{\infty}Y_{rpq}^{o}b_{rpq}^{+}e^{-j\gamma_{pq}^{o}z}\cdot e^{-j\boldsymbol{k}_{pq}\cdot\boldsymbol{\rho}}(\boldsymbol{a}_z \times \boldsymbol{\kappa}_{rpq}) \qquad (1.12)$$

where $\boldsymbol{a}_{rpq}^{-}$, b_{rpq}, a_{rpq} and b_{rpq}^{+} are unknown field amplitudes. Each Floquet mode in the scattered fields must satisfy the following boundary conditions;

1. The tangential components of electric and magnetic fields are continuous at z=d,

2. The tangential component of electric field is continuous at z=0,

3. The tangential magnetic field exhibits a jump discontinuity at z=0 and is equal to surface current density $\boldsymbol{J}(x, y)$ which resides on the interface.

The boundary conditions are straightforward at z=d, resulting in,

$$a_{rpq} = R_{rpq} b_{rpq} \tag{1.13}$$

The continuity of electric field at z=0 results in,

$$a_{rpq}^{-} = (1 + R_{rpq}) b_{rpq} \tag{1.14}$$

The third boundary condition on the tangential magnetic field at z=0 is,

$$\boldsymbol{H}_2(x, y, 0) - \boldsymbol{H}_1(x, y, 0) = \boldsymbol{a}_z \times \boldsymbol{J}(x, y) \tag{1.15}$$

Substituting (1.8) and (1.10) into (1.15) and using (1.13) and (1.14), we find

$$-\sum_{p=-\infty}^{\infty} \sum_{q=-\infty}^{\infty} \sum_{r=1}^{2} \left[Y_{rpq}^{o} + Y_{rpq} \left(\frac{1 - R_{rpq}}{1 + R_{rpq}} \right) \right] a_{rpq}^{-} \cdot e^{-j\boldsymbol{k}_{pq} \cdot \boldsymbol{\rho}} \boldsymbol{a}_z \times \boldsymbol{\kappa}_{rpq} = \boldsymbol{a}_z \times \boldsymbol{J}(x, y) \tag{1.16}$$

The challenge is to find the values of the unknown coefficients a_{rpq}^{-}. By taking the inner product on both sides of (1.16) $e^{j\boldsymbol{k}_{uv} \cdot \boldsymbol{\rho}} \boldsymbol{\kappa}_{ruv}$ (where $\{u, v\}$ are arbitrary integers), and integrating both sides of the resulting equation over one periodic cell (using the orthogonality relationship) we obtain the following expression for the coefficients a_{rpq}^{-} in terms of the unknown induced currents.

$$a_{rpq}^{-} = -\frac{1}{A Y_{rpq}^{eq}} \int_{unitcell} \boldsymbol{\kappa}_{rpq} \cdot \boldsymbol{J}(x', y') e^{j\boldsymbol{k}_{pq} \cdot \boldsymbol{\rho}'} dx' dy' \tag{1.17}$$

Hence the scattered tangential electric field for z≤0, can be written explicitly as,

$$\boldsymbol{E}_1 = -\sum_{r=1}^{2} \sum_{p=-\infty}^{\infty} \sum_{q=-\infty}^{\infty} e^{j\gamma_{pq}^{o} z} \cdot e^{-j\boldsymbol{k}_{pq} \cdot \boldsymbol{\rho}} (Y_{rpq}^{eq})^{-1} \cdot \frac{1}{A} \int_{unitcell} \boldsymbol{\kappa}_{rpq} \cdot \boldsymbol{J}(x', y') e^{j\boldsymbol{k}_{pq} \cdot \boldsymbol{\rho}'} dx' dy' \boldsymbol{\kappa}_{rpq} \tag{1.18}$$

Since both the scattered and the incident field satisfy the dielectric boundary conditions, the final boundary condition is that the tangential electric field vanishes over the perfect conductor. Hence

$$\boldsymbol{E}_1(x, y, 0) + \boldsymbol{E}_t^{inc}(x, y, 0) = 0 \tag{1.19}$$

or substituting Equation (1.4) and (1.18) into (1.19), we find explicitly

$$\sum_{r=1}^{2}(1+R_{r00}^{slab})b_r^{inc}e^{-jk_{00}\cdot\rho}\kappa_{r00}=$$

$$\frac{1}{A}\sum_{r=1}^{2}\sum_{p=-\infty}^{\infty}\sum_{q=-\infty}^{\infty}e^{-jk_{pq}\cdot\rho}(Y_{rpq}^{eq})^{-1}\int_{unitcell}\kappa_{rpq}\cdot J(x',y')e^{jk_{pq}\cdot\rho'}dx'dy'\kappa_{rpq} \qquad (1.20)$$

where $\qquad b_1^{inc}=1, \qquad b_2^{inc}=0 \qquad$ for TM incidence,

$$b_1^{inc}=0, \qquad b_2^{inc}=1 \qquad \text{for TE incidence}$$

This is EFIE for the unknown current distribution. The most common method to solve the EFIE is the MM. In the MM, the integral equation for the electromagnetic field is transformed into a simultaneous equation or matrix equation and the unknown quantities such as the surface current on conducting scatterers is evaluated by solving the simultaneous equation numerically. In Equation (1.20) the current density $J(x,y)$ is approximated as follows:

$$J(x,y)=\sum_{n=1}^{N}c_n f_n(x,y) \qquad (1.21)$$

where c_n's are the unknown current coefficients to be determined. The functions $f_n(x,y)$ are complete and orthogonal over a conducting element and N is finite for computability. Substituting (1.21) in (1.20) and integrating over a unit cell after multiplying both sides by $f_m(x,y)$ yields the following system of equations.

$$\sum_{r=1}^{2}(1+R_{r00}^{slab})b_r^{inc}\kappa_{r00}\cdot g_{m00}^{*}=\frac{1}{A}\sum_{n=1}^{N}c_n\sum_{r=1}^{2}\sum_{p=-\infty}^{\infty}\sum_{q=-\infty}^{\infty}\frac{\kappa_{rpq}\cdot g_{mpq}^{*}\kappa_{rpq}\cdot g_{npq}}{Y_{rpq}^{eq}} \qquad (1.22)$$

where m=1,2,…,N and the asterisk denotes the complex conjugate.

$$g_{npq}=\iint f_n \quad e^{jk_{pq}\cdot\rho}\,dxdy \qquad (1.23)$$

where $\qquad k_{pq}\cdot\rho=u_p x+v_{pq}y$

$$u_p=k\sin\theta\cos\phi+\frac{2\pi}{d_1}p \qquad v_{pq}=k\sin\theta\sin\phi-\frac{2\pi p}{d_1}\cot\beta+\frac{2\pi q}{d_2\sin\beta}$$

11
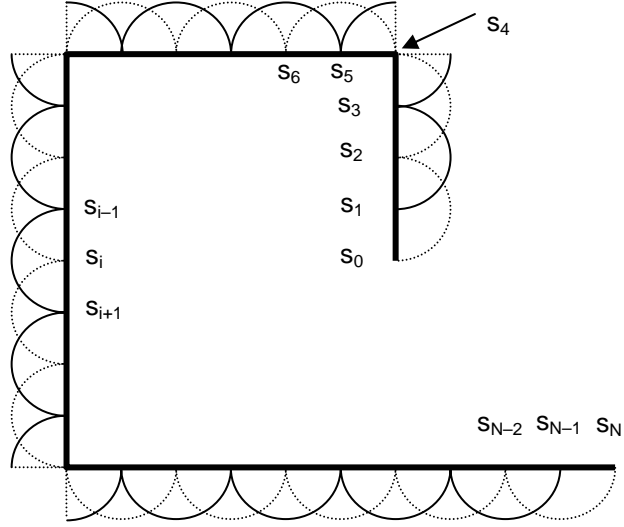
Figure 1.2 Piecewise sinusoidal expansion functions for one–turn square spiral FSS

Since the solution domain is a contour, it can first be divided into small segments, denoted by $s_0, s_1, s_2, \cdots s_N$ as illustrated in Figure1.2 for one–turn square spiral FSS. The basis function $\boldsymbol{f}_n$, is used to approximately represent the surface current which is the overlapping functions of PWS. The basis function in an arbitrary direction $\boldsymbol{a}_s$ is defined in parametric form as

$$\boldsymbol{f}_n(s) = \boldsymbol{a}_s \begin{cases} \dfrac{\sin k(s - s_{n-1})}{\sin k(s_n - s_{n-1})} & s_{n-1} \leq s < s_n \\[3mm] \dfrac{\sin k(s_{n+1} - s)}{\sin k(s_{n+1} - s_n)} & s_n \leq s < s_{n+1} \end{cases} \tag{1.24}$$

The current flows only along the lengths of structures, which is axially directed and only x– or y– dependent. The reference current direction is assumed to be outward from the origin of the structure. The basis and weighting functions will follow the contour of the FSS elements. The width (w) of the square spiral is much smaller compared with the segment length ($w \ll h$) and the wavelength ($w \ll \lambda$). Hence, the variation of the current across the width can be ignored.

Equation (1.22) is a matrix equation of NxN for the unknown coefficients of the current expansion. Substituting (1.23) in (1.22) would yield infinite system of linear equations for the unknown current coefficients. If this infinite system of linear equation is truncated, the solution to the truncated system approximates the exact

12

solution. The truncated linear system can be written in matrix form as;

$$[V_m] = [Z_{mn}] \ [c_n] \tag{1.25}$$

The elements of the impedance matrix are,

$$Z_{mn} = \frac{1}{A} \sum_{p=-\infty}^{\infty} \sum_{q=-\infty}^{\infty} \frac{\boldsymbol{\kappa}_{1pq} \cdot \boldsymbol{g}_{mpq}^* \boldsymbol{\kappa}_{1pq} \cdot \boldsymbol{g}_{npq}}{Y_{1pq}^{eq}} + \frac{\boldsymbol{\kappa}_{2pq} \cdot \boldsymbol{g}_{mpq}^* \boldsymbol{\kappa}_{2pq} \cdot \boldsymbol{g}_{npq}}{Y_{2pq}^{eq}} \tag{1.26}$$

The excitation vector is,

$$[V]_{Nx1} = \left(1 + R_{r00}^{slab}\right) b_r^{inc} \boldsymbol{\kappa}_{r00} \cdot \boldsymbol{g}_{n00} \tag{1.27}$$

The unknown current coefficients are

$$[c]_{Nx1} = [c_1 \quad c_2 \quad \cdots \quad c_N]^T, \text{ with the superscript T denotes transpose.}$$

In Equation (1.26), the matrix that is to be solved is called the moment matrix. The moment matrix is a square matrix with one row and one column for every basis function. Each entry in the moment matrix represents the electromagnetic coupling between two basis functions. For example the moment matrix entry at row one and column two represents the coupling between the first and second basis functions. Typically the computation of the moment matrix entries (filling the matrix) is one of the most time–consuming tasks when using the MM. The size of the matrix equals the number of basis functions used. The matrix is symmetric at normal incidence due to Galerkin's MM. Symmetric means that elements are mirror images of each other across the diagonal of the impedance matrix. The problem is formulated using MM of overlapping PWS basis functions. Since the PWS basis functions are continuous within a segment, the convergence of the results is obtained by increasing the number of Floquet modes until there is little change in the results. With sufficiently large number of Floquet modes the resulting matrix equation is well–conditioned [33]. Equation (1.25) is solved using matrix inversion to calculate the current coefficients for the computation of reflection and transmission coefficients. The total reflected field can be written using (1.4) and (1.18),

$$\boldsymbol{E}_t^{reflected} = \sum_{r=1}^{2} R_{r00}^{slab} e^{j\gamma_{00}^o z} e^{-j\boldsymbol{k}_{00} \cdot \boldsymbol{\rho}} b_r^{inc} \boldsymbol{\kappa}_{r00}$$

$$- \sum_{r=1}^{2} \sum_{p=-\infty}^{\infty} \sum_{q=-\infty}^{\infty} e^{j\gamma_{pq}^o z} e^{-j\boldsymbol{k}_{pq} \cdot \boldsymbol{\rho}} \left[Y_{rpq}^{eq}\right]^{-1} \cdot \frac{1}{A} \int_{unitcell} \boldsymbol{\kappa}_{rpq} \cdot \boldsymbol{J}(x',y') e^{j\boldsymbol{k}_{pq} \cdot \boldsymbol{\rho}'} dx' dy' \boldsymbol{\kappa}_{rpq} \tag{1.28}$$

13

In a straightforward manner we can also find the transmitted field,

$$E_t^{\text{transmitted}} = \sum_{r=1}^{2} e^{-j\gamma_{00}^{o}z} e^{-jk_{00}\cdot\boldsymbol{\rho}} t_{r00}(1+R_{r00}^{\text{slab}})b_r^{\text{inc}}\boldsymbol{\kappa}_{r00}$$

$$-\sum_{r=1}^{2}\sum_{p=-\infty}^{\infty}\sum_{q=-\infty}^{\infty} e^{-j\gamma_{pq}^{o}z} e^{-jk_{pq}\cdot\boldsymbol{\rho}} t_{rpq}\left[Y_{rpq}^{\text{eq}}\right]^{-1}\cdot\frac{1}{A}\int_{\text{unitcell}}\boldsymbol{\kappa}_{rpq}\cdot\boldsymbol{J}(x',y')e^{jk_{pq}\cdot\boldsymbol{\rho}'}dx'dy'\boldsymbol{\kappa}_{rpq} \qquad (1.29)$$

where
$$t_{rpq} = \frac{e^{j(\gamma_{pq}^{o}-\gamma_{pq})d} + R_{rpq}e^{j(\gamma_{pq}^{o}+\gamma_{pq})d}}{1+R_{rpq}}$$

The reflected and transmitted far fields contain only propagating Floquet modes for which γ_{pq} is real. Since the distant scattered fields only consist of zero order $\{p,q\}=\{0,0\}$ propagating Floquet modes, the reflection and transmission coefficients are computed from the following expressions:

$$R = \sum_{r=1}^{2}\left\{R_{r00}^{\text{slab}}b_r^{\text{inc}} - \frac{1}{AY_{r00}^{\text{eq}}}\sum_{n=1}^{N}c_n\boldsymbol{g}_{n00}\cdot\boldsymbol{\kappa}_{r00}\right\}\boldsymbol{\kappa}_{r00} \qquad (1.30)$$

$$T = \sum_{r=1}^{2}\left\{(1+R_{r00}^{\text{slab}})t_{r00}b_r^{\text{inc}} - \frac{t_{r00}}{AY_{r00}^{\text{eq}}}\sum_{n=1}^{N}c_n\boldsymbol{g}_{n00}\cdot\boldsymbol{\kappa}_{r00}\right\}\boldsymbol{\kappa}_{r00} \qquad (1.31)$$

In case of the higher order Floquet modes propagation, it should be included to Equations (1.30) and (1.31). A good FSS design supports only one propagating mode in the same direction as the incident field. To avoid additional modes propagating, we should pay attention to $d_{1,2}(1+\sin\theta_i) < \lambda$, in free space, with $d_{1,2}$ the inter–element spacing and θ_i the angle of incidence. It must be mentioned that while computing the current coefficients of c_n in (1.22), the higher order modes must be included since they are necessary for satisfying boundary conditions. The total current can be expressed as the amount of surface current flowing on FSS structure in the direction of $\boldsymbol{n}\times\boldsymbol{dl}$ is,

$$I_{\text{total}} = \int[\boldsymbol{J}(x,y)\times\boldsymbol{n}]\cdot\boldsymbol{dl} \qquad (1.32)$$

where the normal vector, $\boldsymbol{n} = \boldsymbol{a}_z$ and $\boldsymbol{dl} = \boldsymbol{a}_x dx$ or $\boldsymbol{dl} = \boldsymbol{a}_y dy$.

1.3 Moment Method (MM)

The MM is one of the most popular numerical techniques for solving either open or closed scattering problems. In antenna analysis, the MM is used to convert the EFIE into matrix equation or systems of linear equations. The matrix equation can then be solved for the current coefficients by inverting the matrix, LU decomposition, Gaussian elimination or any other techniques of linear algebra. The basic form of the equation to be solved by the MM is,

$$L(\mathrm{f}) = \mathrm{g} \tag{1.33}$$

where L is a linear operator, f is to be determined (unknown function), and g is the source or forcing function. A crucial point is usually the choice of a suitable basis function set to represent the unknown of the problem. In order to create the matrix equation, the unknown function is defined to be the sum of a set of known independent functions, f_n called basis or expansion functions with unknown amplitudes c_n,

$$\mathrm{f} = \sum_n \mathrm{c_n f_n} \tag{1.34}$$

For exact solutions, (1.34) is usually an infinite summation and f_n form a complete set of basis functions. For approximate solutions, (1.34) is usually a finite summation. Substituting (1.34) in (1.33) and using a linearity of the operator L, we have,

$$\sum_n \mathrm{c_n L(f_n)} = \mathrm{g} \tag{1.35}$$

The unknown amplitudes cannot yet be determined because there are n unknowns, but one functional equation. A fixed set of equations are found by defining independent weighting or testing functions w_m, which are integrated with (1.35) to give m different linear equations. The integration of the weighting functions with (1.35) may be written symbolically as the inner product of the two functions, giving

$$\sum_n \mathrm{c_n} \left\langle \mathrm{w_m}, \mathrm{L(f_n)} \right\rangle = \left\langle \mathrm{w_m}, \mathrm{g} \right\rangle \tag{1.36}$$

where the inner product, $\left\langle a, b \right\rangle$, is defined to be the integral of two functions over the domain of linear operator. Now there are an equal number of unknowns and

independent functions, which allow for the solution of the unknown amplitudes, c_n. The set of equations can be written in matrix form as,

$$[g_m] = [Z_{mn}] \ [c_n] \tag{1.37}$$

where

$$[Z_{mn}] = \begin{bmatrix} \langle w_1, L(f_1) \rangle & \langle w_1, L(f_2) \rangle & \cdots & \langle w_1, L(f_n) \rangle \\ \langle w_2, L(f_1) \rangle & \langle w_2, L(f_2) \rangle & \cdots & \langle w_2, L(f_n) \rangle \\ \vdots & \vdots & \ddots & \vdots \\ \langle w_m, L(f_1) \rangle & \langle w_m, L(f_2) \rangle & \cdots & \langle w_m, L(f_n) \rangle \end{bmatrix} \qquad [c_n] = \begin{bmatrix} c_1 \\ c_2 \\ \vdots \\ c_n \end{bmatrix},$$

$$[g_m] = \begin{bmatrix} \langle w_1, g \rangle \\ \langle w_2, g \rangle \\ \vdots \\ \langle w_m, g \rangle \end{bmatrix} \quad \text{If the matrix Z is nonsingular its inverse exists. The unknown}$$

current coefficients c_n are obtained by $[c_n] = [Z_{mn}]^{-1} [g_m]$.

1.4   Numerical Results

The numerical results are presented for three different FSS element geometries as shown in Figure 1.3. The matrix elements, as given in (1.26), are a doubly infinite summation in Floquet modes p and q. Generally, more basis functions should be included to obtain convergent results. Since the double summation is slowly converging, the convergence of the results is obtained by increasing the number of Floquet modes until there is little change in the results. The numbers of Floquet modes included are $(2M+1)^2$, where M is the index of the highest order Floquet modes. The double infinite sums of Floquet modes, occurring as matrix entries, are truncated over a square matrix of dimension NxN.

For an array consisting of conducting elements under plane wave incidence, a maximum current magnitude is excited on the elements at the array resonant frequency. The current in this case is in phase with the incident field, i.e., the impedance seen by the incident wave is purely ohmic (real), since the capacitive and inductive parts cancel out. At resonance, the magnitude of the current is equal to the real part and the imaginary part is negligible. As a result of the resonance the incident wave is reflected with a phase reversal. Because of this, the currents induced on the FSS elements are plotted at resonant frequency.

16

(a) L–shaped   (b) One–turn square spiral   (c) Two–turn square spiral
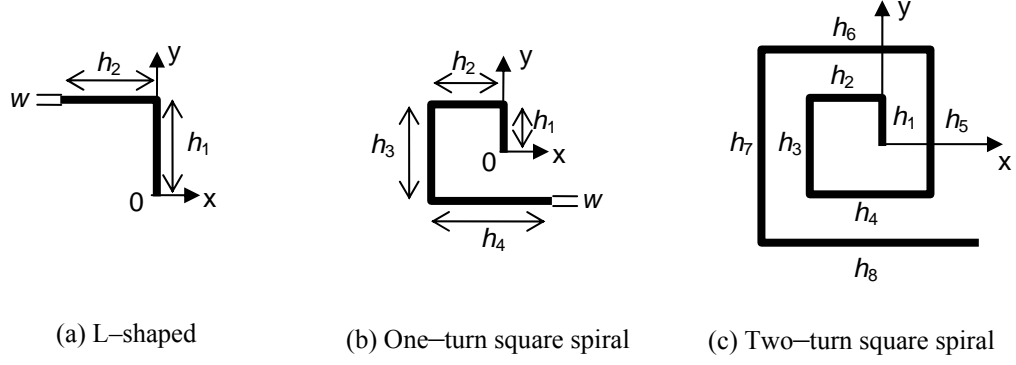
Figure 1.3   L–shaped, One– and Two–turn square spiral scatterers

For the purposes of comparison, numerical results are calculated for the power reflection coefficient versus frequency, for freestanding (d=0 cm and ε_r=1) narrow strip FSS arranged in a square lattice dimension (β=90°). The length and the width of strip are 1.27 cm and 0.127 cm, respectively. The inter–element spacing is d_1=d_2=1.78 cm. The number of basis is 10, which is satisfactory to make a comparison with the experimental results. The comparison of the magnitude of power reflection coefficient versus frequency with that of the measured result (black dots) by Ott et all [4] is almost exact, as given in Figure 1.4. When the field is almost normally incident, θ=1° and ϕ=1°, total reflection (resonance) manifests itself at 11.2 GHz. At resonance (full reflection) the reflection coefficient is equal to unity with a phase of 180°, while at anti–resonance (full transmission) the reflection coefficient must have a magnitude of 0 (zero) with a phase of ±90°. The reflection (R) and transmission (T) coefficients versus frequency for a freestanding and dielectric backed narrow strip FSS are plotted in Figure 1.5. Due to dielectric loading the resonant frequency decreases when the FSS is etched on a dielectric slab. The amount of frequency shift is proportional to the dielectric constant of slab. The plot in Figure 1.6 shows the current amplitude versus length of the narrow strip. As expected the current amplitude is in sinusoidal form.

1.4.1   Numerical Results of L–Shaped FSS Backed by Dielectric Slab

The reflection and transmission coefficients of L–shaped FSS elements on a dielectric slab were first studied by the researcher in [34, 35]. The lengths of L–

shaped FSS elements are $h_1=h_2=0.9$ cm and the width is 0.09 cm. The L–shaped elements are arranged in square lattice. The inter–element spacing are $d_1=d_2=0.93$ cm and the number of basis functions are N=19. The number of included Floquet modes is 361. Figure 1.7 reflection and transmission coefficients for the freestanding and dielectric backed L–shaped FSS have been plotted against frequency at normal incidence. At normal incidence, the reflection and transmission coefficients are the same for both types of polarization. Total reflection (resonance) occurs at 13.4 GHz for L–shaped FSS supported by dielectric slab of 0.1 cm thickness. The L–shaped FSS behaves as a band stop filter in the frequency region of about 10.5 to 16.4 GHz and it is transparent in other frequency regions. Total reflection appears at 15.2 GHz for the freestanding FSS and shifts to 13.4 GHz for dielectric backed FSS elements of L–shaped as shown in Figure 1.7.

The incident electric field induces more current in the parallel arm while it induces less current in the perpendicular arm of the L–shaped FSS. As expected the current amplitude was the same for TE and TM wave incidence for dielectric backed L–shaped FSS, as illustrated in Figure 1.8. In Figure 1.9, the reflection coefficient was plotted for different lengths of L–shaped FSS. The resonant frequency shifts to lower frequency as the length of strip increases. A 0.1 cm increase in strip length approximately causes 2.2 GHz frequency shift for the resonance. The resonant frequency is inversely proportional to the total length of L–shaped FSS elements and the square root of the dielectric constant. The resonant frequencies are 17.4 GHz, 15.2 GHz and 13.4 GHz for the strip lengths of 0.7 cm, 0.8 cm and 0.9 cm, respectively. Figures 1.10 and 1.11 illustrate the reflection coefficient versus frequency for TE and TM waves at different values of incident angles. The resonant frequency is almost stable up to 30° around 13.4 GHz and there is a slight shift in resonance for higher incidences as shown in Figure 1.10 for TE incident wave. The bandwidth of the reflected wave decreases as the incident angle increases for TM incidence as shown in Figure 1.11. For the variation of slab thickness, plotted in Figure 1.12, the resonant frequency is almost stable. Figure 1.13 depicts the reflection coefficient versus frequency for different values of dielectric constant. The resonant frequency shifts to lower frequencies as the dielectric constant increases.
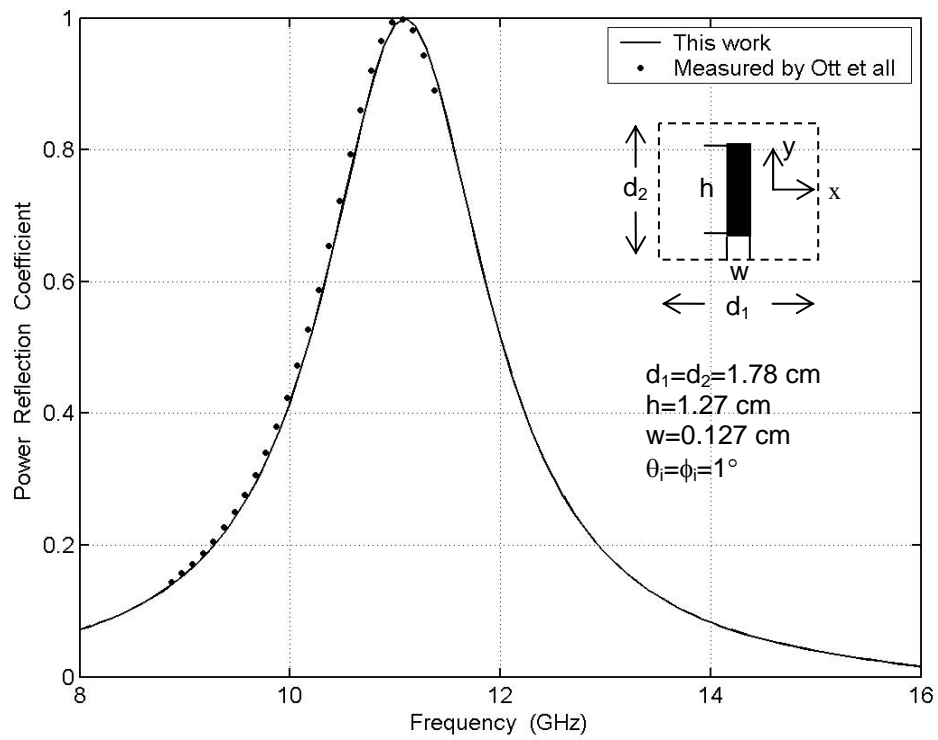
Figure 1.4 Power reflection coefficient versus frequency for the freestanding strip FSS
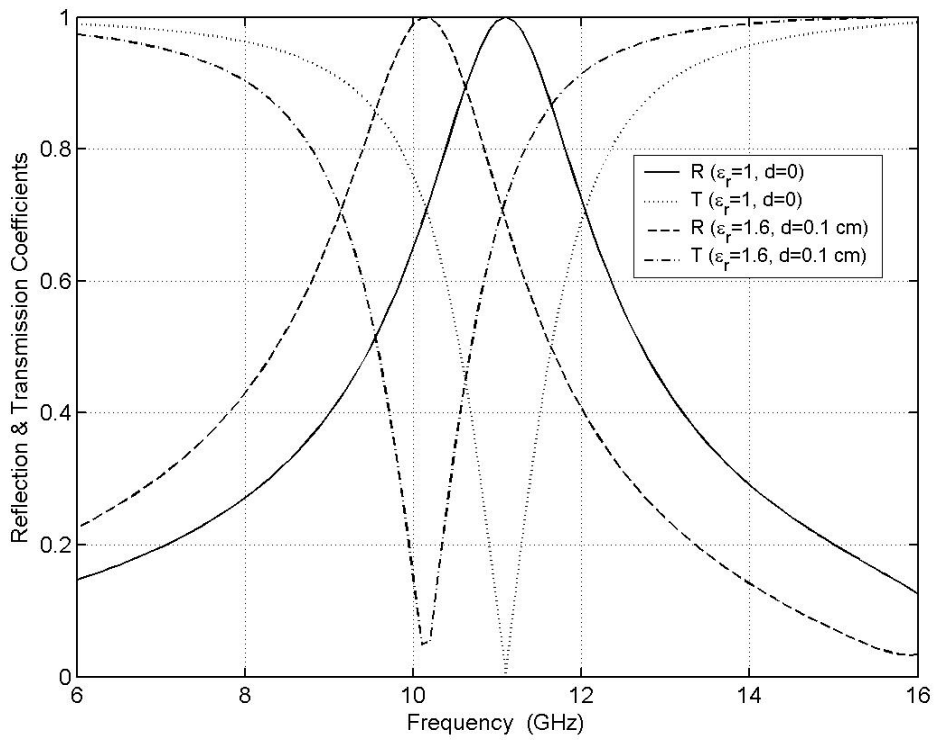
Figure 1.5 TE Reflection and transmission coefficients versus frequency for the freestanding and dielectric backed strip FSS

19
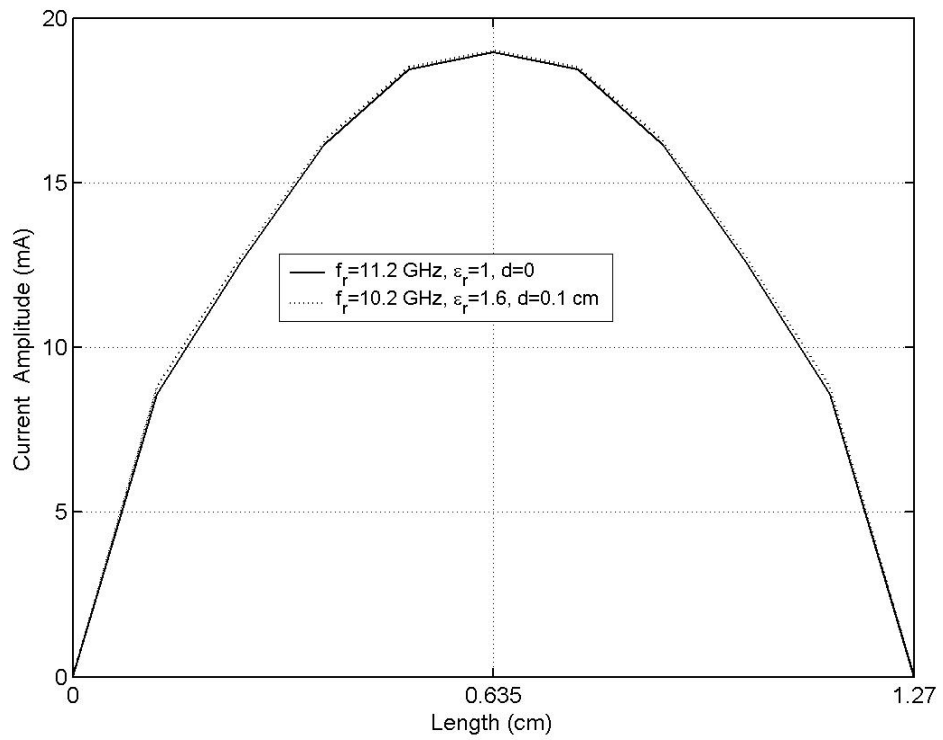
Figure 1.6 Current amplitude versus length for the freestanding and dielectric backed strip FSS at resonance frequency
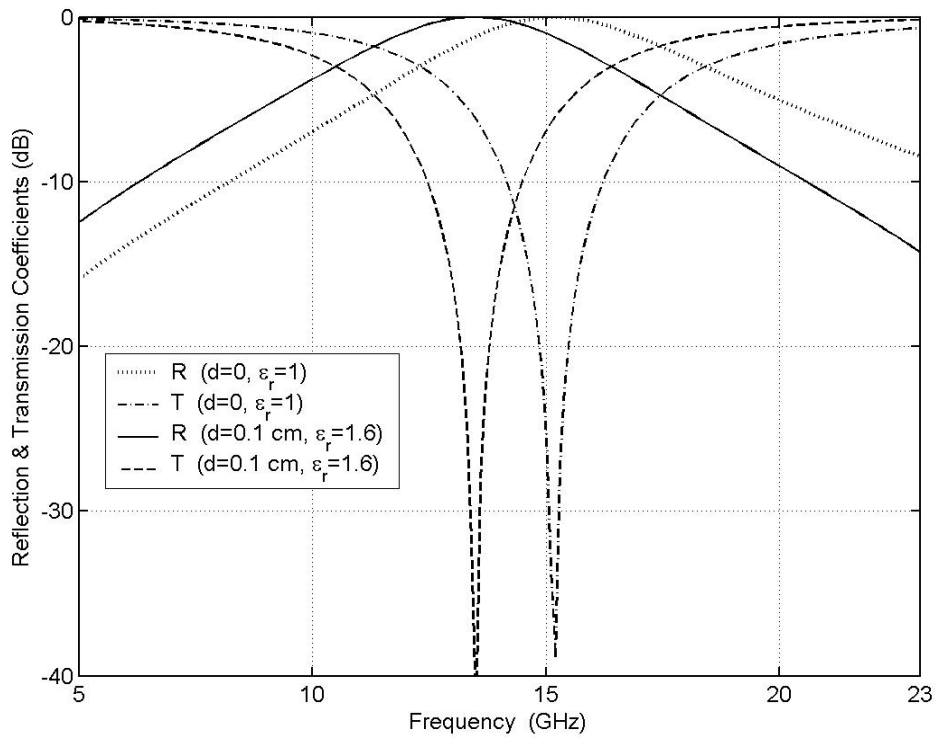
Figure 1.7 Reflection and transmission coefficients for the freestanding and dielectric backed L–shaped FSS $\theta=\phi=0°$, $h_1=h_2=0.9$ cm, $w=0.09$ cm, $d_1=d_2=0.93$ cm

20
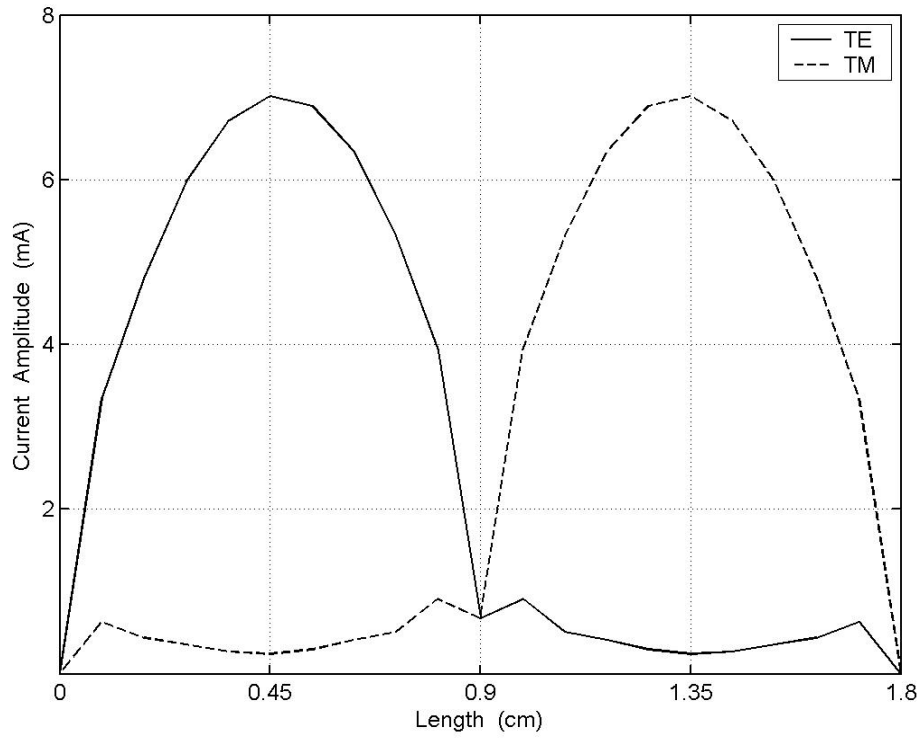
Figure 1.8 Current amplitude versus length for the dielectric backed L–shaped FSS at f_r= 13.4 GHz, $\theta=\phi=0°$, ε_r=1.6, d=0.1 cm, $h_1=h_2$=0.9 cm, w=0.09 cm, $d_1=d_2$=0.93 cm
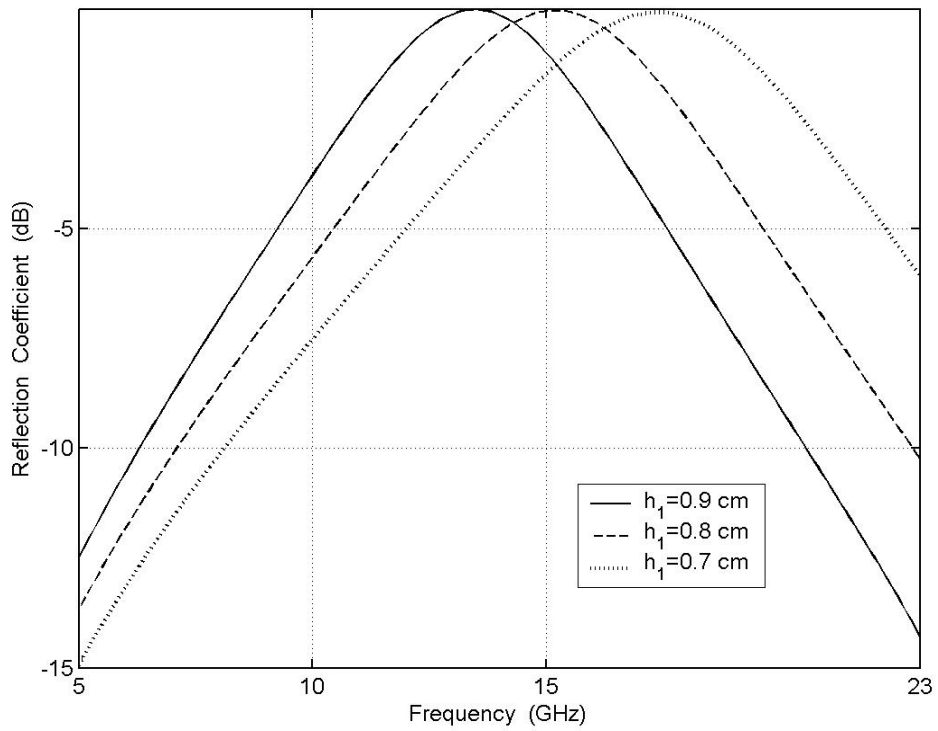
Figure 1.9 Reflection coefficient versus frequency at different lengths of L–shaped FSS; $\theta=\phi=0°$, ε_r=1.6, d=0.1 cm, $w=h_1/10$, $d_1=d_2=h_1$+0.03 cm

21
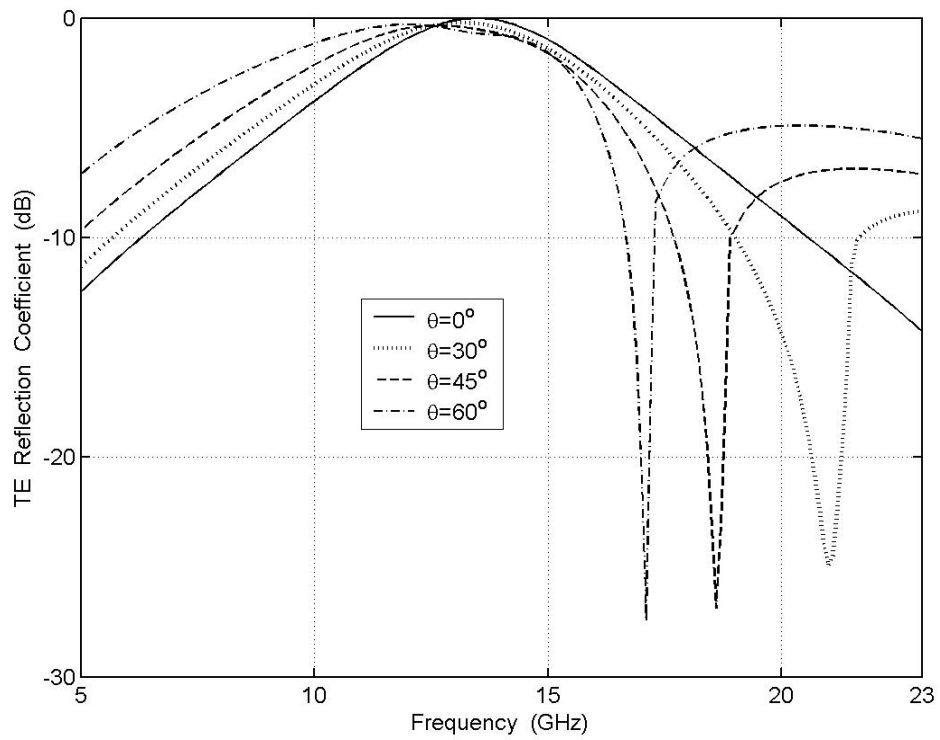
Figure 1.10 TE Reflection coefficient versus frequency for L–shaped FSS at oblique angle incidence
ϕ=0°, ε_r=1.6, d=0.1 cm, h_1=h_2=0.9 cm, w=0.09 cm, d_1=d_2=0.93 cm
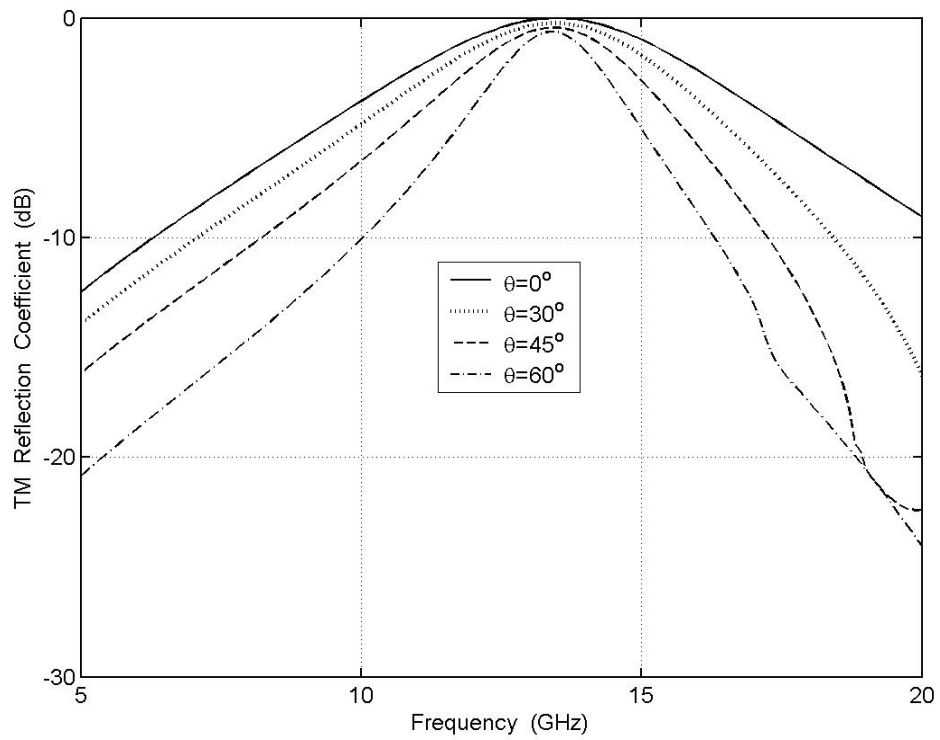
Figure 1.11 TM Reflection coefficient versus frequency for L–shaped FSS at oblique angle incidence
ϕ=0°, ε_r=1.6, d=0.1 cm, h_1=h_2=0.9 cm, w= 0.09 cm, d_1=d_2=0.93 cm

22
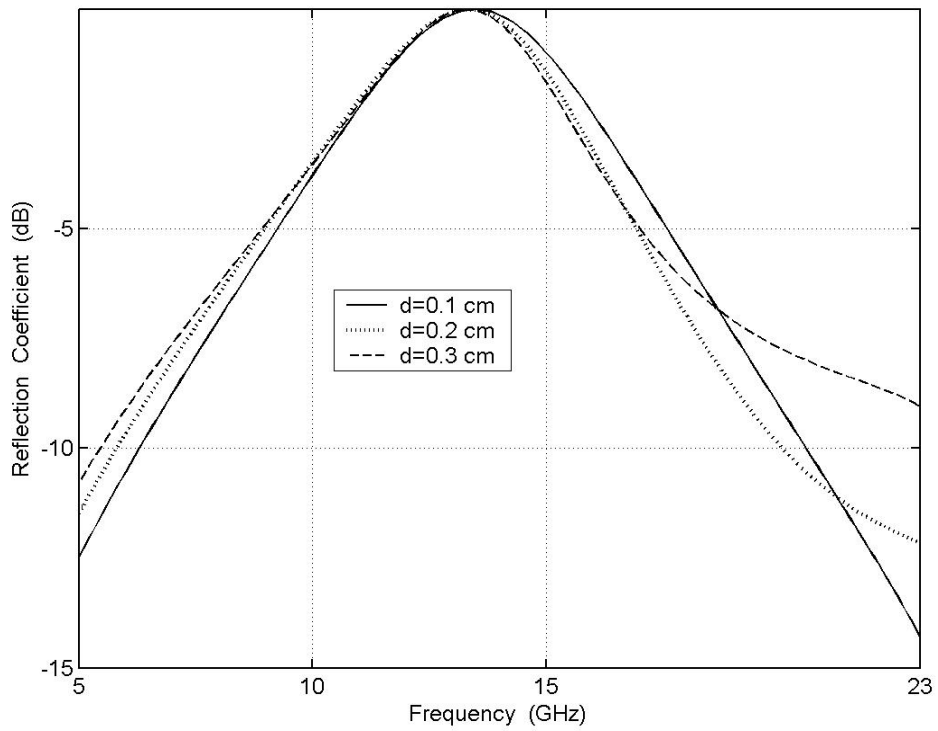
Figure 1.12 Reflection coefficient versus frequency for L–shaped FSS at different slab thicknesses, $\theta=\phi=0°$, $\varepsilon_r=1.6$, $h_1=h_2=0.9$ cm, $w=0.09$ cm, $d_1=d_2=0.93$ cm
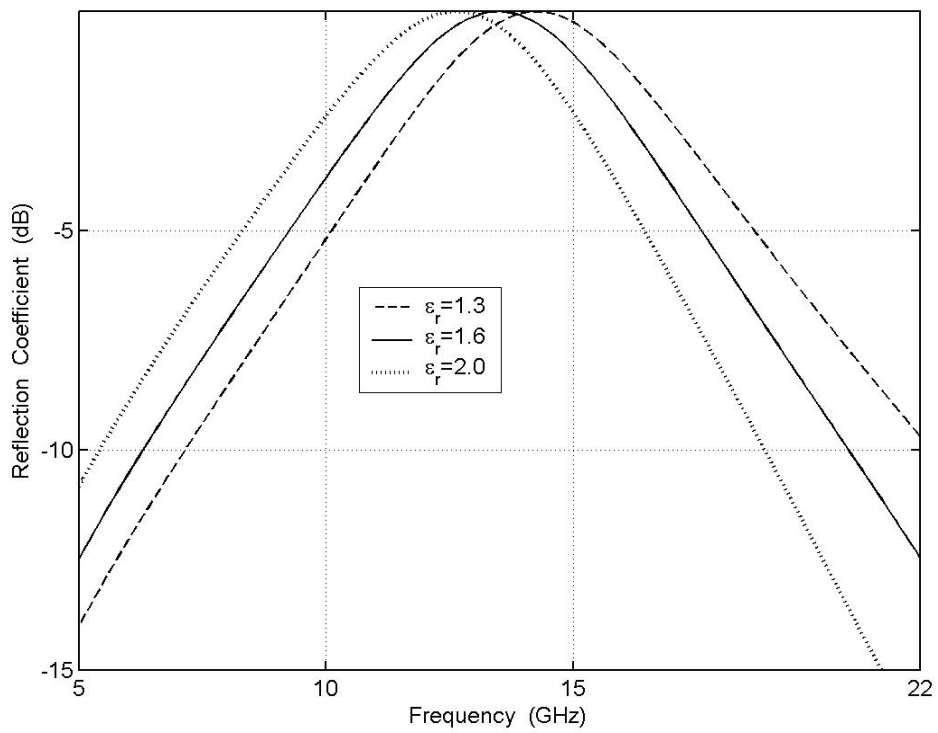
Figure 1.13 Reflection coefficient versus frequency for L–shaped FSS at different values of ε_r, $\theta=\phi=0°$, $d=0.1$ cm, $h_1=h_2=0.9$ cm, $w=0.09$ cm, $d_1=d_2=0.93$ cm

23

1.4.2 Numerical Results of One– and Two–Turn Square Spiral FSSs Backed by Dielectric Slab

The numerical results of one–turn spiral FSS has been presented in Figures 14–23 for TE and TM incident plane waves [35, 36]. The length of the first segment is h_1=0.2 cm and the other lengths can be found from the relation $h_n=2h_1(n-1)$ for $n=2$, 3, 4. The width is chosen as one tenth of the first length ($w=h_1/10$=0.02 cm). The inter–element spacings are equal to 1.55 cm. The number of basis is 25 to estimate the unknown current coefficients. The number of included Floquet modes is 625. The periodic cells are arranged in square lattice (β=90°). In Figure 14, the reflection and transmission coefficients are illustrated for freestanding and dielectric backed FSS at normal incidence for TE incidence. The resonant frequency shifts to lower value when FSS is backed by dielectric slab. The narrow bandwidth is observed for both freestanding and dielectric backed FSS with TE incident wave. The structure behaves as a band stop filter in the frequency region of about 14 to 16 GHz and it is transparent in other frequency regions for dielectric backed FSS. Full transmission (anti–resonance) is observed up to frequency of 13 GHz. Figure 1.15 shows the induced current amplitude variation against overall length of one–turn square spiral FSS. The current induced on the longest parallel segment has a greater peak compared with the current induced on the other segments. Figure 1.16 is depicted for the variation of incident angle. At oblique incidence, the bandwidth is narrower and resonance frequency shifts to lower frequencies. In Figure 1.17 the TE reflection coefficient is plotted for the variation of slab thickness. The slab thickness shifts the resonant to lower frequency and decreases the bandwidth of the reflected wave. As the dielectric constant increases the resonant frequency shifts to lower end as shown in Figure 1.18. As shown in Figure 1.19, the magnitude of the reflected and transmitted waves is plotted with respect to frequency for freestanding and dielectric backed one–turn square spiral FSS at normal incidence of TM plane wave illumination. The structure shows anti–resonance up to 8 GHz. The resonance manifests itself at 11.7 GHz and 10.6 GHz for freestanding and dielectric backed one–turn square spiral FSS structure, respectively. The structure behaves as a band stop filter in the frequency region of about 8 to 12.5 GHz and it is transparent in other frequency regions for dielectric backed FSS. Figure 1.20 illustrates the current

amplitude versus length induced on the one–turn square spiral FSS. The current induced on the last segment has a greater peak and reduces in the other segments. The reflection coefficient versus frequency for the variation of incidence angle is shown in Figure 1.21. The resonant frequency is stable at 10.6 GHz for three different values of incident angles and the bandwidths decrease for increasing values of incident angles. The TM reflection coefficient versus frequency corresponding to slab thickness and dielectric constant variations are shown in Figures 1.22 and 1.23, respectively. In Figure 1.22 the resonant frequency is almost stable for the variation of slab thickness. There is no change in bandwidth of the reflected wave. In Figure 1.23 the increasing value of dielectric constant moves the resonant to lower frequency. The FSS resonates at different frequencies for TE and TM incident waves. The bandwidth of the reflected wave is nearly the same for TE and TM incident waves.
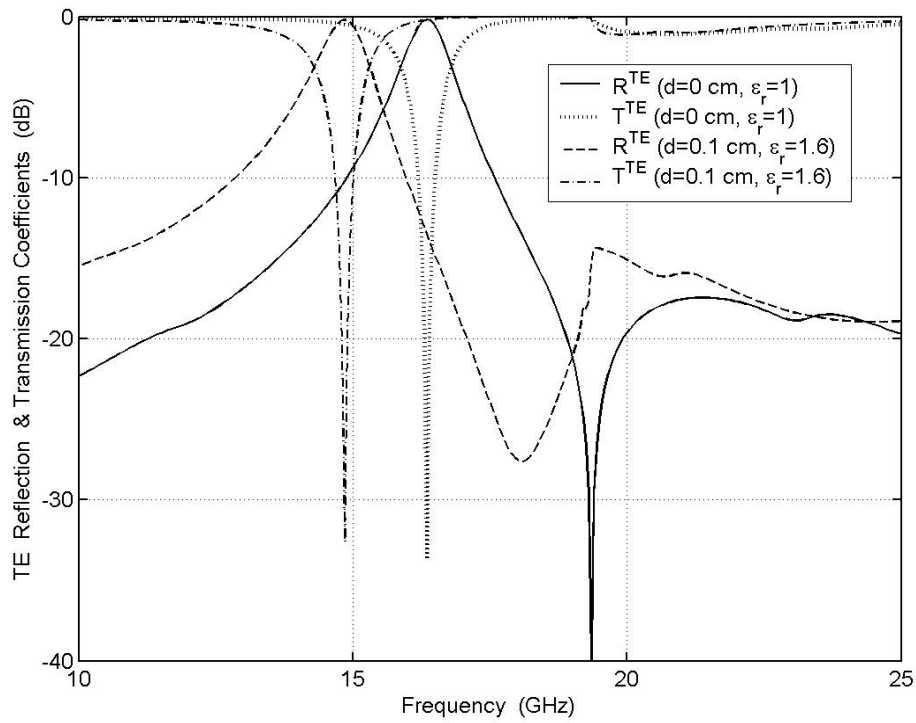
Figure 1.14 TE Reflection and transmission coefficients for freestanding and dielectric backed one–turn square spiral FSS; $\theta=\phi=0°$, $h_1=0.2$ cm, $h_n=2(n-1)h_1$, n=2,3,4., $w=0.02$ cm, $d_1=d_2=1.55$ cm
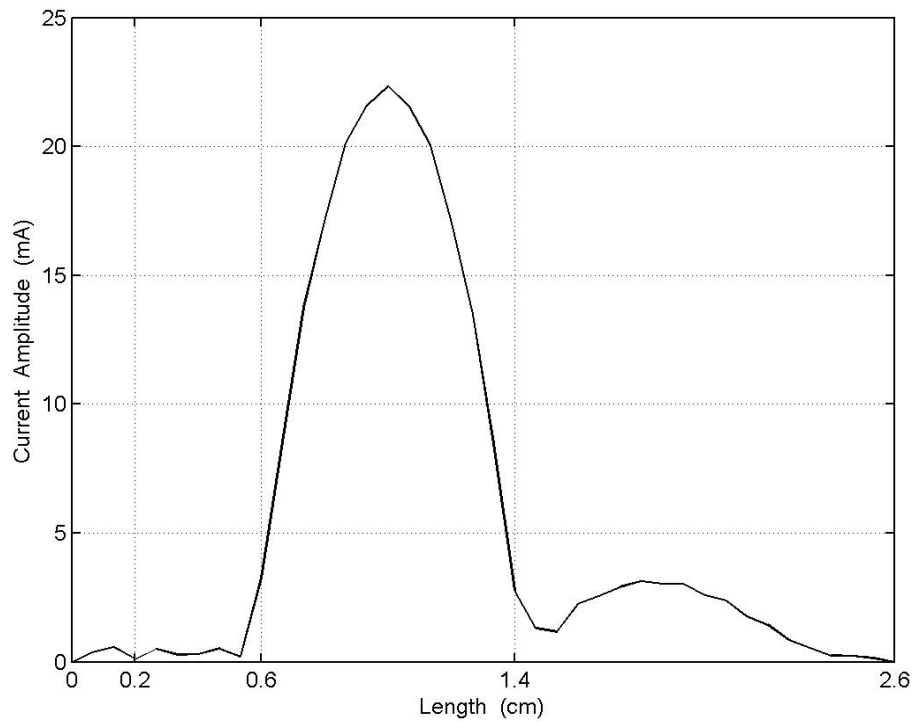
Figure 1.15 TE Current amplitude versus length for dielectric backed one–turn square spiral FSS at $f_r=14.85$ GHz; $\theta=\phi=0°$, $d=0.1$ cm, $\varepsilon_r=1.6$, $h_1=0.2$ cm, $h_n=2(n-1)h_1$, n=2,3,4., $w=0.02$ cm, $d_1=d_2=1.55$ cm

26
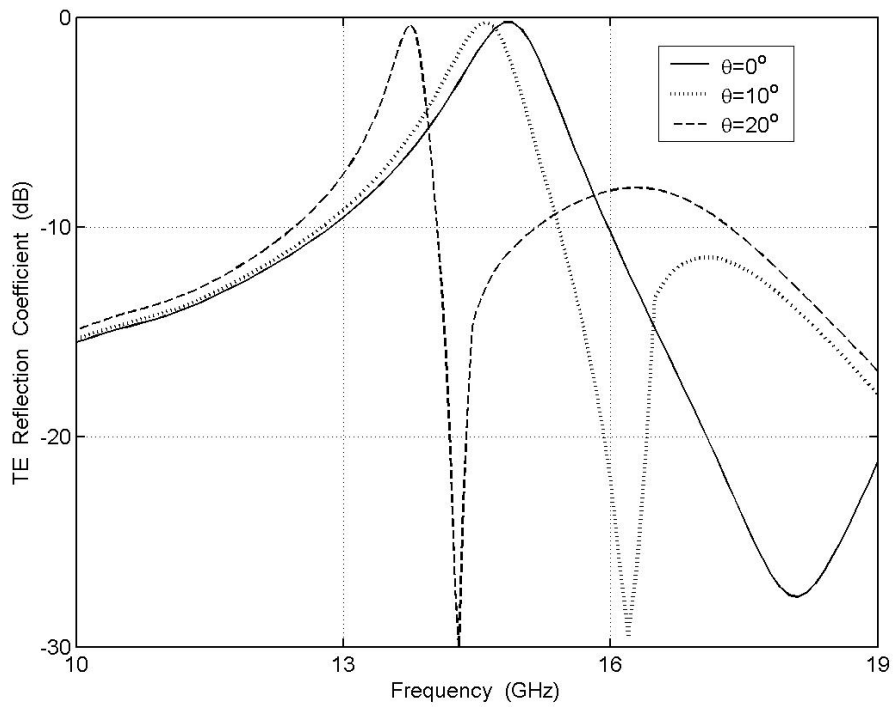
Figure 1.16 TE Reflection coefficient versus frequency for one–turn square spiral FSS at different incident angles; ϕ=0°, d=0.1 cm, ε_r=1.6, h_1= 0.2 cm, h_n=2(n–1)h_1, n=2,3,4., w=0.02 cm, d_1=d_2=1.55 cm
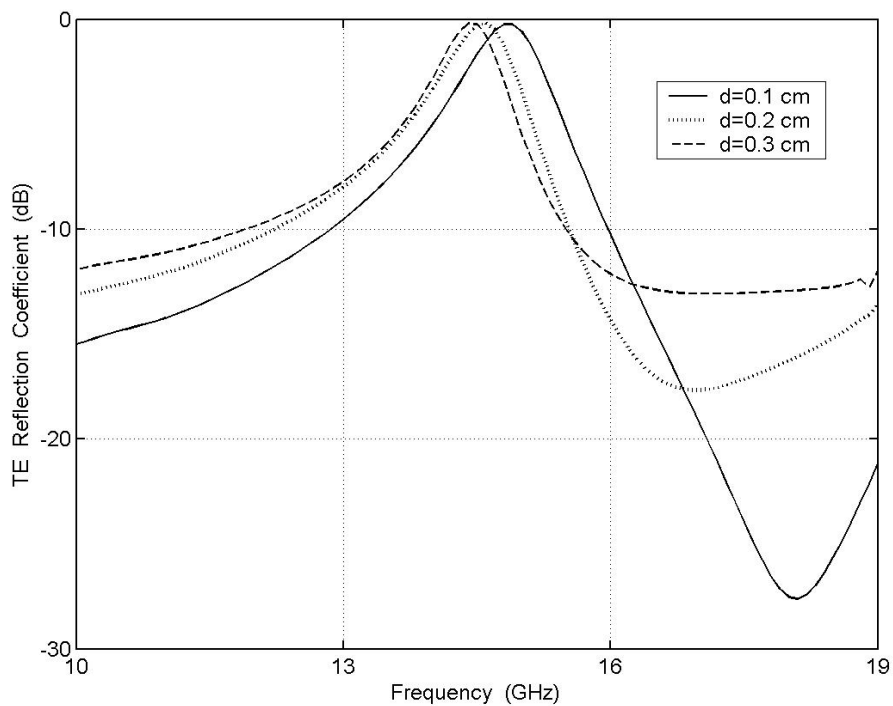
Figure 1.17 TE Reflection coefficient versus frequency for one–turn square spiral FSS at different slab thicknesses; θ=ϕ=0°, ε_r=1.6, h_1=0.2 cm, h_n=2(n–1)h_1, n=2,3,4., w=0.02 cm, d_1=d_2=1.55 cm

27

Figure 1.18 TE Reflection coefficient versus frequency for one–turn square spiral FSS at different values of ε_r; $\theta=\phi=0°$, d=0.1 cm, h_1=0.2 cm, h_n=2(n–1)h_1, n=2,3,4., w=0.02 cm, d_1=d_2=1.55 cm
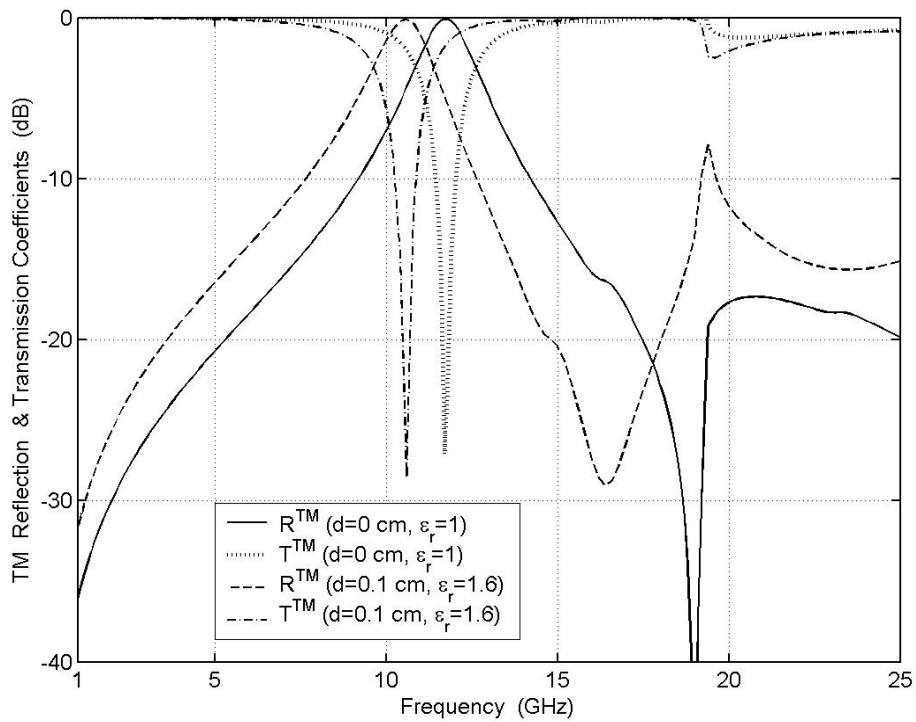
Figure 1.19 TM Reflection and transmission coefficients for freestanding and dielectric backed one–turn square spiral FSS; $\theta=\phi=0°$, h_1=0.2 cm, h_n=2(n–1)h_1, n=2,3,4., w=0.02 cm, d_1=d_2=1.55 cm
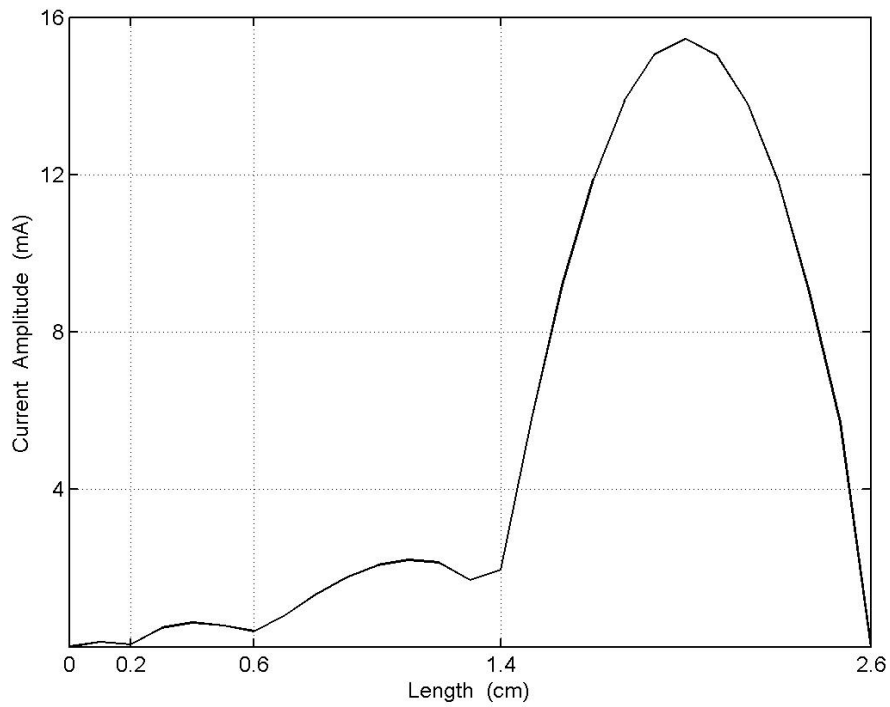
Figure 1.20 TM Current amplitude versus length for one–turn square spiral FSS at f_r=10.6 GHz; $\theta=\phi=0°$, d=0.1 cm, ε_r=1.6, h_1=0.2 cm, h_n=2(n–1)h_1, n=2, 3, 4., w=0.02 cm, d_1=d_2=1.55 cm

Figure 1.21 TM Reflection coefficient versus frequency for one–turn square spiral FSS at different incident angles; ϕ=0°, d=0.1 cm, ε_r=1.6, h_1=0.2 cm, h_n=2(n–1)h_1, n=2, 3, 4., w=0.02 cm, d_1=d_2=1.55 cm

29

Figure 1.22 TM Reflection coefficient versus frequency for one–turn square spiral FSS at different slab thicknesses, $\theta=\phi=0°$, $\varepsilon_r=1.6$, $h_1=0.2$ cm, $h_n=2(n–1)h_1$, n=2, 3, 4., $w=0.02$ cm, $d_1=d_2=1.55$ cm
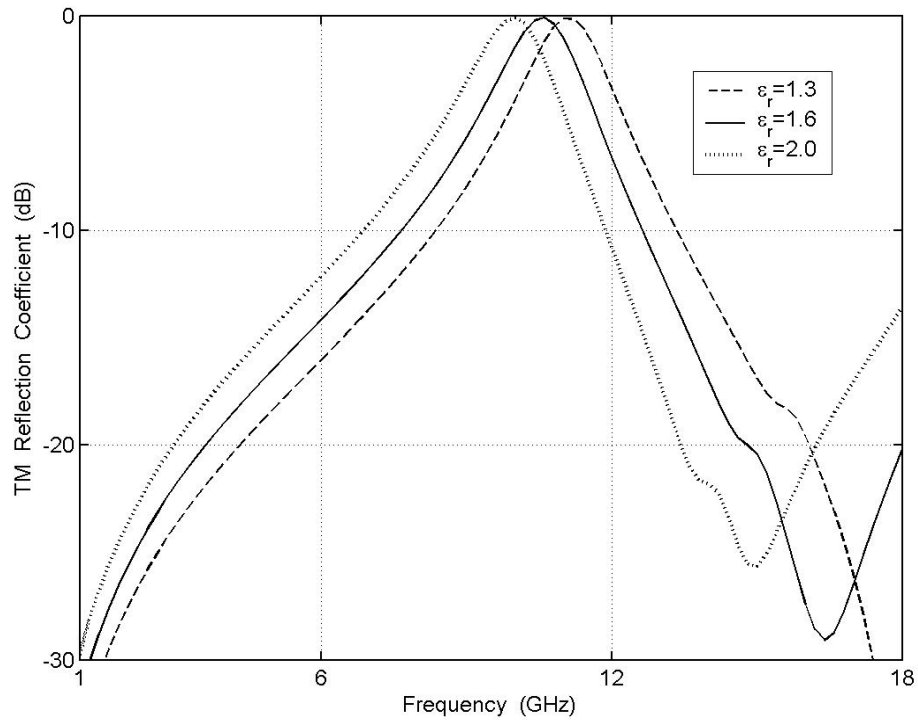
Figure 1.23 TM Reflection coefficient versus frequency for one–turn square spiral FSS at different values of ε_r, $\theta=\phi=0°$, $d=0.1$ cm, $h_1=0.2$ cm, $h_n=2(n–1)h_1$, n=2, 3, 4., $w=0.02$ cm, $d_1=d_2=1.55$ cm

30

The numerical results of the FSS comprised of periodic arrays of two–turn square spiral shaped conductors in the case of TE and TM incident waves are presented from Figure 1.24 to Figure 1.31 [36, 37]. The length of the first segment is h_1=0.1 cm. The lengths of the other segments can be found from the relation $h_n=2h_1(n-1)$ for n=2, 3, … , 8. The overall length of the spiral is 5.7 cm. The width of the two–turn square spiral was chosen as h_1/10. The inter–element spacings are 1.7 cm. The periodic cells are arranged in square dimension. The number of basis functions required to estimate the unknown current coefficients is 56. The number of included Floquet modes is 961. This number is obtained by inclusion of more Floquet modes until there is little change in the results. The only propagating mode is the zero order Floquet mode. Keeping d_1 and d_2 small delays the onset of grating modes.

In Figure 1.24 and 1.25 the reflection and transmission coefficients are plotted for freestanding and dielectric backed two–turn square spiral FSS, under normal incidence with electric field polarized along the y–axis (TE incidence). The resonance frequency for the freestanding FSS is at 16.08 GHz. The resonance frequency moves to14.62 GHz, when FSS is supported by dielectric slab as shown in Figure 1.24. There is a full transmission at the S–band frequency region (1–5 GHz). The FSS comprised of periodic two–turn square spiral shaped conductors is used as a band stop filter in the microwave frequency regions of Ku–band (12.5–18 GHz) as shown in Figure1.25. The curve in Figure 1.26 illustrates the normalized current amplitude versus overall length for dielectric backed two–turn square spiral FSS under normal incidence at resonant frequency (f_r=14.62 GHz). The vertical grids show the corner points of the structure. More current is induced on the fifth segment of the structure. Figure 1.27 shows TE reflection coefficient for different values of the first strip length (h_1). As the length of the first strip increases by 0.01 cm each time, the resonance shifts nearly 1 GHz to lower frequencies. The resonance frequencies are 14.62 GHz, 13.3 GHz and 12.3 GHz for the values of first strip lengths of 0.10 cm, 0.11 cm, 0.12 cm, respectively. In Figure 1.28, TE reflection coefficient is plotted against frequency for the incident angle variations. The resonance frequency shifts to lower frequency for oblique angle of incidence 10°. When this value is greater than 10° the resonance disappears.

Plots in Figures 1.29 and 1.30 shows the reflection and transmission coefficients for freestanding and dielectric backed two–turn square spiral FSS corresponding to TM incident plane wave. There are two resonant frequencies for TM incident wave at 12.3 GHz and 17.52 GHz for dielectric slab as shown in Figure 1.29. The bandwidth of the first resonance is wider than the second one. The second resonance is due to the higher order grating modes. There is a full transmission at the S–band frequency region (1–5GHz) as shown in Figure 1.30. The FSS comprised of periodic two–turn square spiral shaped conductors is used as a band stop filter in the microwave frequency regions of Ku–band (12.5–18 GHz). Figure 1.31 illustrates the normalized current versus length for dielectric backed FSS at resonance frequency. More current is induced on the sixth segment of the two–turn square spiral. Figure 1.32 depicts TM reflection coefficient for different values of the first strip length (h_1). As the length of the first strip increases, the resonance shifts nearly 1 GHz to lower frequencies. The resonance frequencies are 12.3 GHz, 11.2 GHz and 10.3 GHz for the values of first strip lengths of 0.10 cm, 0.11 cm, 0.12 cm, respectively. It is seen that the curves are approximately equal to each other. Figure 1.33 illustrates the oblique angle incidence variations for the magnitude of TM reflection coefficient. The first resonant frequency is almost stable up to 20° incidences. There is a small decrease in bandwidth of the reflected wave. The second resonance disappears for oblique angle of incidence. When the angle of incidence is greater than 20°, the magnitude of the first peak reduces and resonance disappears. The variation of dielectric constant and slab thickness versus frequency are not plotted for the two–turn square spiral FSS. Since, we know their effects from the L–shaped and one–turn square spiral FSS structures. FSS with two–turn square spiral array can be used as a band–stop filter at different frequencies for TE and TM wave incidences. There is anti–resonance at S–band and Ku–band frequency regions. Therefore, it can be made into both reflecting and transparent FSS.
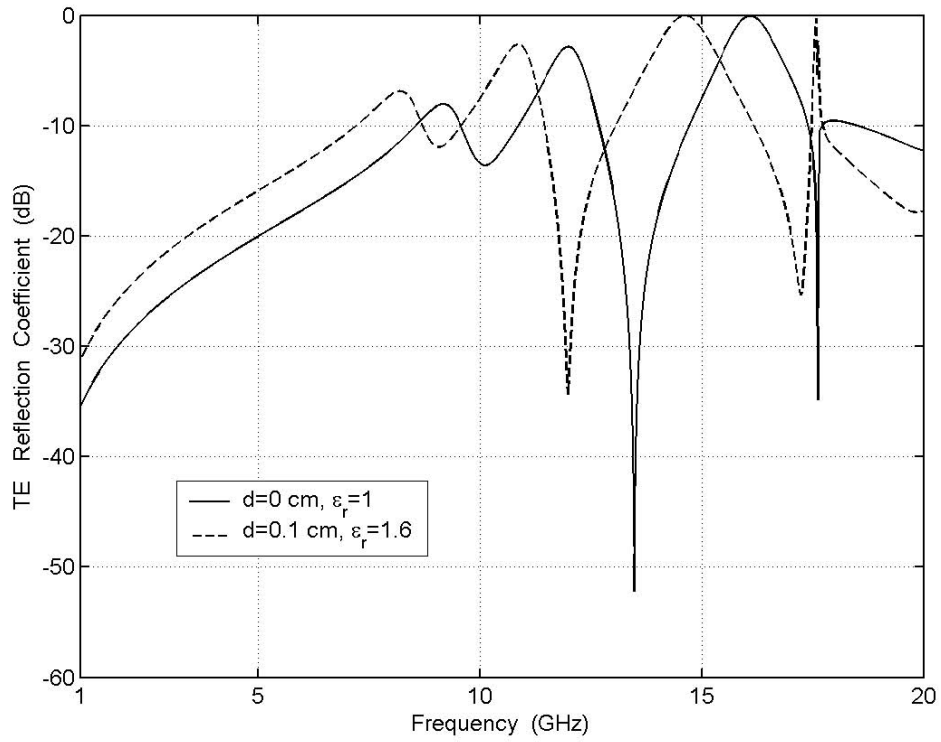
Figure 1.24 TE Reflection coefficient for freestanding and dielectric backed two–turn square spiral FSS; $\theta=\phi=0°$, $d=0.1$ cm, $\varepsilon_r=1.6$, $h_1=0.1$ cm, $h_n=2(n–1)h_1$, n=2, 3,…,8., $w=0.01$ cm, $d_1=d_2=1.7$ cm
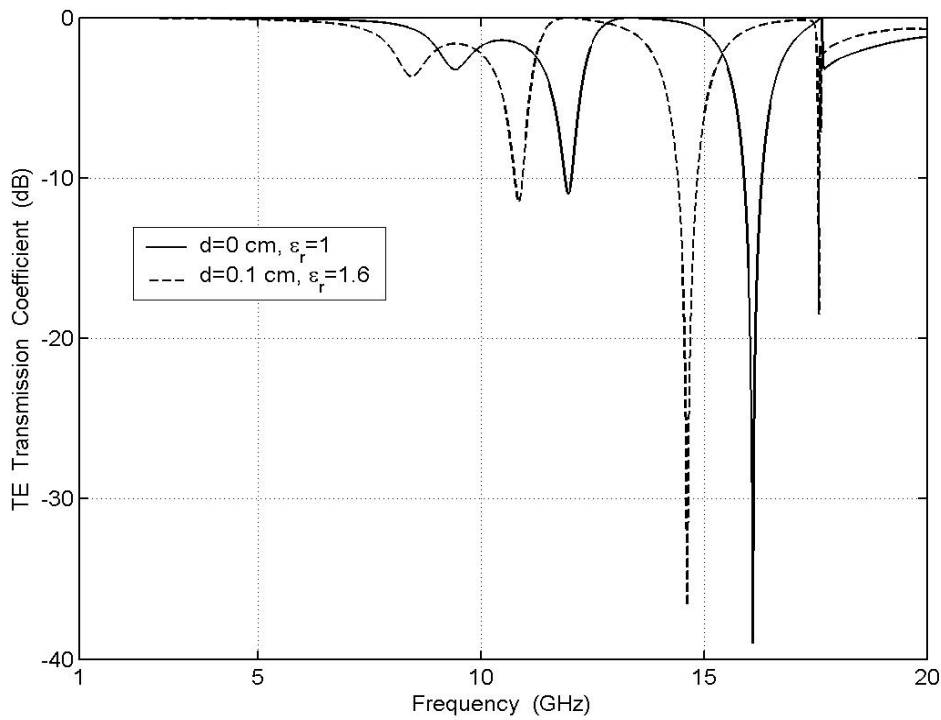
Figure 1.25 TE Transmission coefficient for freestanding and dielectric backed two–turn square spiral FSS; $\theta=\phi=0°$, $d=0.1$ cm, $\varepsilon_r=1.6$, $h_1=0.1$ cm, $h_n=2(n–1)h_1$, n=2, 3,…,8., $w=0.01$ cm, $d_1=d_2=1.7$ cm

33
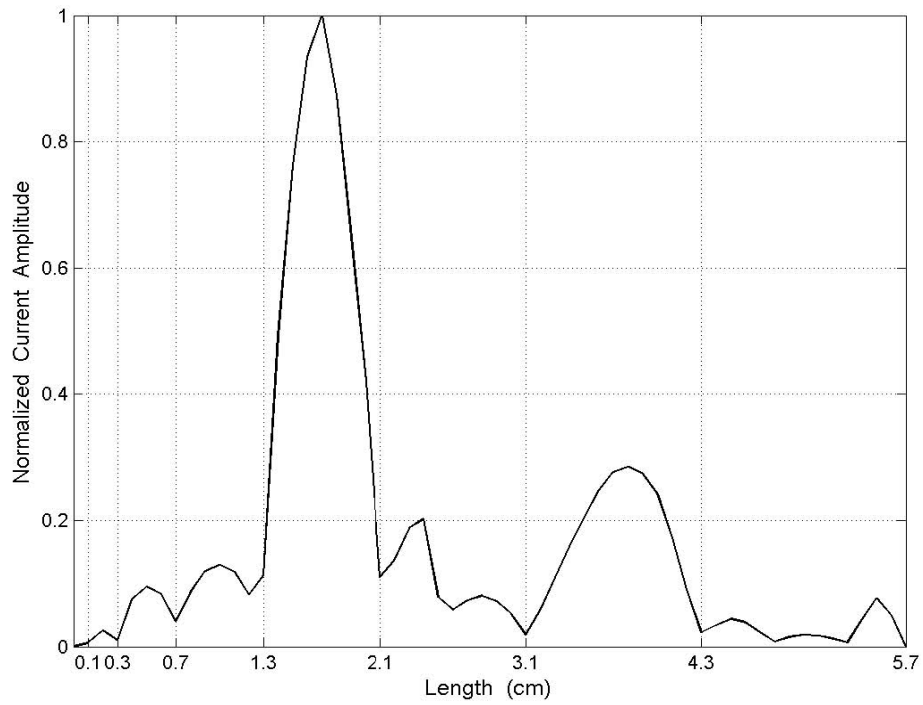
Figure 1.26 TE Normalized current amplitude versus length for dielectric backed two–turn square spiral FSS at f_r=14.62 GHz; $\theta=\phi=0°$, d=0.1 cm, ε_r=1.6, h_1=0.1 cm, h_n=2(n–1)h_1, n=2, 3,…, 8., w=0.01 cm, d_1=d_2=1.7 cm
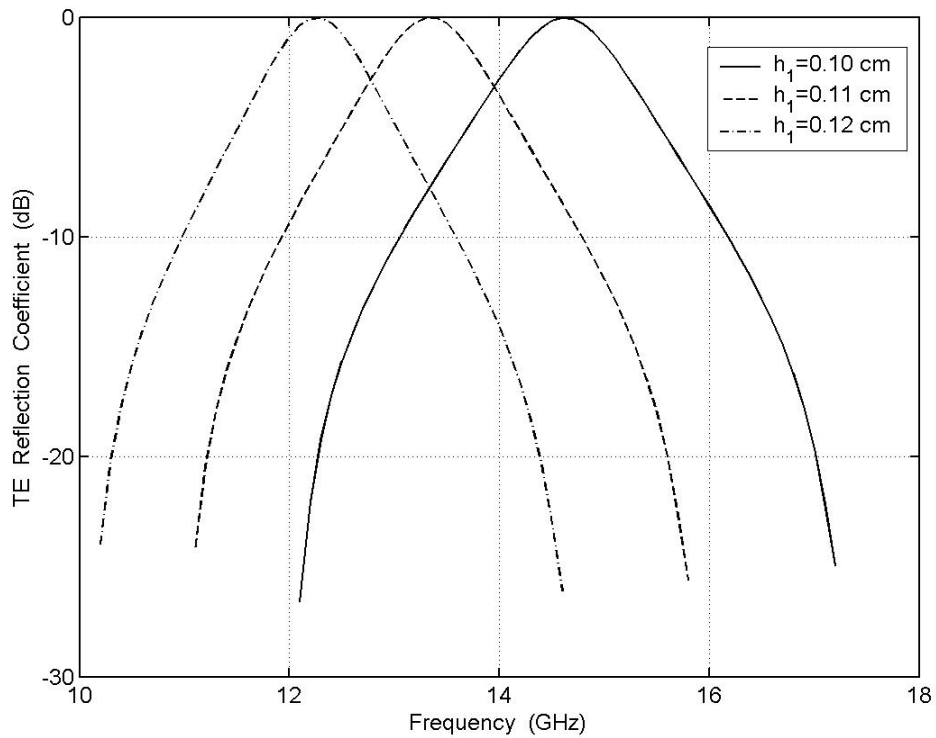
Figure 1.27 TE Reflection coefficient versus frequency for two–turn square spiral FSS at different values of first strip length, $\theta=\phi=0°$, d=0.1 cm, ε_r=1.6, h_n=2(n–1)h_1, n=2,3,…,8., w=h_1/10 cm

Figure 1.28 TE Reflection coefficient versus frequency for two–turn square spiral FSS at different incident angles; $\phi=0°$, $d=0.1$ cm, $\varepsilon_r=1.6$, $h_1=0.1$ cm, $h_n=2(n–1)h_1$, n=2,3,…,8., $w=0.01$ cm, $d_1=d_2=1.7$ cm
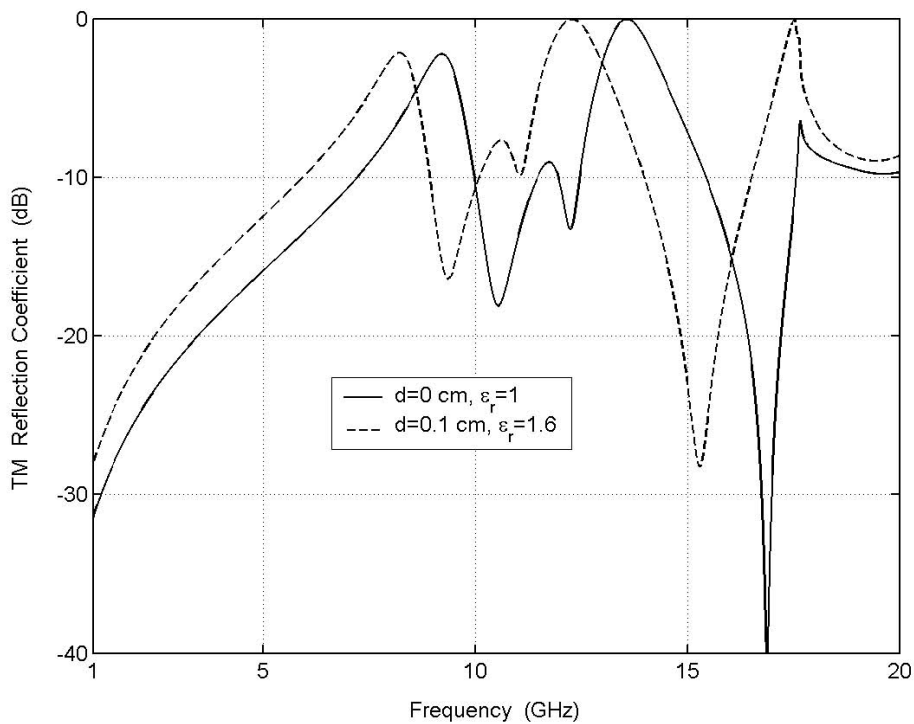
Figure 1.29 TM Reflection coefficient for freestanding and dielectric backed two–turn square spiral FSS; $\theta=\phi=0°$, $d=0.1$ cm, $\varepsilon_r=1.6$, $h_1=0.1$ cm, $h_n=2(n–1)h_1$, n=2, 3,…,8., $w=0.01$ cm, $d_1=d_2=1.7$ cm
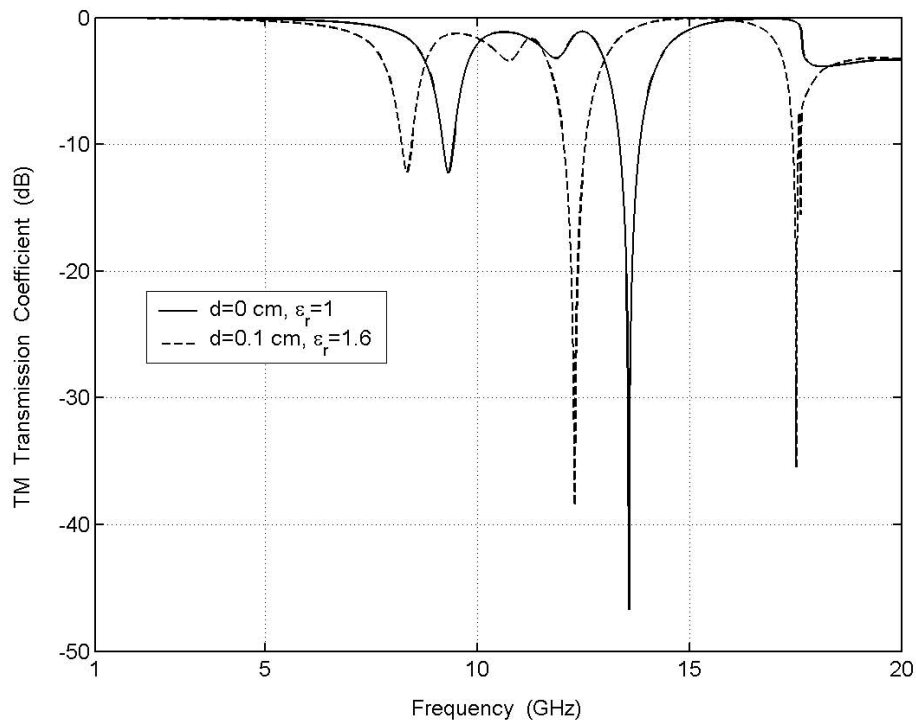
Figure 1.30 TM Transmission coefficient for freestanding and dielectric backed two–turn square spiral FSS; $\theta=\phi=0°$, $d=0.1$ cm, $\varepsilon_r=1.6$, $h_1=0.1$ cm, $h_n=2(n-1)h_1$, n=2, 3,...,8., $w=0.01$ cm, $d_1=d_2=1.7$ cm
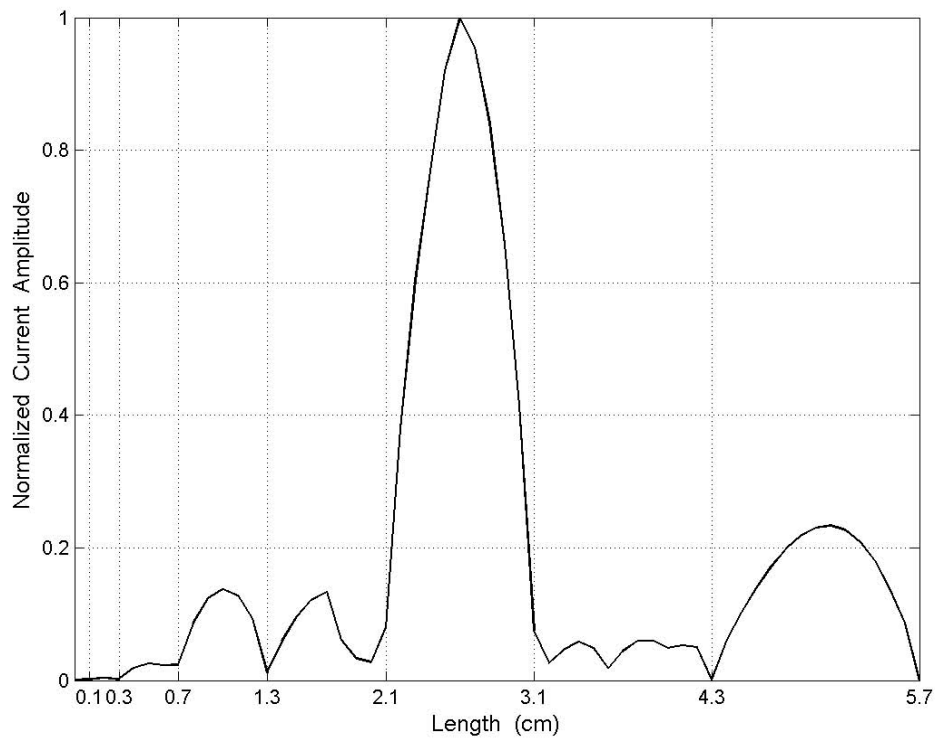
Figure 1.31 TM Normalized current amplitude versus length for dielectric backed two–turn square spiral FSS at $f_r=12.3$ GHz; $\theta=\phi=0°$, $d=0.1$ cm, $\varepsilon_r=1.6$, $h_1=0.1$ cm, $h_n=2(n-1)h_1$, n=2, 3,...,8., $w=0.01$ cm, $d_1=d_2=1.7$ cm

36
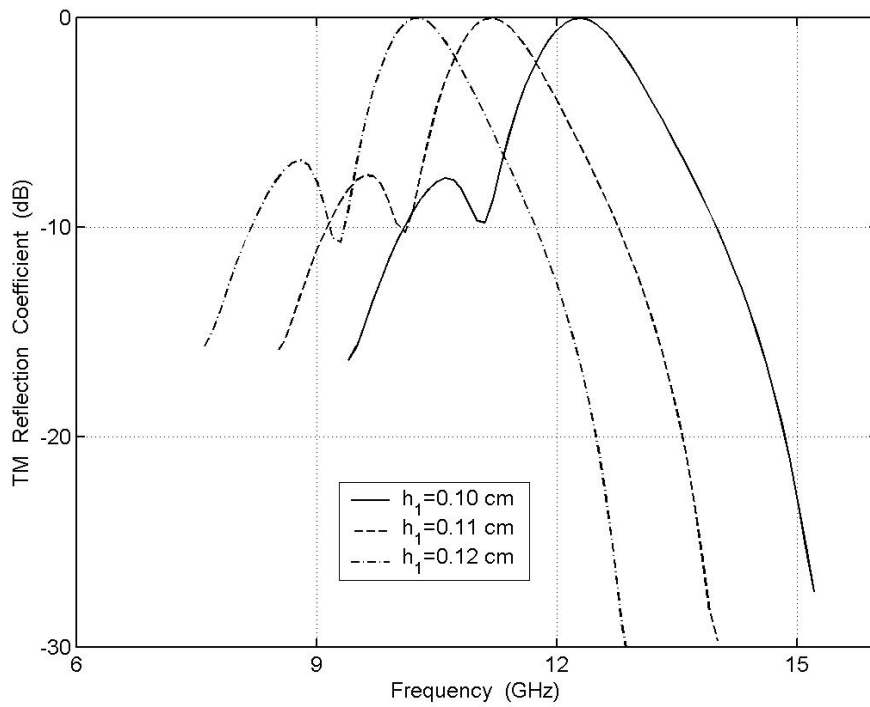
Figure 1.32 TM Reflection coefficient versus frequency for two–turn square spiral FSS at different values of first strip length, $\theta=\phi=0°$, $d=0.1$ cm, $\varepsilon_r=1.6$, $h_n=2(n-1)h_1$, n=2,3,…,8., $w=h_1/10$ cm
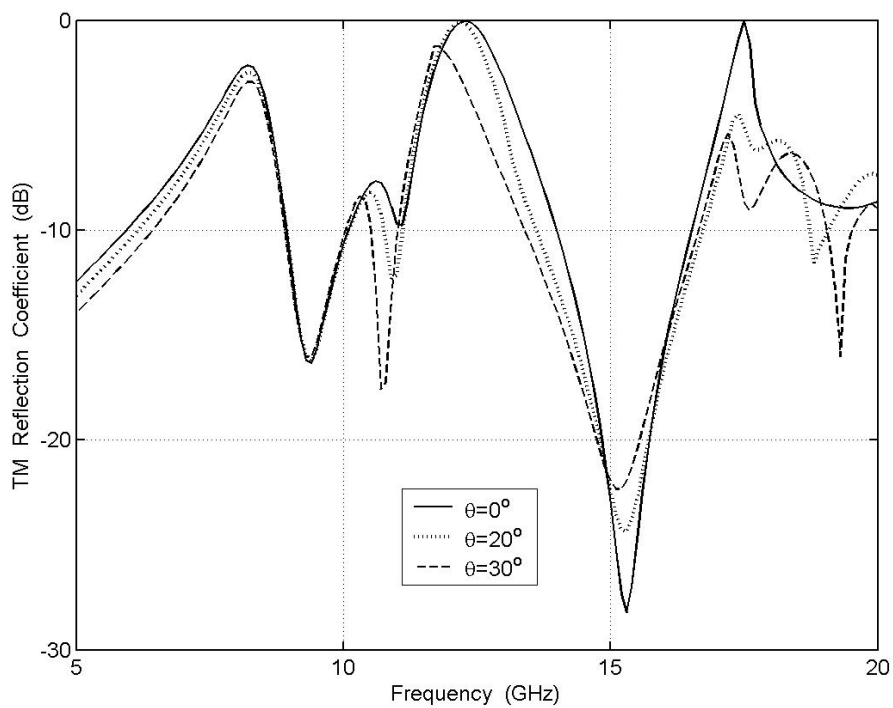
Figure 1.33 TM Reflection coefficient versus frequency for two–turn square spiral FSS at different incident angles; $\phi=0°$, $d=0.1$ cm, $\varepsilon_r=1.6$, $h_1=0.1$ cm, $h_n=2(n-1)h_1$, n=2,3,…,8., $w=0.01$ cm, $d_1=d_2=1.7$ cm

37

CHAPTER 2

CHIRAL BACKED FSSs

2.1 Introduction

Chiral materials, constructed by an artificial composite, have a great importance in electromagnetic field applications with ongoing progress. Such materials occur in nature as optically active molecules which display circular birefringence at optical frequencies. Since chirality is a geometric concept, a chiral object and its mirror image cannot be superimposed neither by rotation nor translation. This property is known as handedness. Objects that have the property of handedness are said to be either right–handed or left–handed. Chiral materials can be used to build novel microwave devices and structures. In microwave and millimeter wave regimes, chiral media are used in many applications, for instance, polarization transformers, phase shifters, antenna radomes, microstrip substrates, and waveguides. An artificial chiral medium for a microwave frequency can be constructed by embedding chiral objects, such as wire helices, möbius strip and irregular tetrahedrons in a non–chiral host medium.

Chiral media are known as optically active media. The special property of optically active media is that the polarization plane of linearly polarized electromagnetic wave is rotated as wave passes through the medium. The amount of rotation depends on the distance traveled by the wave in the medium and on the difference between the two wave numbers, which is indication of the degree of chirality. A linearly polarized wave incident on a chiral slab splits into two circularly polarized waves. One is left circularly polarized (LCP) wave and the other is right circularly polarized (RCP) wave with different phase velocities. The two circularly polarized waves combine and a linearly polarized wave emerges behind the chiral slab. The plane of polarization is rotated with respect to the plane of polarization of the incident plane wave [16–18].
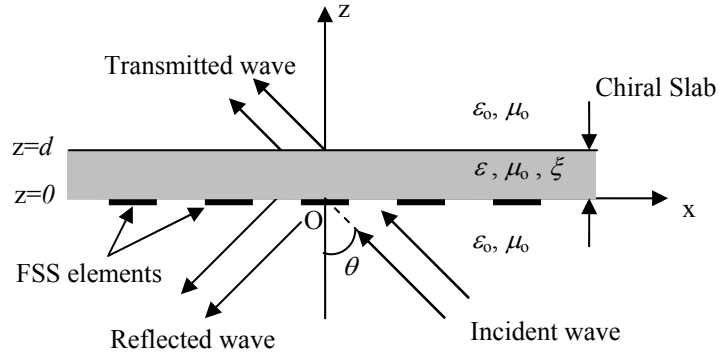
Figure 2.1   Geometry of FSS elements on Chiral Slab

An electric or magnetic incident field simultaneously produces both electric and magnetic polarization that exhibits magneto–electric coupling. The displacement vector **D** and the magnetic field **H** inside a chiral medium depends on both **E** and **B.** In order to explain the dependence, assume a short metallic helix as a chiral object in a dielectric medium, the incident electric field induces currents in the straight portion of the chiral object, and by continuity these currents must also flow in the circular portion of the object. The current in the straight portion contributes to the electric dipole moment of the object while the current in the circular portion contributes to its magnetic dipole moment. In a complementary manner, the incident magnetic field induces currents in the circular portion and by continuity in the straight portions. Thus, also the magnetic field contributes to the electric and magnetic dipole moments of the object.

In this Chapter, the reflection from and transmission through the chiral slab are analyzed for the three structures given in Figure 1.3. The chirality parameter is included to the slab parameters and the chiral slab is sandwiched between two free spaces as shown in Figure 2.1. Unlike a regular dielectric, the chiral scatterers produce both co–polarized and cross–polarized scattered fields. Four different coefficients are calculated when a plane wave is incident on a chiral medium. R_{co} and R_{cr} are the co– and cross–polarization of the reflected waves; T_{co} and T_{cr} are the co– and cross–polarization of the transmitted waves, respectively. The cross–polarization for TE and TM incidences correspond to TM and TE waves, respectively.

39

2.2 Propagation of Wave in Chiral Medium

The isotropic, homogeneous, lossless and source free chiral medium is characterized by the following constitutive relations for electromagnetic field with $e^{j\omega t}$ time harmonic dependence, [18]

$$D = \varepsilon E - j\xi B \tag{2.1}$$

$$H = \frac{1}{\mu_o} B - j\xi E \tag{2.2}$$

where ε, μ_o, and ξ, are real values for lossless media and represent permittivity, permeability, and chirality admittance (ξ) of the chiral medium, respectively. The magnitude of ξ is a measure of the degree of chirality while the sign of ξ specifies the medium handedness. When $\xi > 0$ the medium is a right handed and the sense of polarization is right handed, when $\xi < 0$, the medium is left handed and the sense of polarization is left handed; and when $\xi = 0$ the medium reduces to ordinary dielectric and there is no optical activity.

Inserting the constitutive relations into the source free Maxwell equations, the chiral wave equation for the electric and magnetic fields can be obtained as

$$\nabla \times \nabla \times \begin{pmatrix} E \\ H \end{pmatrix} - 2\omega\mu_o\xi\nabla \times \begin{pmatrix} E \\ H \end{pmatrix} - \omega^2\mu_o\varepsilon\begin{pmatrix} E \\ H \end{pmatrix} = 0 \tag{2.3}$$

The chiral media has two different phase velocities for RCP and LCP waves leading to two different wave numbers k_r and k_l which are given by

$$\begin{aligned} k_r &= \omega\mu_o\xi + \sqrt{\omega^2\mu_o^2\xi^2 + k^2} \\ k_l &= -\omega\mu_o\xi + \sqrt{\omega^2\mu_o^2\xi^2 + k^2} \end{aligned} \tag{2.4}$$

The two characteristic waves propagate at different velocities in the chiral medium, thereby causing birefringence. The solution to the chiral wave equation (Equation 2.3) consists of two partial waves, which are the right hand (E_2^+, H_2^+) and left hand (E_2^-, H_2^-) circularly polarized eigenwaves, [30] such that

$$\begin{aligned} E &= E_2^+ + E_2^- \\ H &= H_2^+ + H_2^- \end{aligned} \tag{2.5}$$

The total electric field in region z<0 for TM and TE wave incidences are

40

$$E_{inc}^{TM} = [E_o^{TM} e^{-j\gamma_{00}^o z} + E_{100}^{TM} e^{j\gamma_{00}^o z}] e^{-jk_{00} \cdot \rho} \kappa_{100} + je_{200}^{TE} e^{j\gamma_{00}^o z} e^{-jk_{00} \cdot \rho} \kappa_{200} \qquad (2.6)$$

$$E_{inc}^{TE} = [E_o^{TE} e^{-j\gamma_{00}^o z} + E_{200}^{TE} e^{j\gamma_{00}^o z}] e^{-jk_{00} \cdot \rho} \kappa_{200} + je_{100}^{TM} e^{j\gamma_{00}^o z} e^{-jk_{00} \cdot \rho} \kappa_{100} \qquad (2.7)$$

where E_o^{TM} and E_o^{TE} are the amplitude of the TM and TE incident waves. The magnitudes of the incident electric fields for TE and TM waves are equal to 1 and $\cos(\theta_i)$, respectively. The sets of $\{E_{100}^{TM} \text{ and } E_{200}^{TE}\}$ and $\{e_{200}^{TE} \text{ and } e_{100}^{TM}\}$ are the amplitude of the co–polarized and cross–polarized reflected waves in the absence of scatterers, respectively.

The scattered reflected electric fields in region z<0 due to metallic structures at the interface of chiral slab are,

$$E_{r1} = \sum_p \sum_q [E_{1pq}^{TM} \kappa_{1pq} + je_{1pq}^{TE} \kappa_{2pq}] e^{-jk_{pq} \cdot \rho} e^{j\gamma_{pq}^o z} \qquad (2.8)$$

$$E_{r2} = \sum_p \sum_q [E_{2pq}^{TE} \kappa_{2pq} + je_{2pq}^{TM} \kappa_{1pq}] e^{-jk_{pq} \cdot \rho} e^{j\gamma_{pq}^o z} \qquad (2.9)$$

The RCP and LCP waves inside the chiral medium (0<z<d) for TM wave incidence are,

$$E_2^+ = \sum_{m=1}^2 \sum_p \sum_q j^{m-1} [A_{mpq}^l e^{-j\gamma_{pq}^l z} + (-1)^{m-1} A_{mpq}^r e^{-j\gamma_{pq}^r z}] \kappa_{mpq} e^{-jk_{pq} \cdot \rho} \qquad (2.10)$$

$$E_2^- = \sum_{m=1}^2 \sum_p \sum_q (-j)^{m-1} [B_{mpq}^l e^{j\gamma_{pq}^l z} + (-1)^{m-1} B_{mpq}^r e^{j\gamma_{pq}^r z}] \kappa_{mpq} e^{-jk_{pq} \cdot \rho} \qquad (2.11)$$

The RCP and LCP waves inside the chiral medium (0<z<d) for TE wave incidence are,

$$E_2^+ = \sum_{m=1}^2 \sum_p \sum_q j^m [C_{mpq}^l e^{-j\gamma_{pq}^l z} + (-1)^{m-1} C_{mpq}^r e^{-j\gamma_{pq}^r z}] \kappa_{mpq} e^{-jk_{pq} \cdot \rho} \qquad (2.12)$$

$$E_2^- = \sum_{m=1}^2 \sum_p \sum_q (-j)^m [D_{mpq}^l e^{j\gamma_{pq}^l z} + (-1)^{m-1} D_{mpq}^r e^{j\gamma_{pq}^r z}] \kappa_{mpq} e^{-jk_{pq} \cdot \rho} \qquad (2.13)$$

where the propagation constants for RCP (γ_{pq}^r) and LCP (γ_{pq}^l) waves along the transverse direction is defined as

$$\gamma_{pq}^{r,l} = \begin{cases} \sqrt{k_{r,l}^2 - |k_{pq}|^2} & k_{r,l} \geq |k_{pq}| \\[2mm] -j\sqrt{|k_{pq}|^2 - k_{r,l}^2} & k_{r,l} \leq |k_{pq}| \end{cases} \tag{2.14}$$

The corresponding magnetic fields inside the chiral slab can be obtained from the relation,

$$\mathbf{H} = \frac{j}{\omega\mu_o}(\nabla \times \mathbf{E} - \omega\mu_o \xi \mathbf{E}) \tag{2.15}$$

The electric fields in region z>d for TM and TE wave incidences are,

$$\mathbf{E}_{t1} = \sum_p \sum_q [E_{3pq}^{TM}\boldsymbol{\kappa}_{1pq} + je_{3pq}^{TE}\boldsymbol{\kappa}_{2pq}]e^{-j\mathbf{k}_{pq}\cdot\boldsymbol{\rho}}e^{-j\gamma_{pq}^o z} \tag{2.16}$$

$$\mathbf{E}_{t2} = \sum_p \sum_q [E_{3pq}^{TE}\boldsymbol{\kappa}_{2pq} + je_{3pq}^{TM}\boldsymbol{\kappa}_{1pq}]e^{-j\mathbf{k}_{pq}\cdot\boldsymbol{\rho}}e^{-j\gamma_{pq}^o z} \tag{2.17}$$

In Equations (2.8)–(2.17) E_{1pq}^{TM}, e_{1pq}^{TE}, E_{2pq}^{TE}, e_{2pq}^{TM}, $A_{mpq}^{r,l}$, $B_{mpq}^{r,l}$, $C_{mpq}^{r,l}$, $D_{mpq}^{r,l}$, E_{3pq}^{TM}, e_{3pq}^{TE}, E_{3pq}^{TE}, e_{3pq}^{TM} are unknown field amplitudes and can be found in terms of medium parameters after matching the boundary conditions.

Matching the boundary conditions as mentioned in Chapter 1, one can get the EFIE for TM wave incidence,

$$-\{(E_o^{TM} + E_{100}^{TM})\boldsymbol{\kappa}_{100} + je_{200}^{TE}\boldsymbol{\kappa}_{200}\}e^{-j\mathbf{k}_{pq}\cdot\boldsymbol{\rho}} =$$

$$\sum_{n=1}^N \alpha_n \sum_{p=-\infty}^\infty \sum_{q=-\infty}^\infty [(D_{1pq}g_{npq}^{TM} + D_{2pq}g_{npq}^{TE})\boldsymbol{\kappa}_{1pq}e^{-j\mathbf{k}_{pq}\cdot\boldsymbol{\rho}} + j(D_{3pq}g_{npq}^{TM} + D_{4pq}g_{npq}^{TE})\boldsymbol{\kappa}_{2pq}e^{-j\mathbf{k}_{pq}\cdot\boldsymbol{\rho}}] \tag{2.18}$$

Similarly for TE incident wave the EFIE is,

$$-\{(E_o^{TE} + E_{200}^{TE})\boldsymbol{\kappa}_{200} + je_{100}^{TM}\boldsymbol{\kappa}_{100}\}e^{-j\mathbf{k}_{pq}\cdot\boldsymbol{\rho}} =$$

$$\sum_{n=1}^N \alpha_n \sum_{p=-\infty}^\infty \sum_{q=-\infty}^\infty [(C_{1pq}g_{npq}^{TE} + C_{2pq}g_{npq}^{TM})\boldsymbol{\kappa}_{2pq}e^{-j\mathbf{k}_{pq}\cdot\boldsymbol{\rho}} + j(C_{3pq}g_{npq}^{TE} + C_{4pq}g_{npq}^{TM})\boldsymbol{\kappa}_{1pq}e^{-j\mathbf{k}_{pq}\cdot\boldsymbol{\rho}}] \tag{2.19}$$

where C_{spq} and D_{spq} are known coefficients (s=1,2,3,4)

$$\begin{aligned} g_{npq}^{TM} &= \boldsymbol{\kappa}_{1pq} \cdot \mathbf{g}_{npq} \\ g_{npq}^{TE} &= \boldsymbol{\kappa}_{2pq} \cdot \mathbf{g}_{npq} \end{aligned} \tag{2.20}$$

Multiplying both sides of (2.18) and (2.19) by $f_m(x, y)$ and integrating over a unit cell yields a simultaneous equation or NxN matrix equation.

$$[V_m]^{TM,TE} = [Z_{mn}]^{TM,TE} \quad [\alpha_n]^{TM,TE} \tag{2.21}$$

where V, Z and α are the excitation vector, the impedance matrix and unknown coefficients, respectively. The excitation vectors are given by the equations,

$$[V]_{Nx1}^{TM} = -(E_o^{TM} + E_{100}^{TM})(g_{n00}^{TM})^\bullet - je_{200}^{TE}(g_{n00}^{TE})^\bullet \tag{2.22}$$

$$[V]_{Nx1}^{TE} = -(E_o^{TE} + E_{200}^{TE})(g_{n00}^{TE})^\bullet - je_{100}^{TM}(g_{n00}^{TM})^\bullet \tag{2.23}$$

The elements of the impedance matrix are

$$[Z_{mn}]^{TM} = \frac{1}{A}\sum_p\sum_q[(D_{1pq}\boldsymbol{g}_{npq}^{TM} + D_{2pq}\boldsymbol{g}_{npq}^{TE})(\boldsymbol{g}_{mpq}^{TM})^\bullet + j(D_{3pq}\boldsymbol{g}_{npq}^{TM} + D_{4pq}\boldsymbol{g}_{npq}^{TE})(\boldsymbol{g}_{mpq}^{TE})^\bullet] \tag{2.24}$$

$$[Z_{mn}]^{TE} = \frac{1}{A}\sum_p\sum_q[(C_{1pq}\boldsymbol{g}_{npq}^{TE} + C_{2pq}\boldsymbol{g}_{npq}^{TM})(\boldsymbol{g}_{mpq}^{TE})^\bullet + j(C_{3pq}\boldsymbol{g}_{npq}^{TE} + C_{4pq}\boldsymbol{g}_{npq}^{TM})(\boldsymbol{g}_{mpq}^{TM})^\bullet] \tag{2.25}$$

where the asterisk denotes the complex conjugate. By inverting the matrix equation (2.21), the unknown current coefficients can be obtained. The co– and cross–polarized reflection and transmission coefficients can then be written as

$$R_{co}^{TM} = E_{100}^{TM} + \sum_{n=1}^{N}\alpha_n^{TM}(D_{100}g_{n00}^{TM} + D_{200}g_{n00}^{TE})/A \tag{2.26}$$

$$R_{cr}^{TE} = e_{200}^{TE} + \sum_{n=1}^{N}\alpha_n^{TM}(D_{300}g_{n00}^{TM} + D_{400}g_{n00}^{TE})/A \tag{2.27}$$

$$T_{co}^{TM} = E_{300}^{TM} + \sum_{n=1}^{N}\alpha_n^{TM}(K_{100}g_{n00}^{TM} + K_{200}g_{n00}^{TE})/A \tag{2.28}$$

$$T_{cr}^{TE} = e_{300}^{TE} + \sum_{n=1}^{N}\alpha_n^{TM}(K_{300}g_{n00}^{TM} + K_{400}g_{n00}^{TE})/A \tag{2.29}$$

$$R_{co}^{TE} = E_{200}^{TE} + \sum_{n=1}^{N}\alpha_n^{TE}(C_{100}g_{n00}^{TE} + C_{200}g_{n00}^{TM})/A \tag{2.30}$$

$$R_{cr}^{TM} = e_{100}^{TM} + \sum_{n=1}^{N}\alpha_n^{TE}(C_{300}g_{n00}^{TE} + C_{400}g_{n00}^{TM})/A \tag{2.31}$$

$$T_{co}^{TE} = E_{300}^{TE} + \sum_{n=1}^{N}\alpha_n^{TE}(P_{100}g_{n00}^{TE} + P_{200}g_{n00}^{TM})/A \tag{2.32}$$

$$T_{cr}^{TM} = e_{300}^{TM} + \sum_{n=1}^{N} \alpha_n^{TE} (P_{300} g_{n00}^{TE} + P_{400} g_{n00}^{TM}) / A \qquad (2.33)$$

where the detailed expressions for the unknown parameters D_{k00}, K_{k00}, C_{k00} and P_{k00} can be seen in Appendix. (k=1,2,3,4.)

2.2.1 Numerical Results of Strip FSS on a Chiral Slab

The numerical results of a strip FSS on a chiral slab [38] is given in this section in order to compare the results. The configuration considered here is two dimensional infinite arrays of perfectly conducting narrow strips having dimensions h=0.92 cm and w=0.1 cm. The FSS strip elements are arranged in a square lattice, d_1=d_2=1 cm. The structure is excited by a normally incident plane wave polarized in $\boldsymbol{a}_y$ direction. The slab thickness and dielectric constants are 0.5 cm and 1.06, respectively. These numerical values are taken from Koca's dissertation [27]. The correctness of the algorithm is ensured by comparing the numerical results with that of [27] for a narrow strip FSS backed by chiral slab and proved to be as good. The amplitude of co– and cross–polarized reflection and transmission coefficients are plotted with respect to frequency for different values of chirality admittance. The value of chirality admittance is varied within the range given by inequality $|\xi| \le \sqrt{\varepsilon_r \varepsilon_o / \mu_o}$ [17]. For instance, the chirality admittance changes from 0 to 0.003355 for 1.6 value of dielectric constant.

In the case of TE or TM wave incidences, we have two reflection and two transmission coefficients in the first and third regions, respectively. Totally, four coefficients are calculated when a plane wave is incident on a chiral medium. That is co– and cross–polarized reflection and transmission coefficients. As shown in Figure 2.2a the co–polarized reflection coefficient at low chirality admittance is very close to the dielectric case. Multiple resonances with narrow bandwidth appear when the chirality admittance of the slab is increased to 0.0015 and 0.0025 S. At the resonant frequency of f_r = 21.04 GHz, R_{co}^{TE} looks like a spike with a very narrow bandwidth. For small values of chirality admittance the co–polarized transmission coefficient of chiral FSS exhibits similarity with that one of the dielectric FSS as shown in Figure 2.2b. In Figure 2.2c full transmission is observed for cross–polarization at 16.35

GHz. At this frequency the polarization state of the incident wave is converted from TE to TM or we can say that optical activity is observed. The current amplitude induced on the strip FSS on chiral slab is illustrated in Figure 2.3 against the length of strip at resonance frequencies for the chirality admittance of ξ=0.0025 S. At resonant frequencies, the current amplitude is maximum at the center of strip, and it is symmetric with respect to the center of strip. At f_r = 21.04 GHz, the current has two equal peaks which are the mirror image of each other with respect to center.
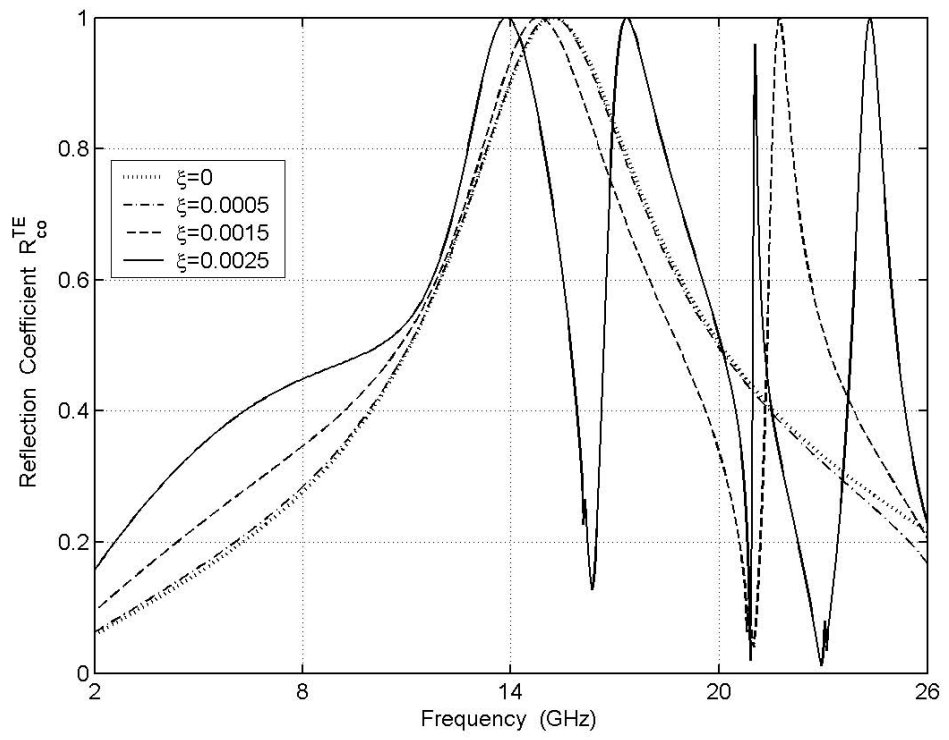
(*a*)
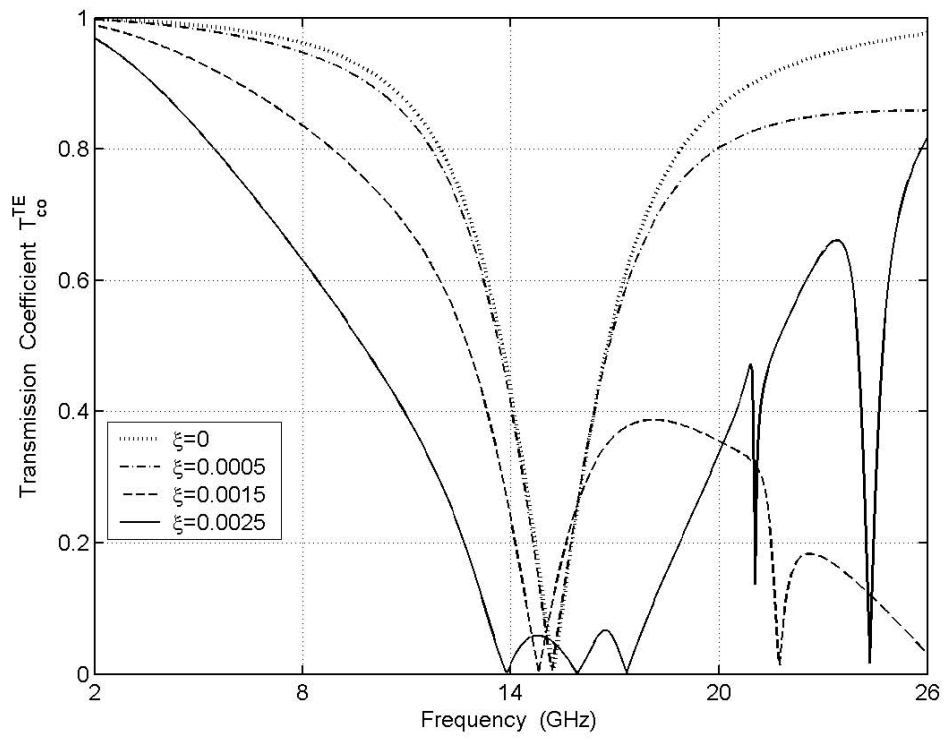
(b)
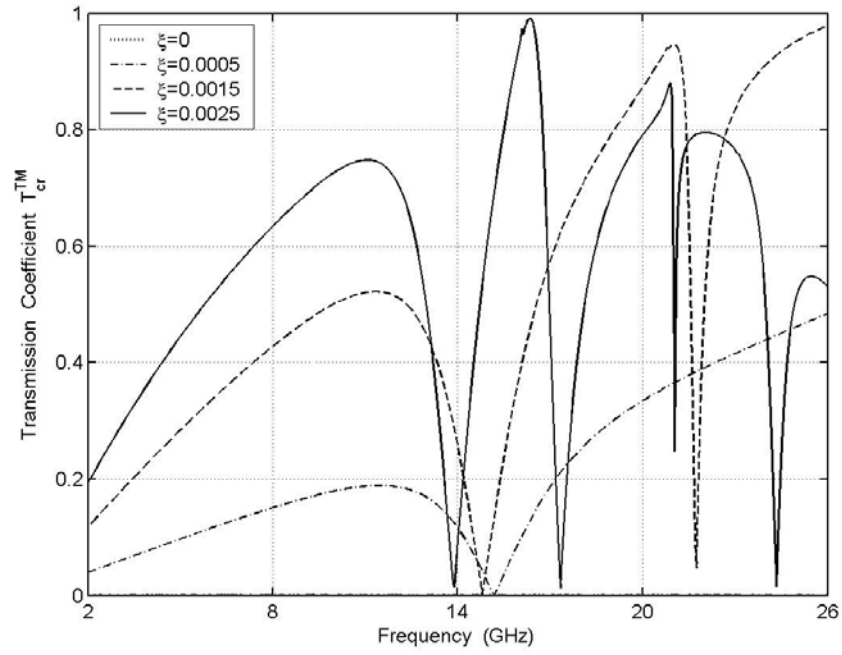
(c)

Figure 2.2 Reflection and transmission coefficients of strip FSS on a chiral slab at different chirality admittances; TE incidence, $\theta=\phi=0°$, $d=0.5$ cm, $\varepsilon_r=1.06$, $w=0.1$ cm, $h=0.92$ cm, $d_1=d_2=1$ cm, (*a*) Reflection Coefficient R_{co}^{TE}, (b) Transmission Coefficient T_{co}^{TE}, (c) Transmission Coefficient T_{cr}^{TM}
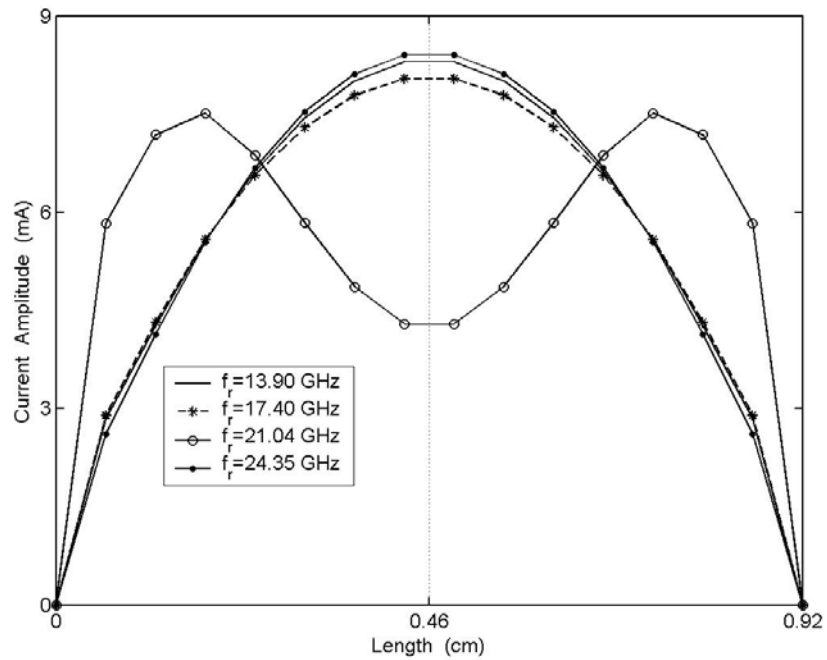
Figure 2.3 Current amplitude versus length at resonance frequencies of strip FSS on a chiral slab; $\theta=\phi=0°$, $\xi=0.0025$ S, $d=0.5$ cm, $\varepsilon_r=1.06$, $w=0.1$ cm, $h=0.92$ cm, $d_1=d_2=1$ cm

47

2.2.2 Numerical Results of L–Shaped FSS on a Chiral Slab

The numerical results of L–shaped FSS backed by chiral slab have been presented for TE and TM incident plane waves [38, 39]. The co– and cross–polarized reflection and transmission coefficients are plotted against frequency at normal incidence for different values of medium parameters such as chirality admittance, slab thickness, and dielectric constant. The coefficients are also plotted for TE and TM incident waves at oblique incidence. The lengths of L–shaped FSS and other parameters can be found in section 1.4.1 of Chapter 1.

Figure 2.4 shows the effect of chirality admittance variations at normal incidence of TE wave. As can be seen from Figure 2.4a at low chirality admittance the reflected wave is close to the dielectric case and has a one resonance frequency. Multiple resonances are seen for high value of chirality admittance because one wave number becomes very high at that value. It is highly interesting that at around 10 GHz the magnitude of co–polarized reflection coefficient is nearly the same for various chirality admittances as shown in Figure 2.4a. At this frequency chiral slab behaves as an ordinary dielectric slab for the reflection. For chirality admittances of ξ=0.002 S and ξ=0.003 S values the cross–polarized transmission coefficient (T_{cr}^{TM}) reaches unity (0–dB) which means that the polarization state of the incident TE wave is converted to TM wave at that frequency. This phenomenon is due to the effect of optical activity, indicating that chirality of slab caused significant rotation of the waves. The cross–polarized transmission coefficient T_{cr}^{TM} has also nulls at resonance frequencies as shown in Figure 2.4b. The magnitude of co–polarized transmission coefficients are very close to each other for low values of chirality admittances but, for higher values the curves are quite different, as seen in Figure 2.4c. At normal incidence the magnitude of the cross–polarized reflection coefficient (R_{cr}^{TM}) is very low as given in Figure 2.4d. In Figure 2.5 the slab thickness variations are plotted for ξ=0.003 S with a dielectric constant of ε_r=1.6. Multiple resonances appear for a thick slab as depicted in Figure 2.5a. The conversion of the polarization state is obtained for d=0.3 and 0.5 cm at the frequency of 21.2 and 14.4 GHz, respectively as shown in Figure 2.5b. The magnitude of T_{co}^{TE} decreases up to 12 GHz as illustrated in

Figure 2.5c. The magnitude of R_{cr}^{TM} is less than -20 dB as depicted in Figure 2.5d. The variation of dielectric constant is shown in Figure 2.6. The resonant and anti–resonant frequencies decrease or shift to left side for an increase in dielectric constant as given in Figure 2.6a and 2.6b. The magnitude of T_{co}^{TE} is nearly the same up to 10 GHz as shown in Figure 2.6c. It has greater peaks at around 21 GHz. The magnitude of R_{cr}^{TM} is less than -20 dB as depicted in Figure 2.6d. The oblique incidence variations are shown in Figure 2.7 for the value of ξ=0.002 S. In Figure 2.7a, two resonant frequencies are seen at normal incidence. The resonant frequencies disappear for an obliquely incident TE wave. Full transmissions are observed for cross–polarized field at normal and oblique angle of incidences as illustrated in Figure 2.7b. The co–polarized transmission coefficient is not affected from the variation of incident angle up to 10 GHz, but it is oscillatory for high frequency values, as depicted in Figure 2.7c. At oblique angle of incidence, the magnitude of R_{cr}^{TM} is seen to increase in high frequency region as depicted in Figure 2.7d.
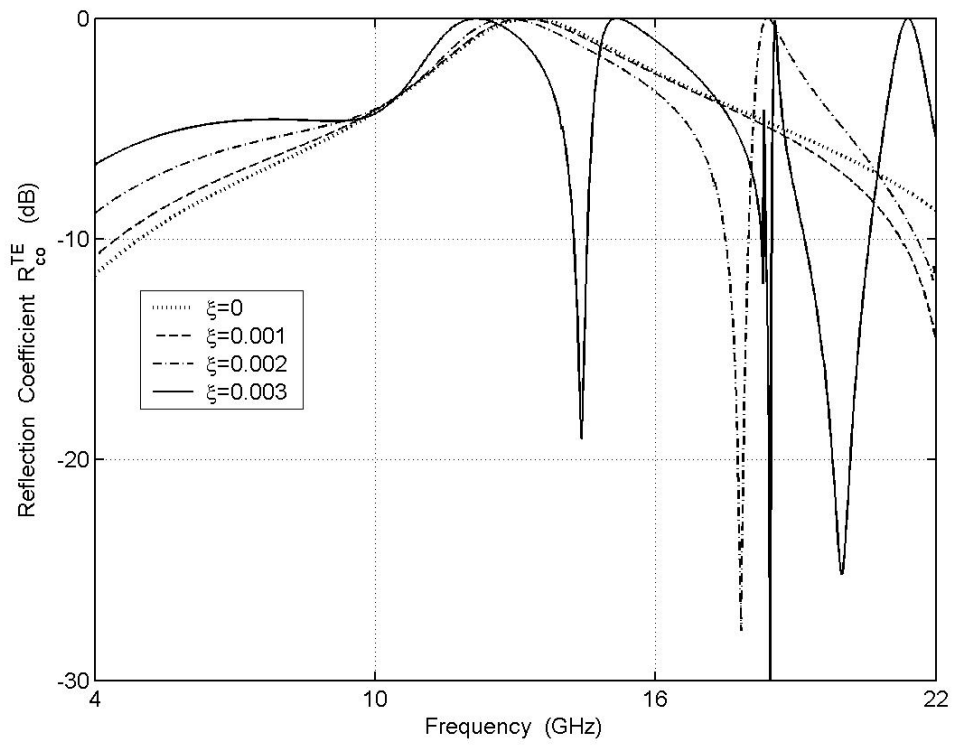
(*a*)
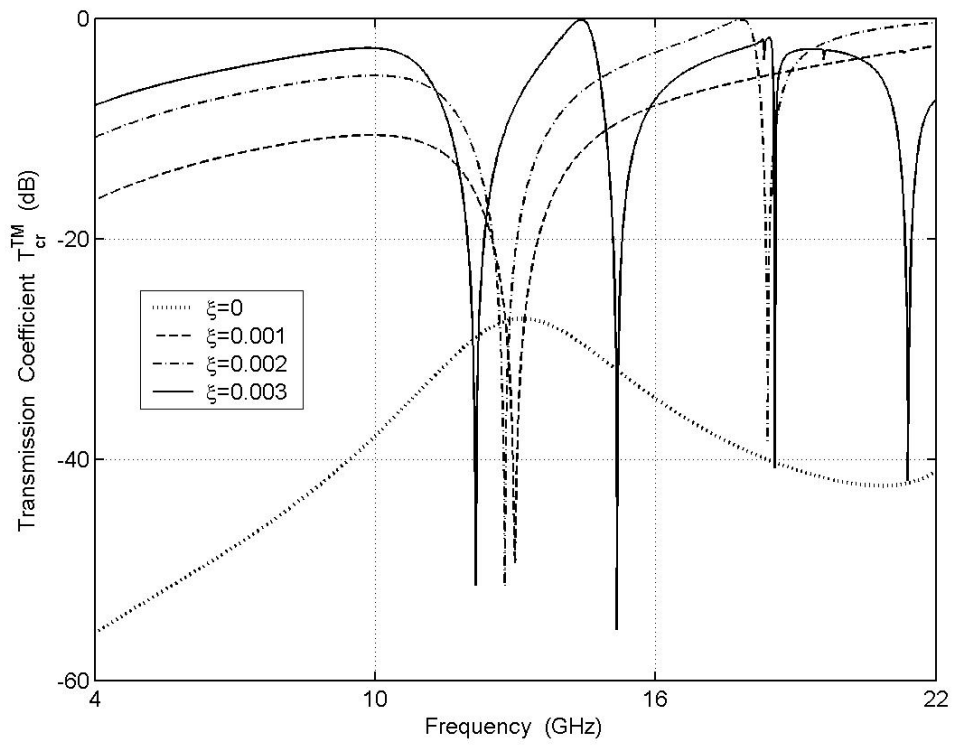
(b)
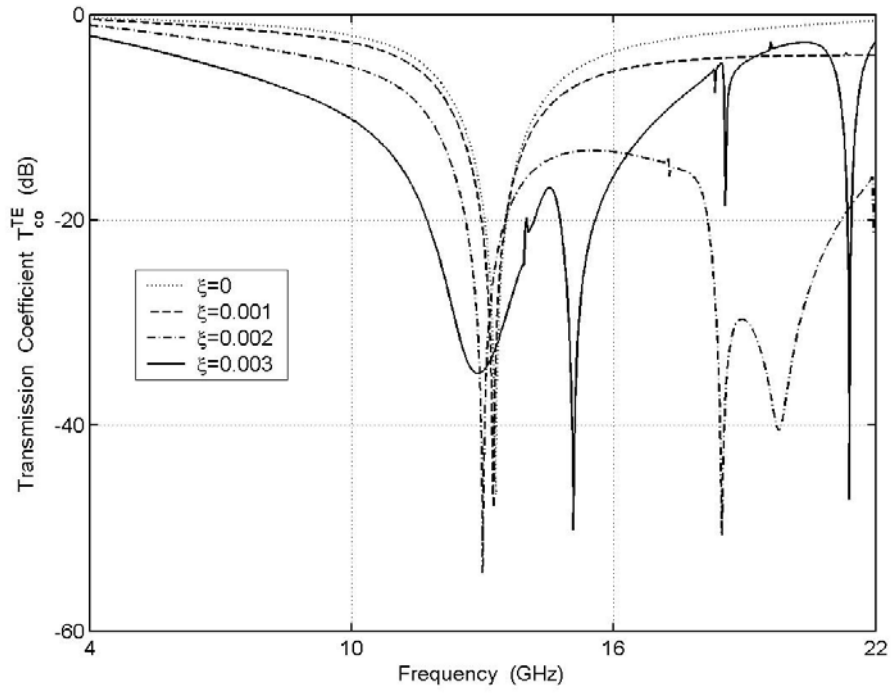
(c)
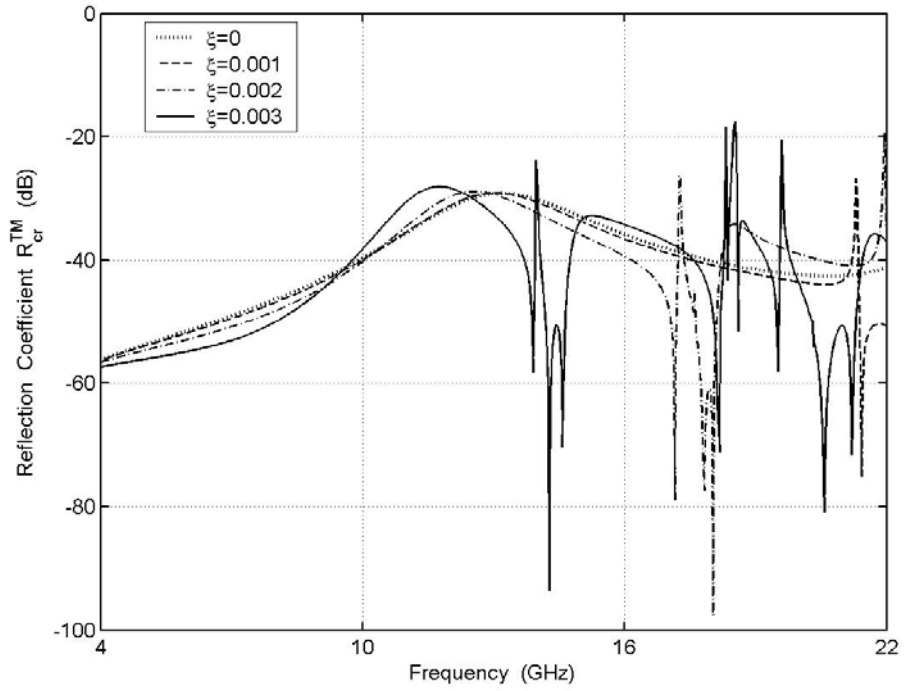
(d)

Figure 2.4 Reflection and transmission coefficients of L–shaped FSS on a chiral slab at different chirality admittances; TE incidence, $\theta=\phi=0°$, $d=0.5$ cm, $\varepsilon_r=1.6$, $w=0.09$ cm, $h_1=h_2=0.9$ cm, $d_1=d_2=0.93$cm, (*a*) Reflection Coefficient R_{co}^{TE}, (b) Transmission Coefficient T_{cr}^{TM}, (c) Transmission Coefficient T_{co}^{TE}, (d) Reflection Coefficient R_{cr}^{TM}

51
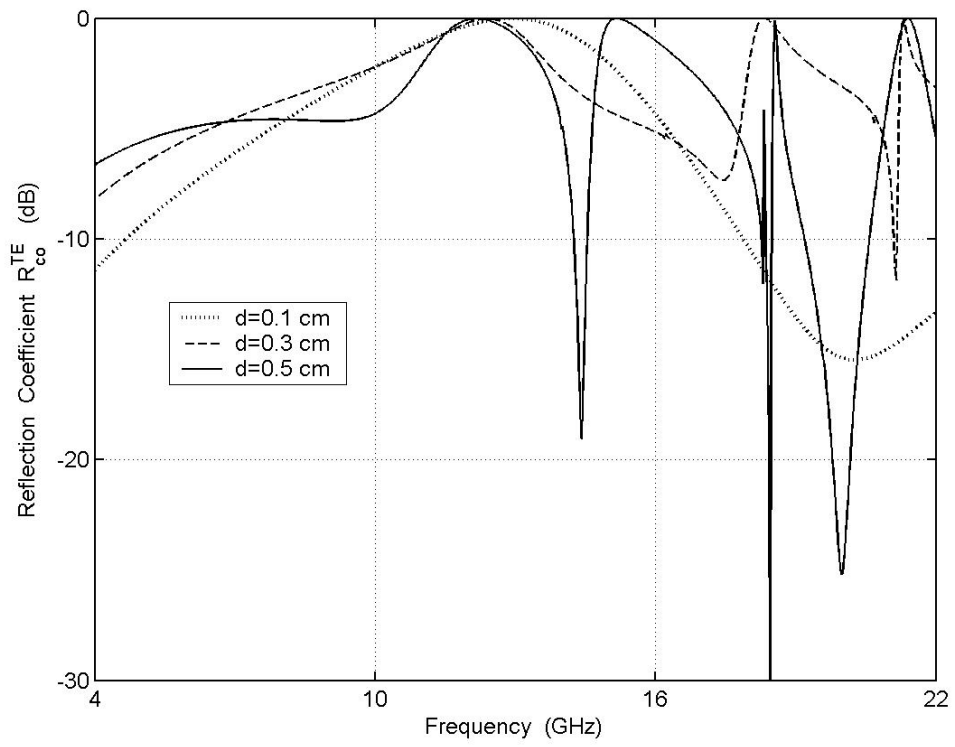
(*a*)
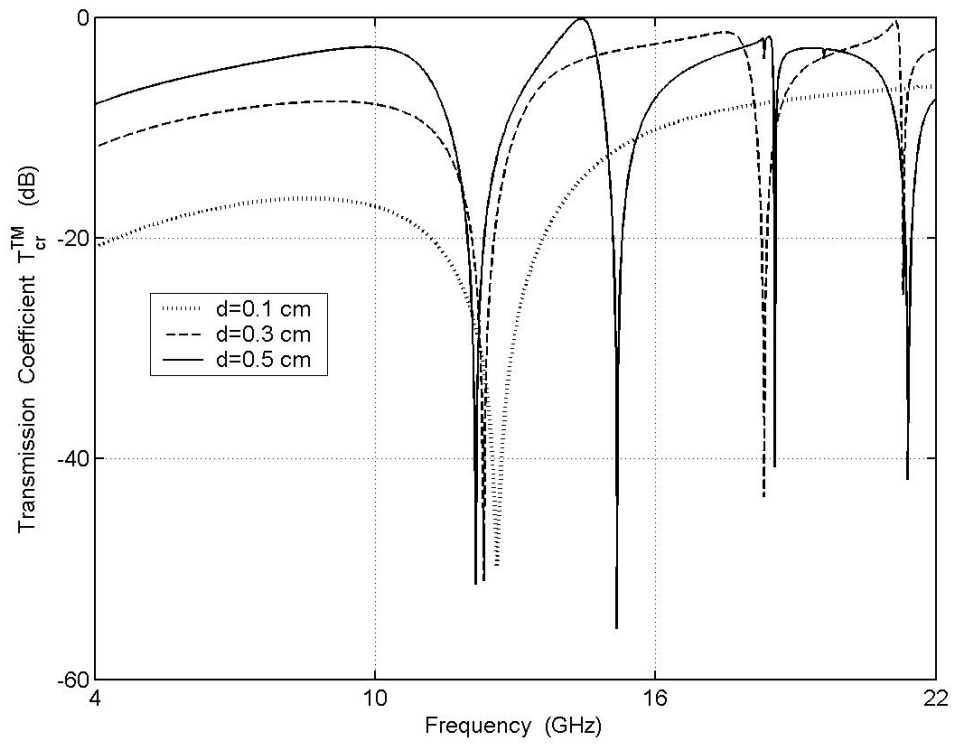
(b)
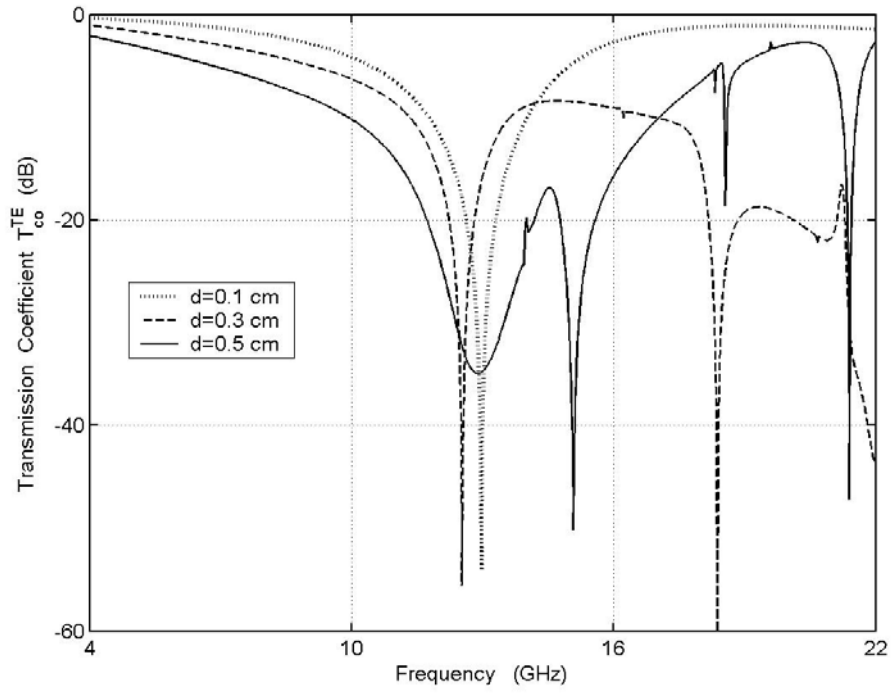
(c)
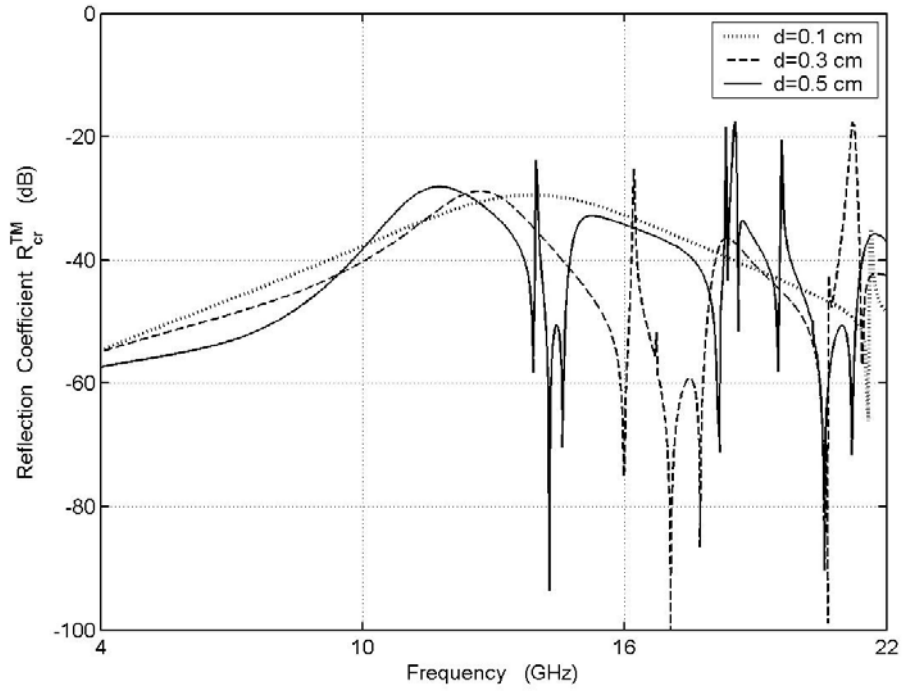
(d)

Figure 2.5 Reflection and transmission coefficients of L–shaped FSS on a chiral slab at different slab thicknesses; TE incidence, $\theta=\phi=0°$, $\xi=0.003$ S, $\varepsilon_r=1.6$, $w=0.09$ cm, $h_1=h_2=0.9$ cm, $d_1=d_2=0.93$ cm, (a) Reflection Coefficient R_{co}^{TE}, (b) Transmission Coefficient T_{cr}^{TM}, (c) Transmission Coefficient T_{co}^{TE}, (d) Reflection Coefficient R_{cr}^{TM}

53

(*a*)

(b)

54
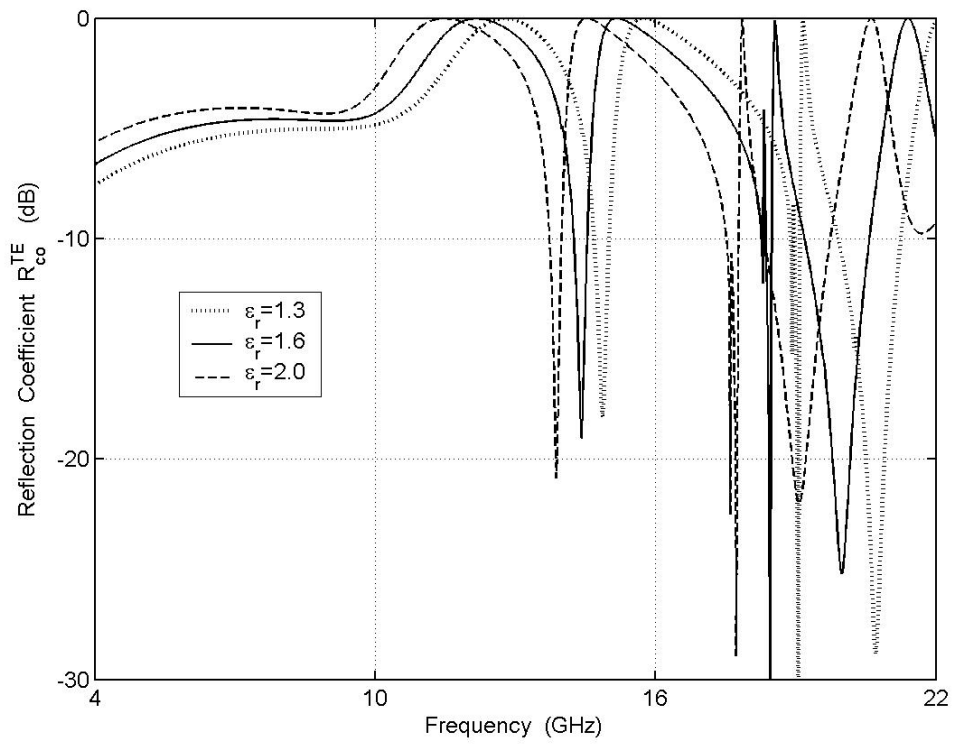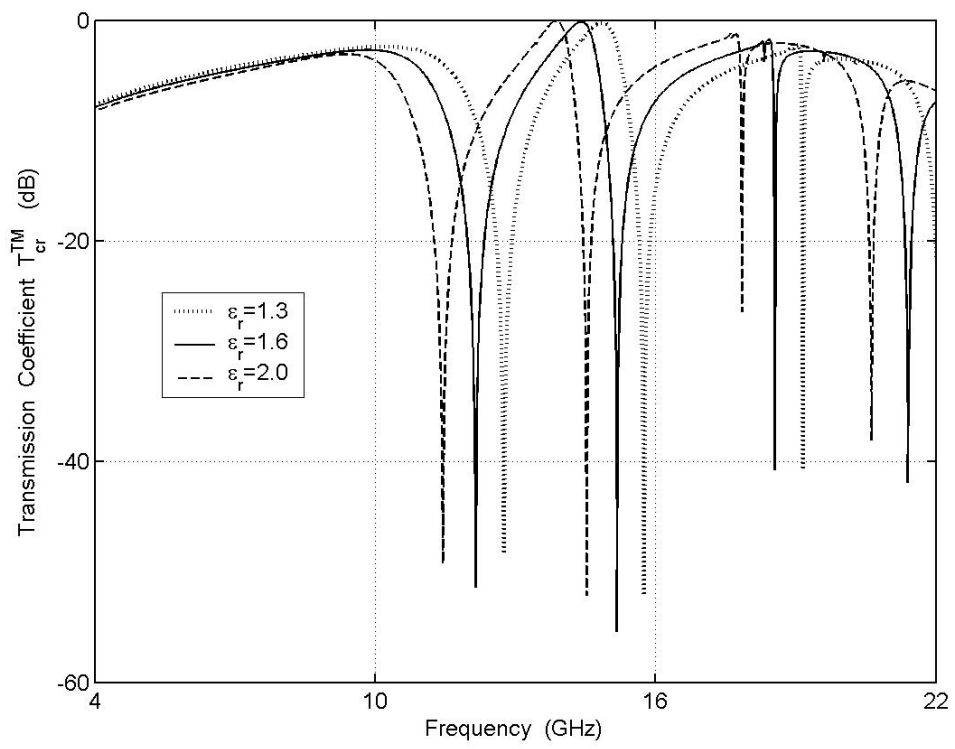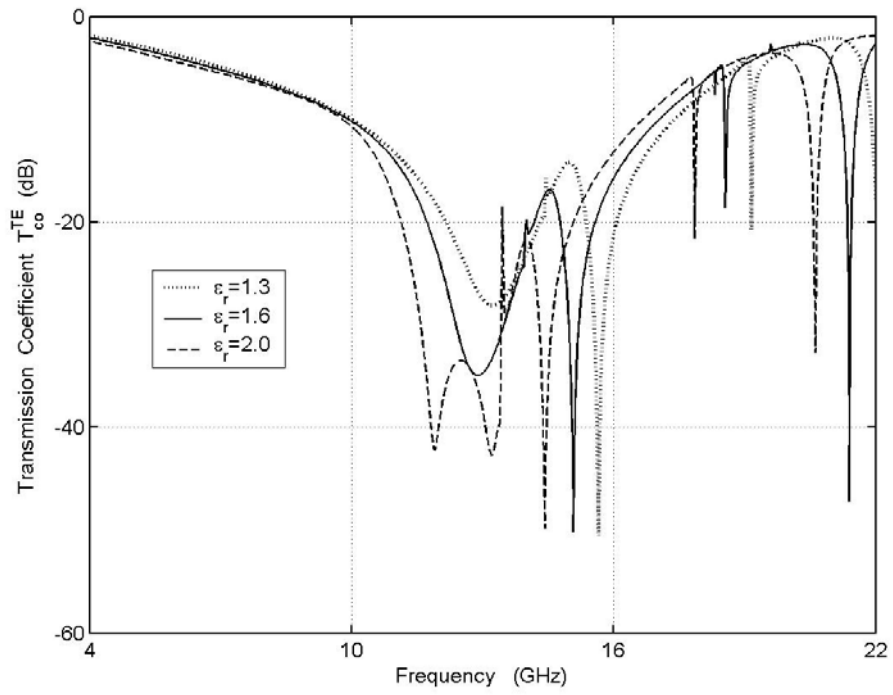
(c)
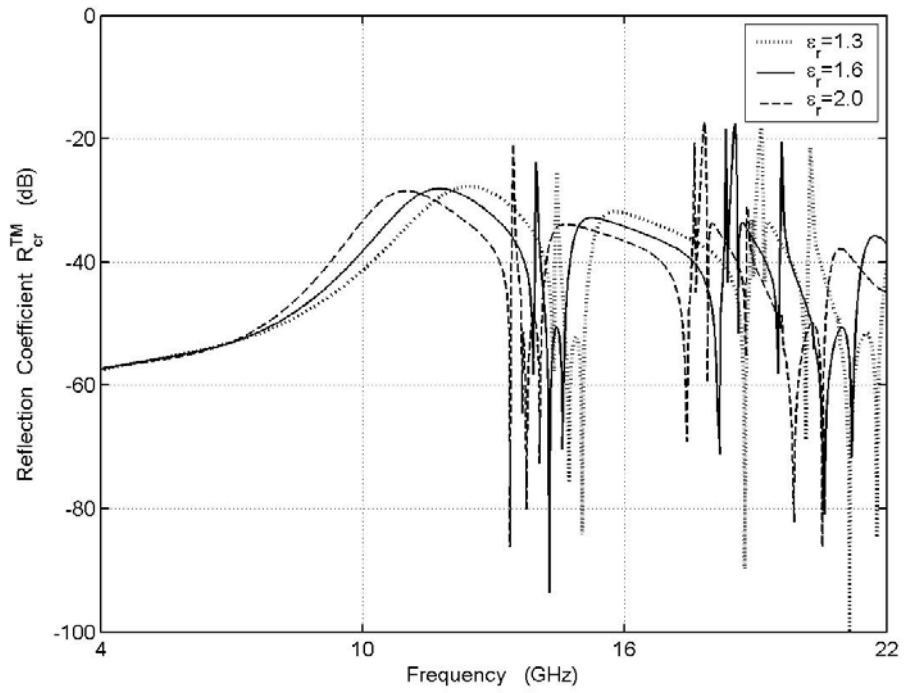
(d)

Figure 2.6 Reflection and transmission coefficients of L–shaped FSS on a chiral slab at different dielectric constants; TE incidence, $\theta=\phi=0°$, $\xi=0.003$ S, $d=0.5$ cm, $w=0.09$ cm, $h_1=h_2=0.9$ cm, $d_1=d_2=0.93$ cm, (a) Reflection Coefficient R_{co}^{TE}, (b) Transmission Coefficient T_{cr}^{TM}, (c) Transmission Coefficient T_{co}^{TE}, (d) Reflection Coefficient R_{cr}^{TM}

55

(*a*)

(b)
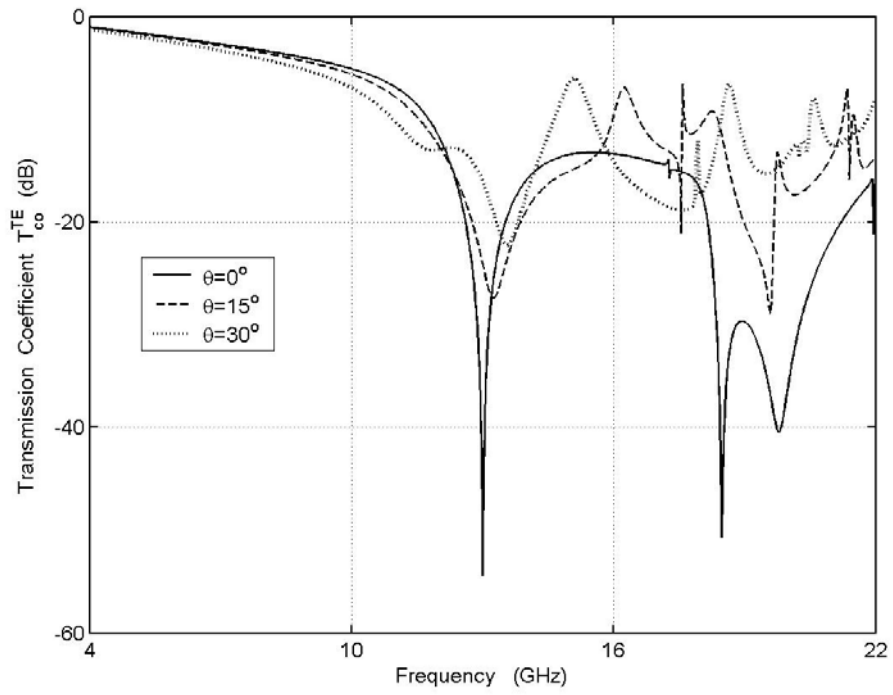
(c)

(d)

Figure 2.7 Reflection and transmission coefficients of L–shaped FSS on a chiral slab at different incident angles; TE incidence, ϕ=0°, ξ=0.002 S, d=0.5 cm, ε_r=1.6, w=0.09 cm, h_1=h_2=0.9 cm, d_1=d_2=0.93 cm, (*a*) Reflection Coefficient R_{co}^{TE}, (b) Transmission Coefficient T_{cr}^{TM}, (c) Transmission Coefficient T_{co}^{TE}, (d) Reflection Coefficient R_{cr}^{TM}

57

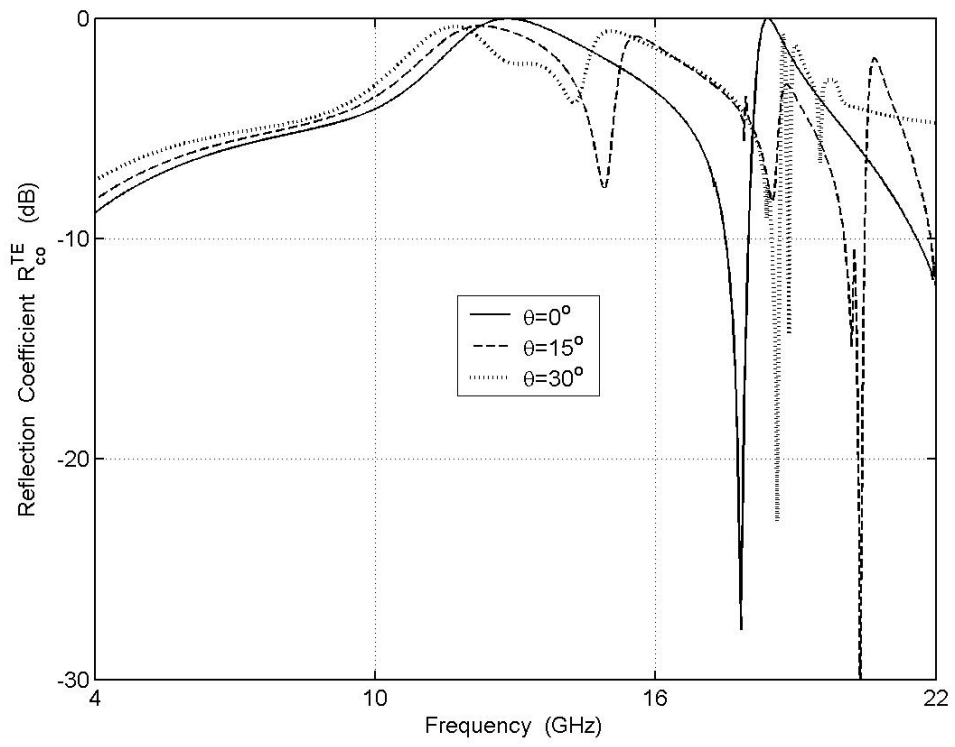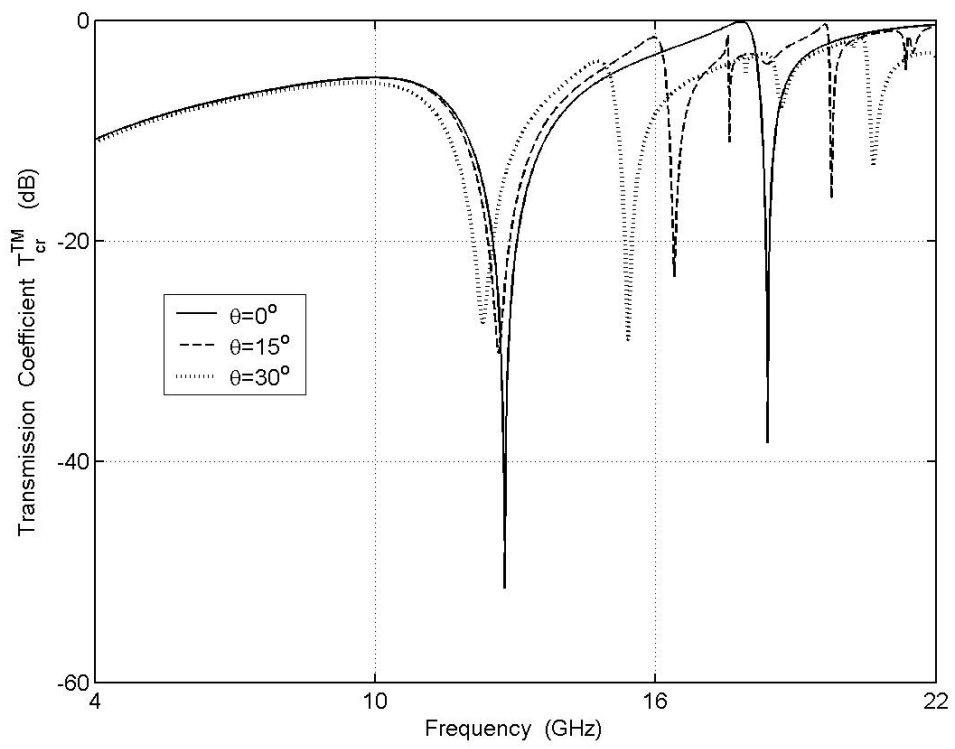Figure 2.8 illustrates the variation of chirality admittance for TM wave at normal incidence. The resonant frequencies are the same with TE incident wave but there are some differences in co– and cross–polarized reflection and transmission coefficients of TM and TE wave at normal incidence. Especially, the deep null points and sharp notches are seen on the reflection and transmission curves for TM incident wave. The incident electric field will not only induce current on FSS elements, but also scatter in the forward as well as the backscatter direction. The net result is that the various array fields can interfere and produce nulls. As seen in Figure 2.8*a* we notice some spurious resonances around 20 GHz. Usually, these resonances are not of great concern, since they in general are very sharp and strongly reduces by a minor amount of loss either from the dielectric or resistivity of the FSS elements. As the chirality admittance increases, multiple resonances are seen. The bandwidth of the fundamental resonance is wider than the others. As depicted in Figure 2.8b, anti–resonances are observed for high values of chirality admittance. At low value of chirality admittances, the magnitude of T_{co}^{TM} is very close to the achiral case (ξ=0), as shown in Figure 2.8c. The magnitude of T_{co}^{TM}, decreases up to frequency of 11.5 GHz. The magnitude of R_{cr}^{TM} and R_{cr}^{TE} are the same for chiral backed FSS at normal incidence, which is less than –20 dB, as shown in Figures 2.4d and 2.8d. The variation of slab thicknesses for TM wave is depicted in Figure 2.9. Multiple resonances are observed for thick dielectric slab, as shown in Figure 2.9*a*. There is approximately, full transmission for cross–polarization in the frequency region of 15–18 GHz as given in Figure 2.9b. Anti–resonances exist for a thicker chiral slab. The magnitude of T_{co}^{TM} decreases in the frequency region of up to 12 GHz as illustrated in Figure 2.9c. The magnitude of R_{cr}^{TE} is less than –20 dB, which is given in Figure 2.9d. Figure 2.10 depicts the oblique angle variation. At normal incidence two resonant frequencies are appeared at 12.8 and 18.4 GHz as shown in Figure 2.10*a*. The second resonance disappeared at oblique angle of incidence. The first resonance has wider bandwidth and nearly the same up to 30° of incidence. At 30° of incidence there is also full transmission for cross–polarized field at 20 GHz as depicted in Figure 2.10b. At normal incidence deep nulls are seen in transmission curves at resonant frequencies. These nulls are filled at oblique angle incidences. The null is also filled for T_{co}^{TM} at oblique angle of incidence as shown in Figure 2.10c.

The magnitude of T_{co}^{TM} is nearly the same for oblique incidence up to 8 GHz. The magnitude of cross polarization increases in the frequency region up to 12 GHz, as given in Figure 2.10d. In the frequency region of 12–20 GHz, the magnitude is greater than the normal incidence case. The plotted Figures 2.11 and 2.12 illustrate the current amplitude versus stretched out length, induced on the L–shaped FSS elements backed by chiral slab, at resonant frequencies of ξ=0.003 S for TE and TM wave incidences, respectively. At resonant frequency, the incident electric field induces more current in the parallel arm while it induces less current in the perpendicular arm of the L–shaped FSS for both type of polarization. On the contrary to dielectric slab, the induced currents are not the same, especially in the perpendicular arms, due to chiral medium for the TE and TM incident waves.

(a)

(b)

60
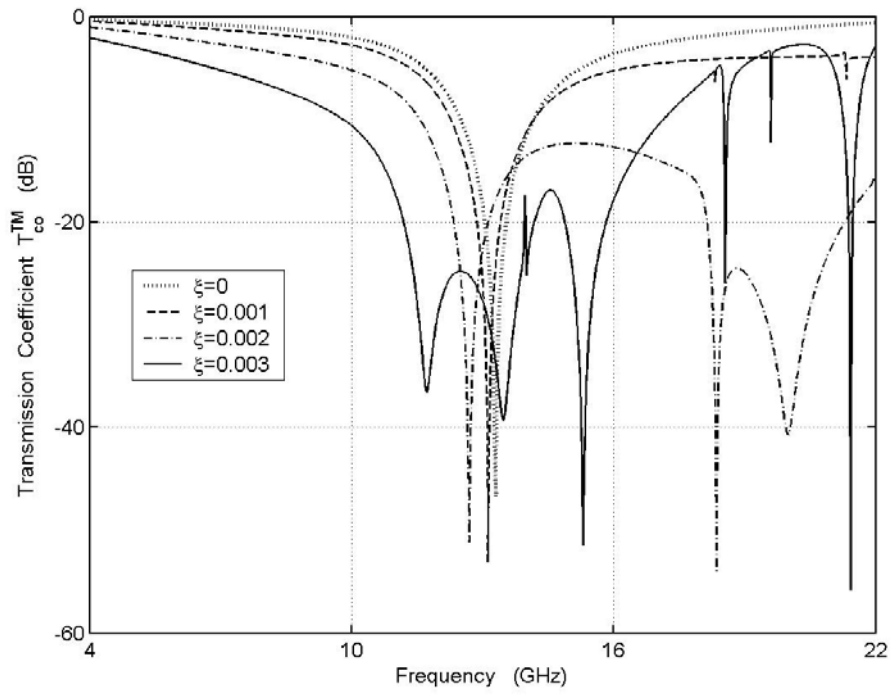
(c)
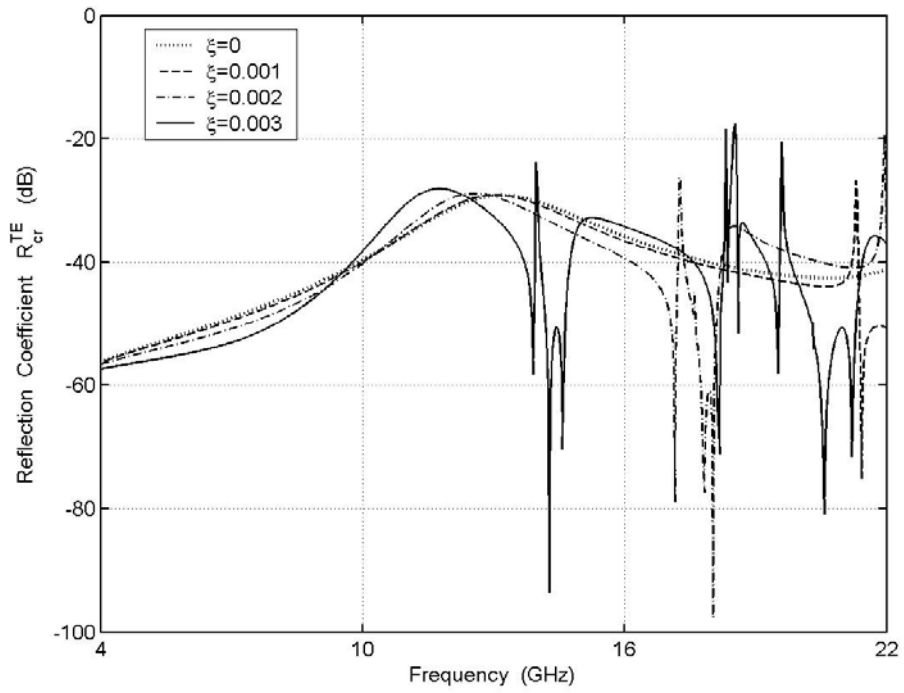
(d)

Figure 2.8 Reflection and transmission coefficients of L–shaped FSS on a chiral slab at different chirality admittances; TM incidence, $\theta=\phi=0°$, $d=0.5$ cm, $\varepsilon_r=1.6$, $w=0.09$ cm, $h_1=h_2=0.9$ cm, $d_1=d_2=0.93$ cm, (*a*) Reflection Coefficient R_{co}^{TM}, (*b*) Transmission Coefficient T_{cr}^{TE}, (c) Transmission Coefficient T_{co}^{TM}, (d) Reflection Coefficient R_{cr}^{TE}
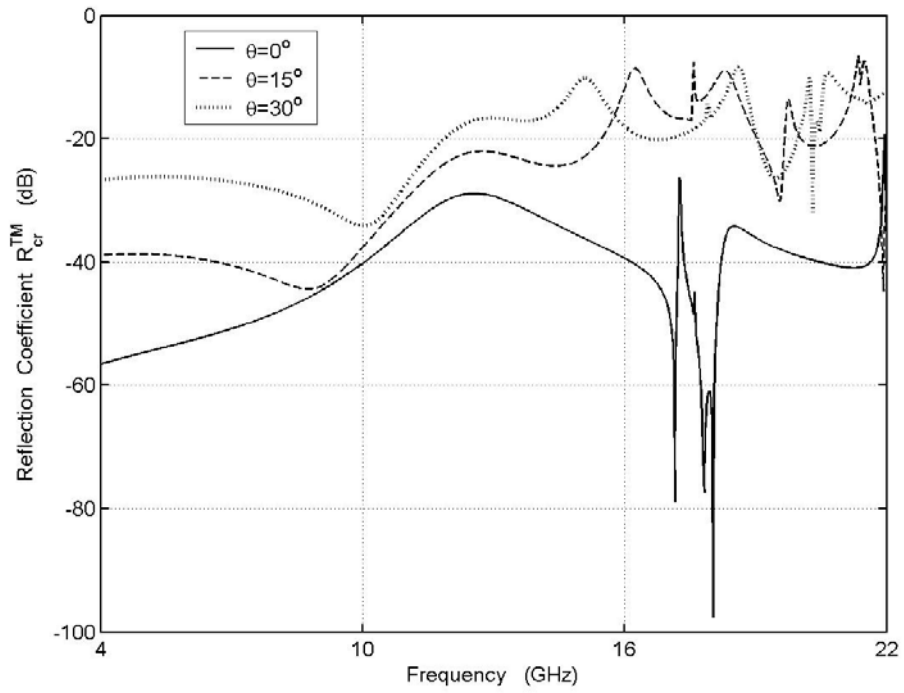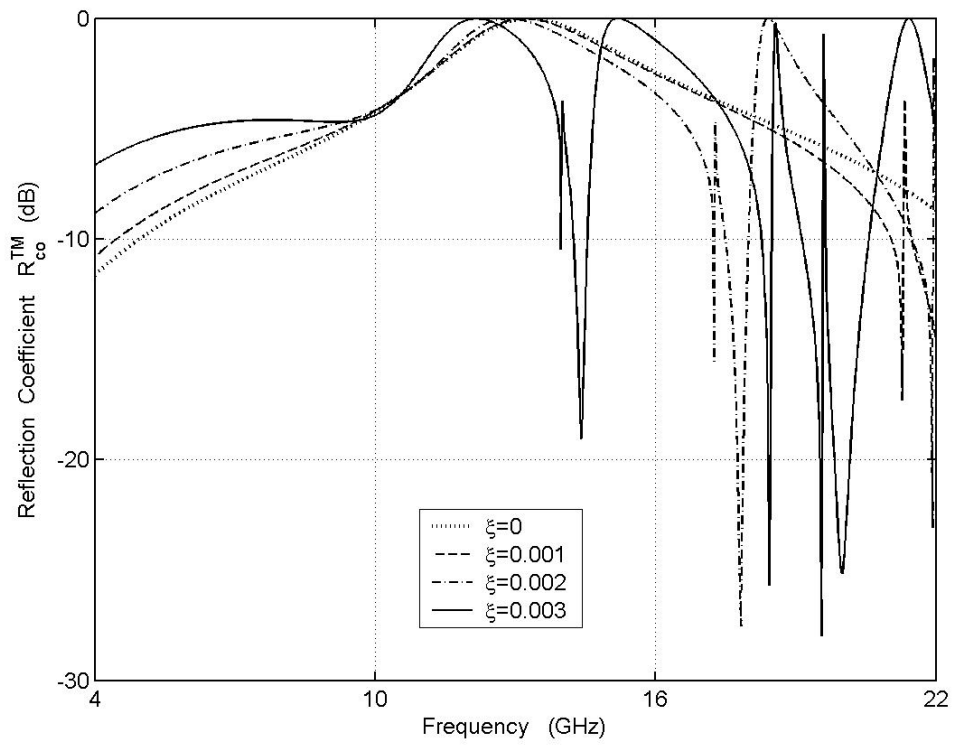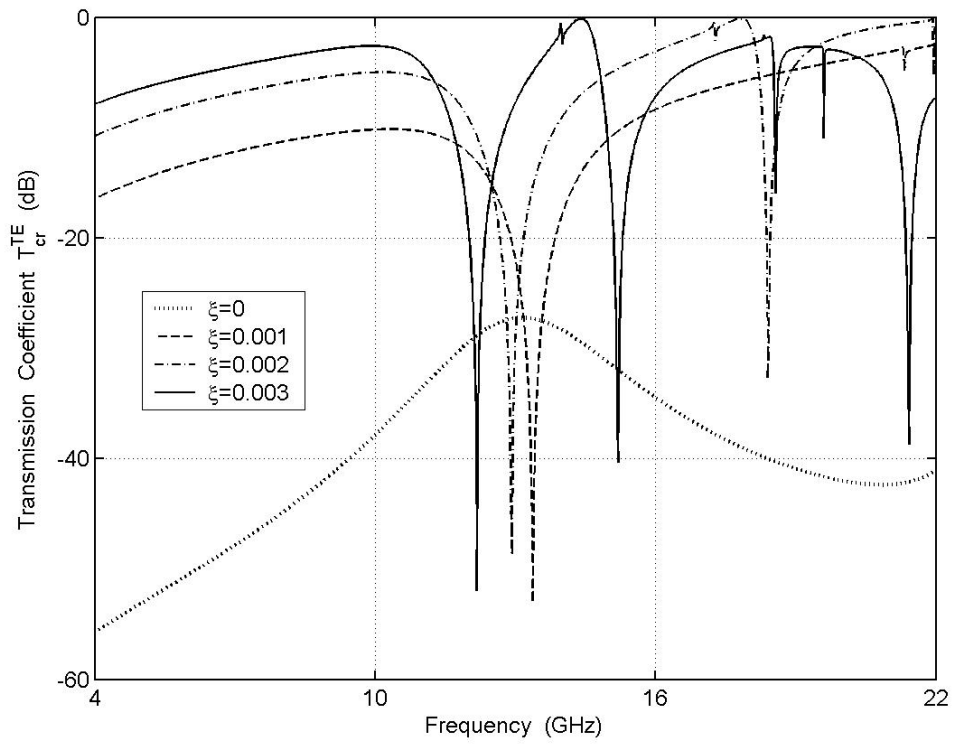
61

(a)

(b)

62
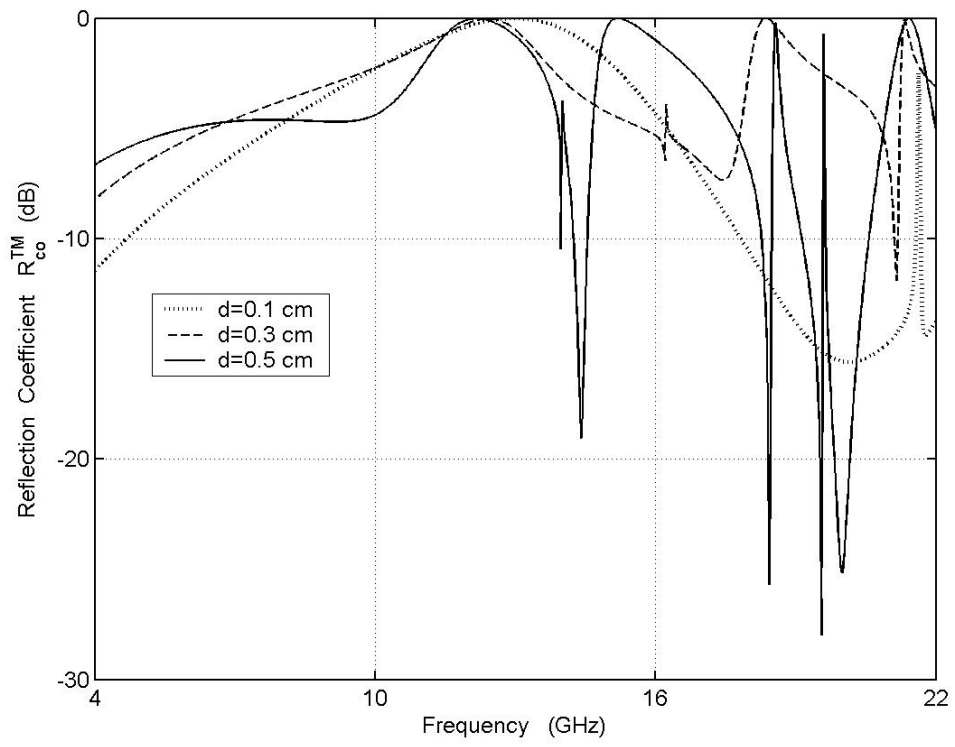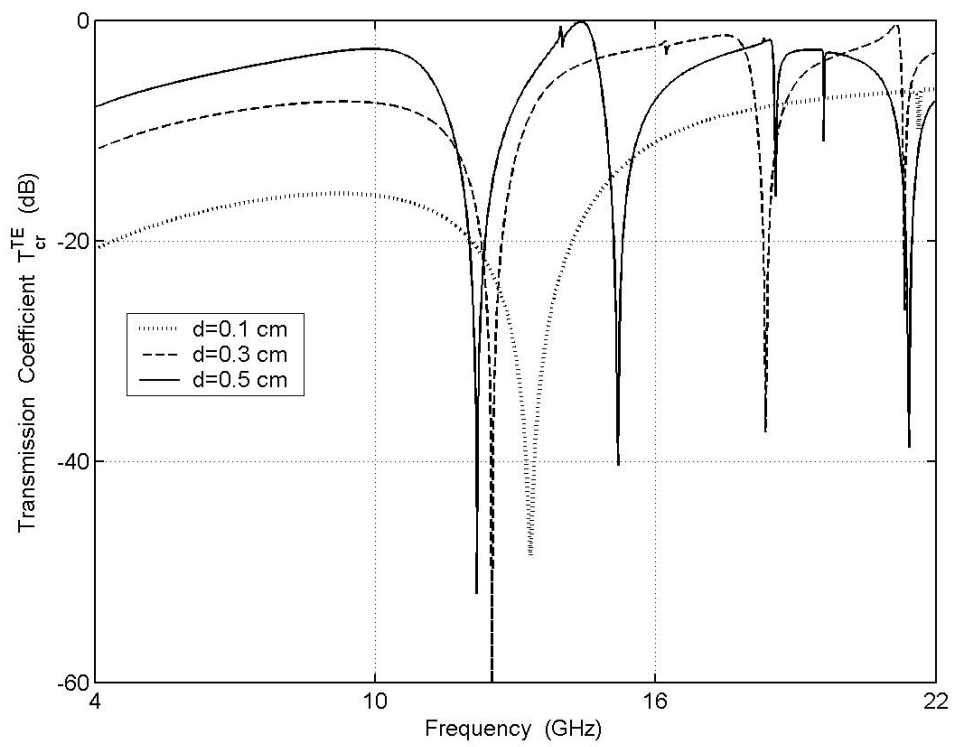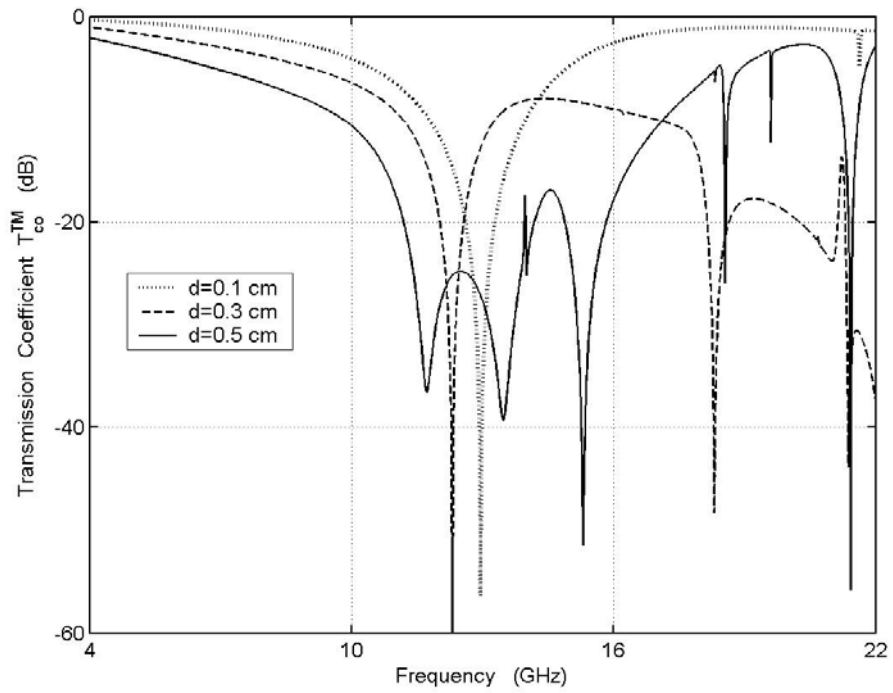
(c)
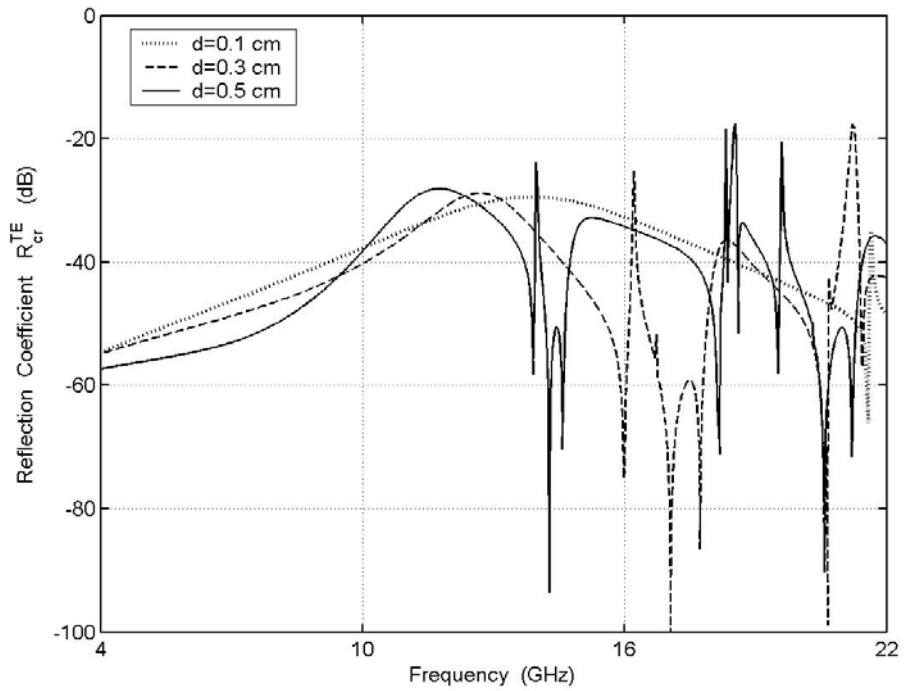
(d)

Figure 2.9 Reflection and transmission coefficients of L–shaped FSS on a chiral slab at different slab thicknesses; TM incidence, $\theta=\phi=0°$, $\xi=0.003$ S, $\varepsilon_r=1.6$, $w=0.09$ cm, $h_1=h_2=0.9$ cm, $d_1=d_2=0.93$ cm, (a) Reflection Coefficient R_{co}^{TM}, (b) Transmission Coefficient T_{cr}^{TE}, (c) Transmission Coefficient T_{co}^{TM}, (d) Reflection Coefficient R_{cr}^{TE}

63
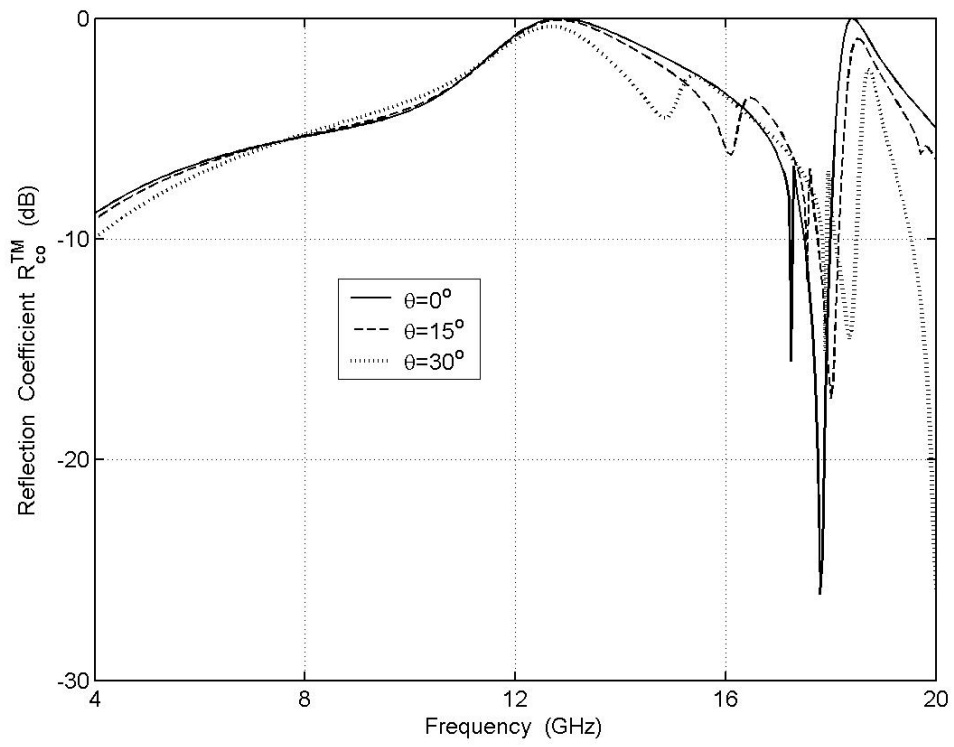
(a)
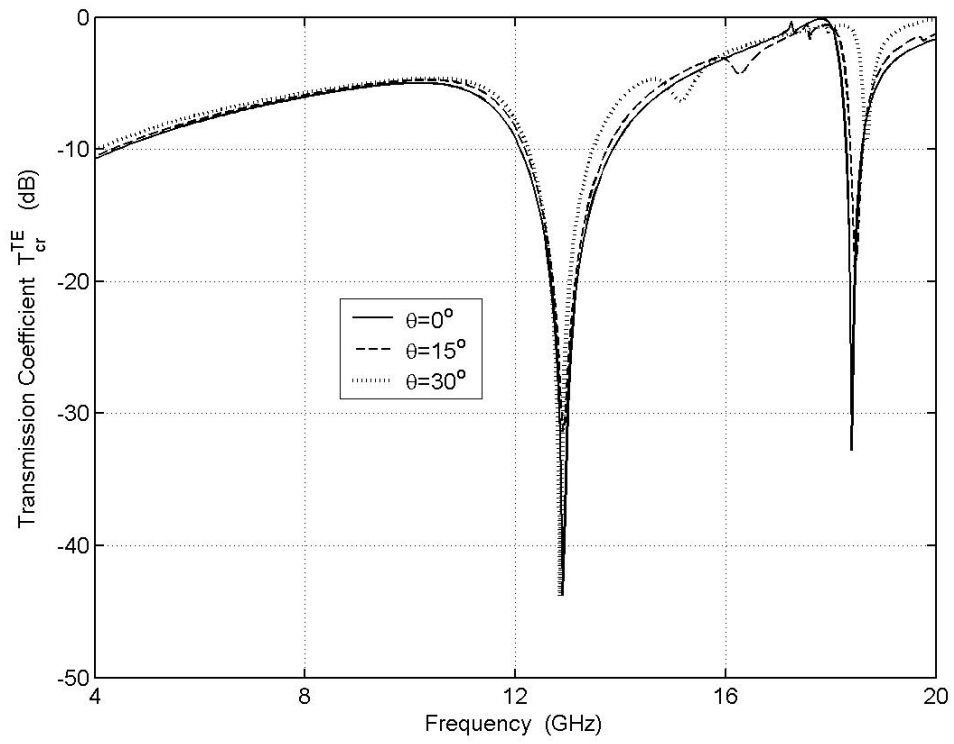
(b)
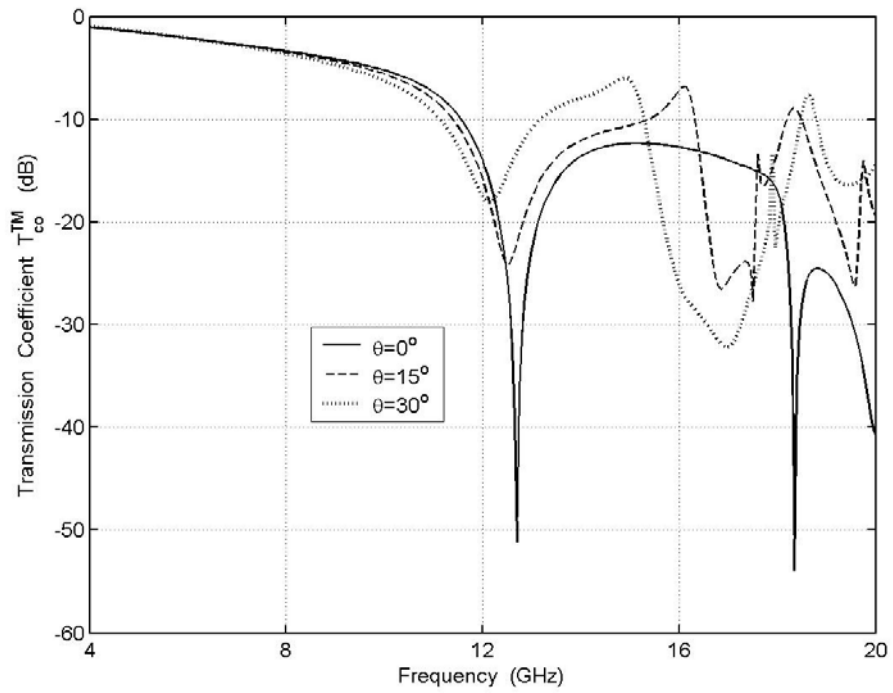
(c)
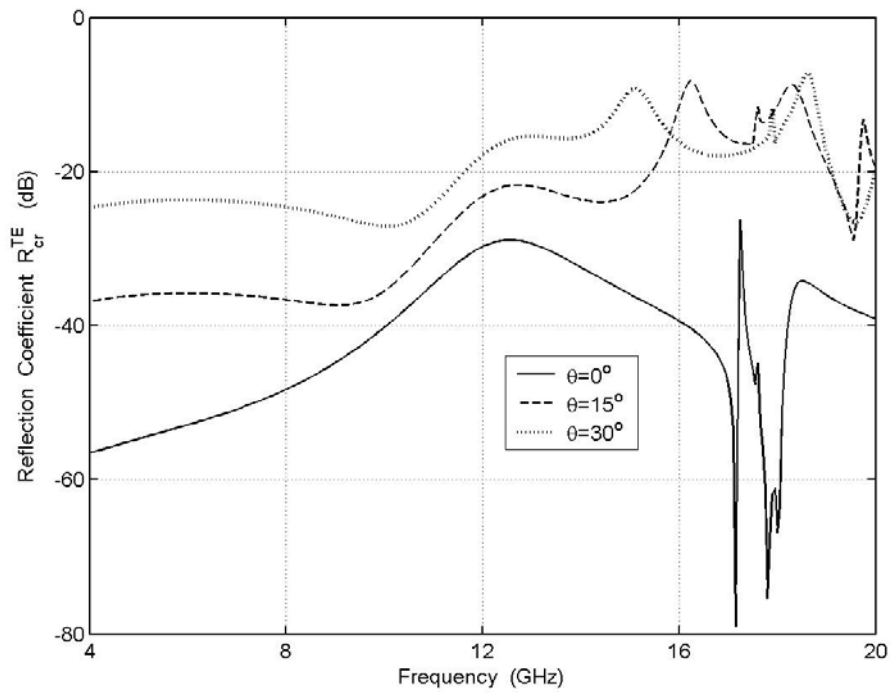
(d)

Figure 2.10 Reflection and transmission coefficients of L–shaped FSS on a chiral slab at different incident angles; TM incidence, $\phi=0°$, $\xi=0.002$ S, $d=0.5$ cm, $\varepsilon_r=1.6$, $w=0.09$ cm, $h_1=h_2=0.9$ cm, $d_1=d_2=0.93$ cm, (a) Reflection Coefficient R_{co}^{TM}, (b) Transmission Coefficient T_{cr}^{TE}, (c) Transmission Coefficient T_{co}^{TM}, (d) Reflection Coefficient R_{cr}^{TE}

65
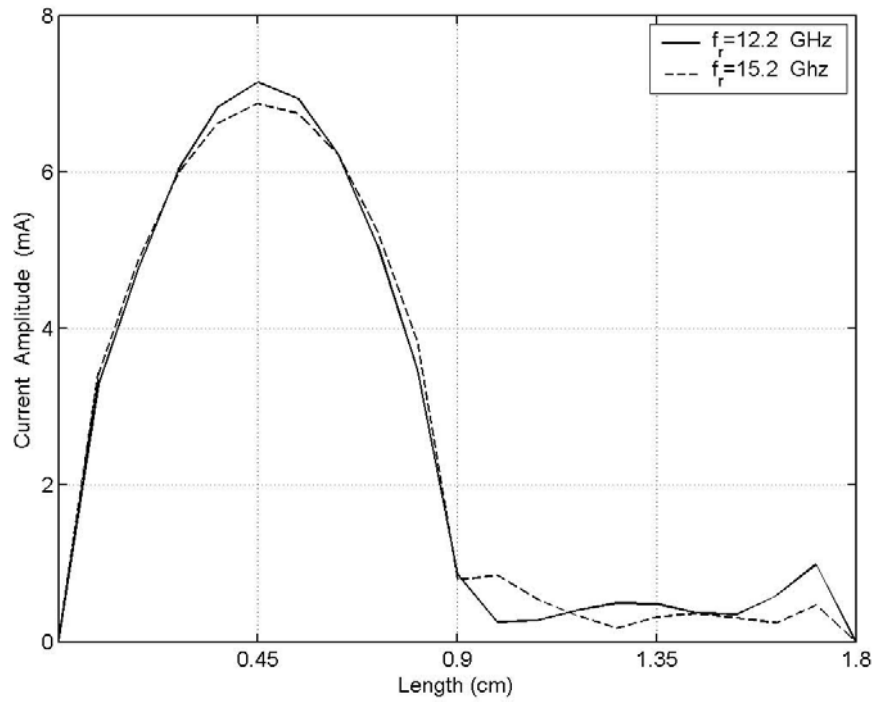
Figure 2.11 Current amplitude versus length at resonant frequencies of L–shaped FSS on a chiral slab TE incidence; $\theta=\phi=0°$, $\xi=0.003$ S, $d=0.5$ cm, $\varepsilon_r=1.6$, $w=0.09$ cm, $h_1=h_2=0.9$ cm, $d_1=d_2=0.93$ cm
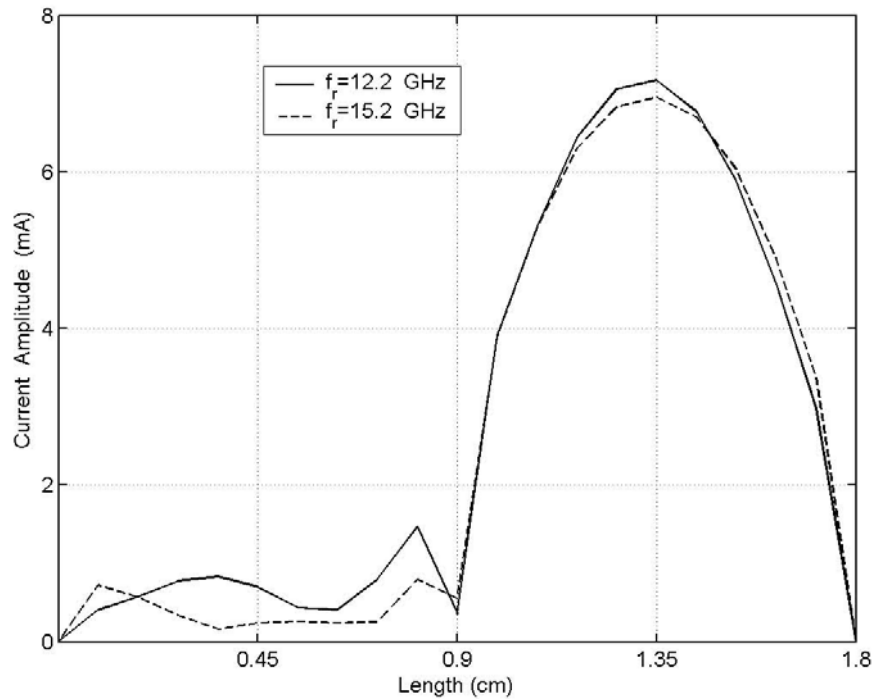
Figure 2.12 Current amplitude versus length at resonant frequencies of L–shaped FSS on a chiral slab TM incidence; $\theta=\phi=0°$, $\xi=0.003$ S, $d=0.5$ cm, $\varepsilon_r=1.6$, $w=0.09$ cm, $h_1=h_2=0.9$ cm, $d_1=d_2=0.93$ cm

66

2.2.3 Numerical Results of One–Turn Square Spiral FSS on a Chiral Slab

The numerical results of one–turn square spiral FSS backed by chiral slab has been presented for TE and TM incident plane waves. The co– and cross–polarized reflection and transmission coefficients are plotted with respect to frequency for different values of chirality admittance, slab thickness and incident angle. The length of the first segment is h_1=0.16 cm and the other lengths can be found from the relation h_n=$n*h_1$ for n=2, 3, 4. The width is chosen as one tenth of the first length (w=h_1/10=0.016 cm). The inter–element spacings d_1 and d_2 are equal to 0.7 cm and 0.73 cm for TE and TM wave incidences, respectively. The periodic cells are arranged in square lattice (β=90°). The total length of one–turn square spiral is approximated by 25 PWS current functions to determine the unknown coefficients. The number of Floquet modes used in the computations is 625. The co– and cross– polarized reflection and transmission coefficients are plotted against frequency at normal incidence for different values of medium parameters such as chirality admittance and slab thickness. The coefficients are also plotted for TE and TM incident waves at oblique incidence.

Figure 2.13 shows the variation of chirality admittance at normal incidence of TE wave for one–turn square spiral FSS on a chiral slab. In Figure 2.13a, at low chirality admittance (dashed curve) only one resonant frequency is seen, while at high chirality admittances two resonant frequencies are observed. In the frequency region of 1–12.5 GHz, the magnitude of R_{co}^{TE} increases, as the chirality admittance increases. The two peaks are approximately equal in terms of bandwidth for ξ=0.002. The bandwidth of the first peak is very narrow than the second one for ξ=0.003. As shown in Figure 2.13b, the magnitude of T_{cr}^{TM} is less than –20 dB for an achiral case (ξ=0). At low chirality, ξ=0.001, no polarization conversion is observed. There are two anti–resonant peaks for ξ=0.002 at 18 and 22 GHz. When ξ=0.003, there is one anti–resonant frequency at about 15 GHz The magnitude of T_{co}^{TE} reduces up to 19.5 GHz as the value of chirality admittance is varied from 0 to 0.002, as illustrated in Figure 2.13c. The magnitude is also decreasing up to 13.5 GHz for ξ=0.003 value. Some extra peaks are seen for ξ=0.003 in the frequency region of 13.5–25 GHz. The

magnitude of the last peak is close to unity. The magnitude of the cross–polarized reflection coefficient is very low, that is why it is not plotted.

The variation of slab thickness is shown in Figure 2.14. The resonant frequency is stable at 23 GHz, as seen in Figure 2.14a. The magnitude of T_{cr}^{TM} increases as slab thickness increases up to 22 GHz, as depicted in Figure 2.14b. Around resonant frequency, there is no more change in magnitude. The magnitude of T_{co}^{TE} decreases for increasing value of slab thickness as illustrated in Figure 2.14c. At resonant frequency the T_{co}^{TE} and T_{cr}^{TM} each have a null.

The reflection and transmission coefficients for oblique incidence are shown in Figure 2.15. The resonant frequency occurs at around 23 GHz at normal incidence TE wave as shown in Figure 2.15a. In the frequency region of 1–17 GHz, the magnitude of R_{co}^{TE} increases, as the chirality admittance increases. For an oblique incidence of $30°$ and $45°$, more than one resonant frequency has been seen. The resonant frequency shifts to the lower end as the angle of incidence increases. As can be depicted in Figure 2.15b, the magnitudes of the cross–polarized transmission coefficients are approximately equal to each other in the frequency region of 1–9 GHz. No anti–resonance is observed for obliquely incident TE wave. There is a slight decrease in the magnitude of T_{co}^{TE} up to 19 GHz, as illustrated in Figure 2.15c.

(a)

(b)

69
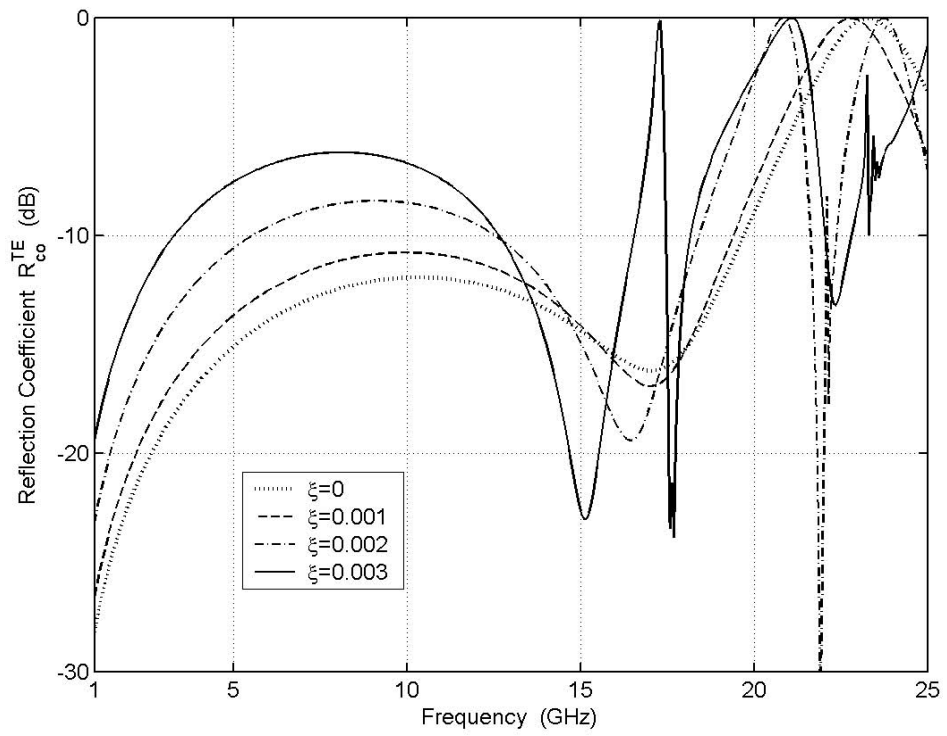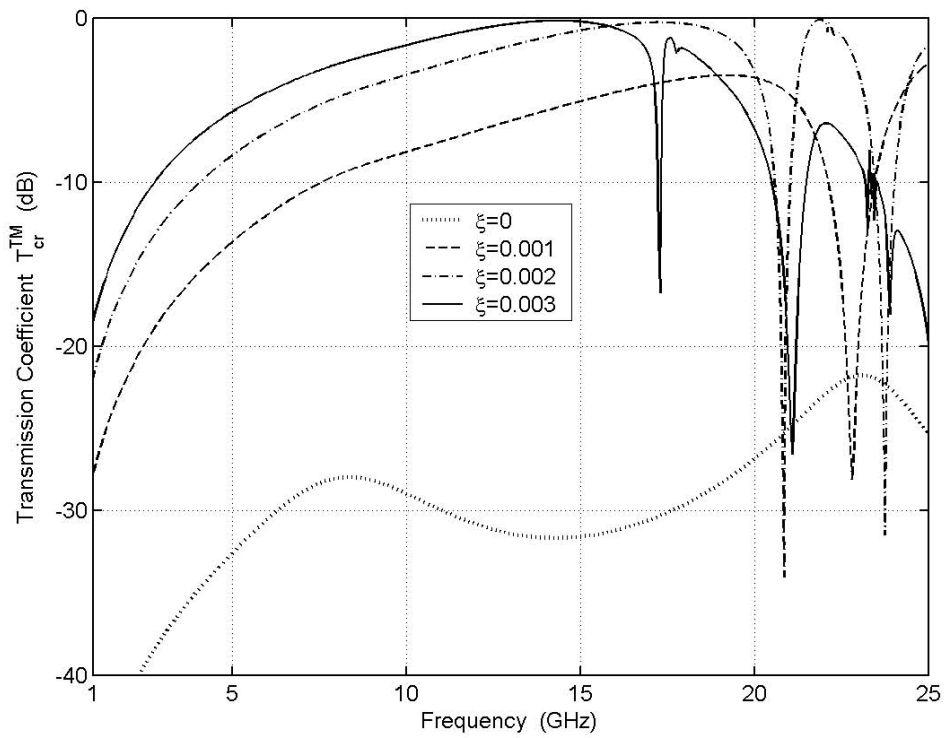
(c)

Figure 2.13 Reflection and transmission coefficients of one–turn square spiral FSS on a chiral slab at different chirality admittances; TE incidence, $\theta=\phi=0°$, $d=0.5$ cm, $\varepsilon_r=1.6$, $w=0.016$ cm, $h_1=0.16$ cm, $h_n=n*h_1$ cm, n=2,3,4., $d_1=d_2=0.7$ cm, (*a*) Reflection Coefficient R_{co}^{TE}, (b) Transmission Coefficient T_{cr}^{TM}, (c) Transmission Coefficient T_{co}^{TE}

(*a*)

(b)

(c)

Figure 2.14 Reflection and transmission coefficients of one–turn square spiral FSS on a chiral slab at different slab thicknesses; TE incidence, $\theta=\phi=0°$, $\xi=0.001$ S, $\varepsilon_r=1.6$, $w=0.016$ cm, $h_1=0.16$ cm, $h_n=n*h_1$ cm, n=2,3,4., $d_1=d_2=0.7$ cm, (*a*) Reflection Coefficient R_{co}^{TE}, (b) Transmission Coefficient T_{cr}^{TM}, (c) Transmission Coefficient T_{co}^{TE}

(*a*)

(b)

72

(c)

Figure 2.15 Reflection and transmission coefficients of one–turn square spiral FSS on a chiral slab at different incident angles; TE incidence, $\phi=0°$, $\xi=0.001$ S, $d=0.5$ cm, $\varepsilon_r=1.6$, $w=0.016$ cm, $h_1=0.16$ cm, $h_n=n*h_1$ cm, n=2,3,4., $d_1=d_2=0.7$ cm, (*a*) Reflection Coefficient R_{co}^{TE}, (b) Transmission Coefficient T_{cr}^{TM}, (c) Transmission Coefficient T_{co}^{TE}

Figure 2.16 illustrates the variation of chirality admittance at normal incidence of TM wave for one–turn square spiral FSS on a chiral slab. The first resonance is stable up to $\xi=0.002$ and slightly shifts for $\xi=0.003$, as shown in Figure 2.16*a*. For $\xi=0.003$, three resonant frequencies appear. The first peak is wider than the others. In Figure 2.16b, there is an anti–resonance at 21.5 GHz for $\xi=0.002$. In the frequency region of 1–12 GHz, as the chirality admittance increases, the magnitude of T_{cr}^{TE} increases whereas the magnitude of T_{co}^{TM} reduces as shown in Figure 2.16b and Figure 2.16c, respectively. In the frequency region of 15–25 GHz, the magnitude of T_{co}^{TM} is also decreasing except for $\xi=0.003$. In this frequency region, two peaks, which are close to unity, are seen for $\xi=0.003$.

73

The variation of slab thickness is illustrated in Figure 2.17. Some slight variations are seen in the magnitude of R_{co}^{TM}, but the resonant frequency is not affected from the variation of slab thickness as depicted in Figure 2.17*a*. The resonant frequency happens at about 14 GHz. As shown in Figure 2.17b, the magnitude of T_{cr}^{TE} is increasing corresponding to an increase in slab thickness. Around the resonant frequency, approximately no variation was observed in the curves. The magnitude of T_{co}^{TM} is not affected from the variation of slab thickness up to resonant frequency as shown in Figure 2.17c. After the resonant frequency the magnitude of T_{co}^{TM} reduces corresponding to an increase in slab thickness.
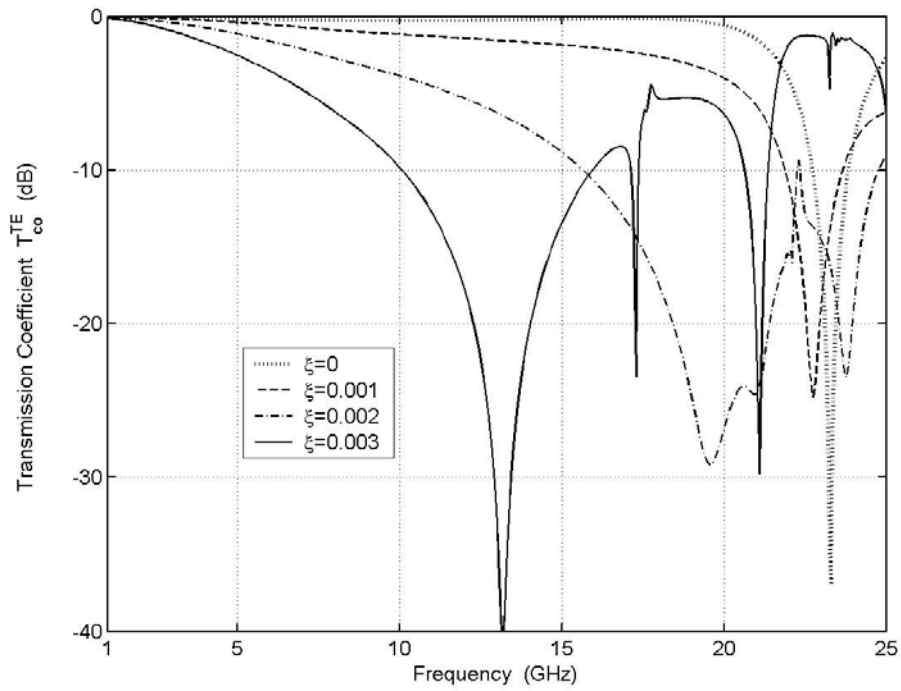
The reflection and transmission coefficients for oblique incidence TM wave are shown in Figure 2.18. The resonant frequency shifts to right side for oblique angle of incidence, as shown in Figure 2.18*a*. For an obliquely incident wave the magnitude of R_{co}^{TM} increases up to resonance frequency. There is only one resonant frequency for oblique incidence of up to $45°$. No anti–resonance is observed for an obliquely incident TM wave as shown in Figure 2.18b. The magnitude of T_{cr}^{TE} increases for an obliquely incident wave up to 14 GHz. There is no variation in the magnitude of T_{co}^{TM} up to 11 GHz, as shown in Figure 2.18c. The magnitude of T_{co}^{TM} is decreasing in the frequency region of 11–14 GHz.

Figures 2.19 and 2.20 illustrate the current amplitude versus stretched out length of one–turn square spiral FSS backed by chiral slab at resonant frequency. The vertical grids show the corner points of the one–turn square spiral element. For TE plane wave at normal incidence the current has a greater peak at the longest (third one) segment as shown in Figure 2.19. For TM plane wave at normal incidence the current amplitude versus stretched out length is shown in Figure 2.20. Most of the current is induced on the fourth segment of one–turn square spiral element which is the longest and parallel to applied electric field. The currents at two resonant frequencies are approximately close to each other.
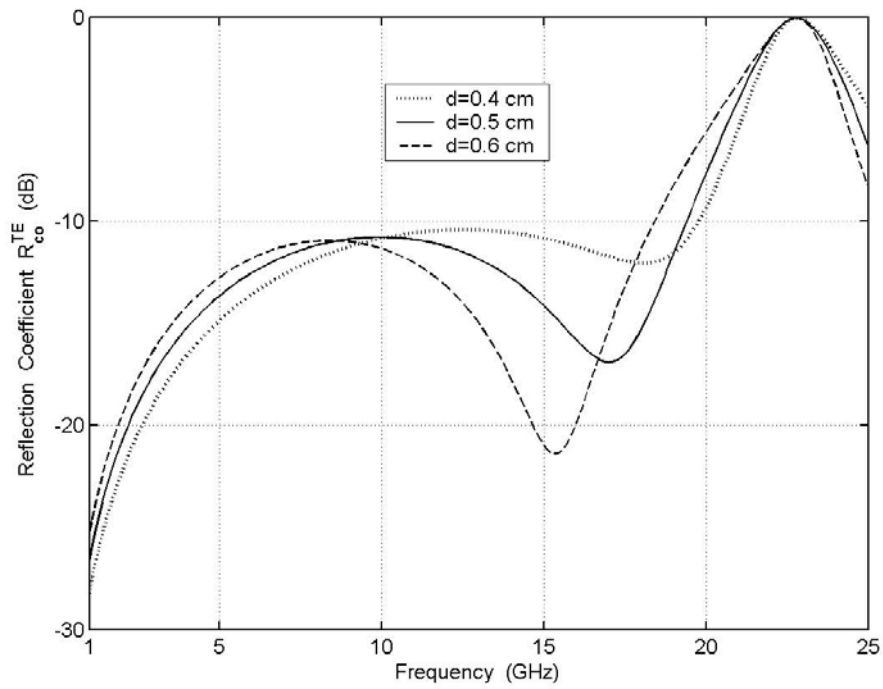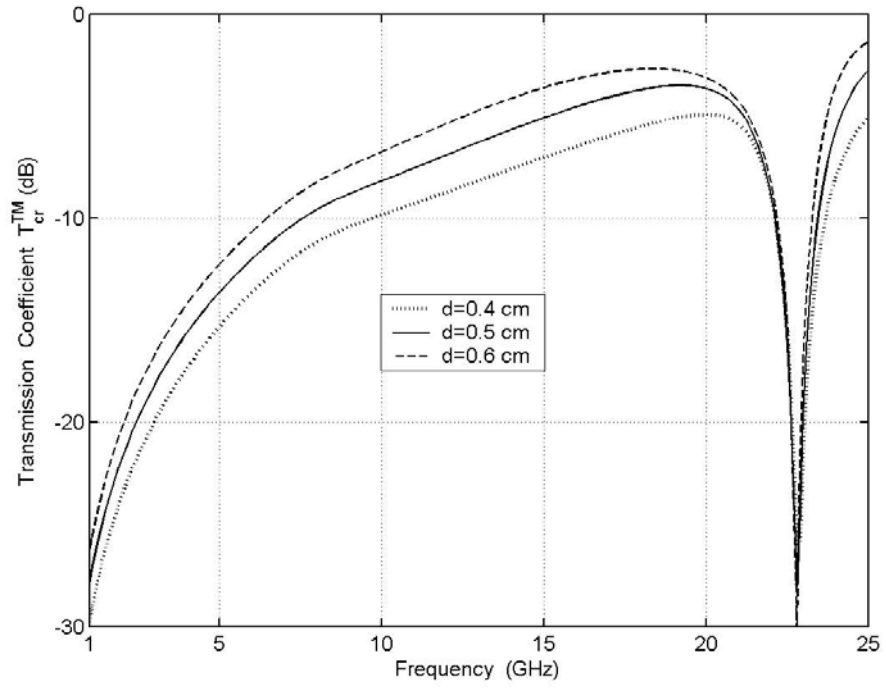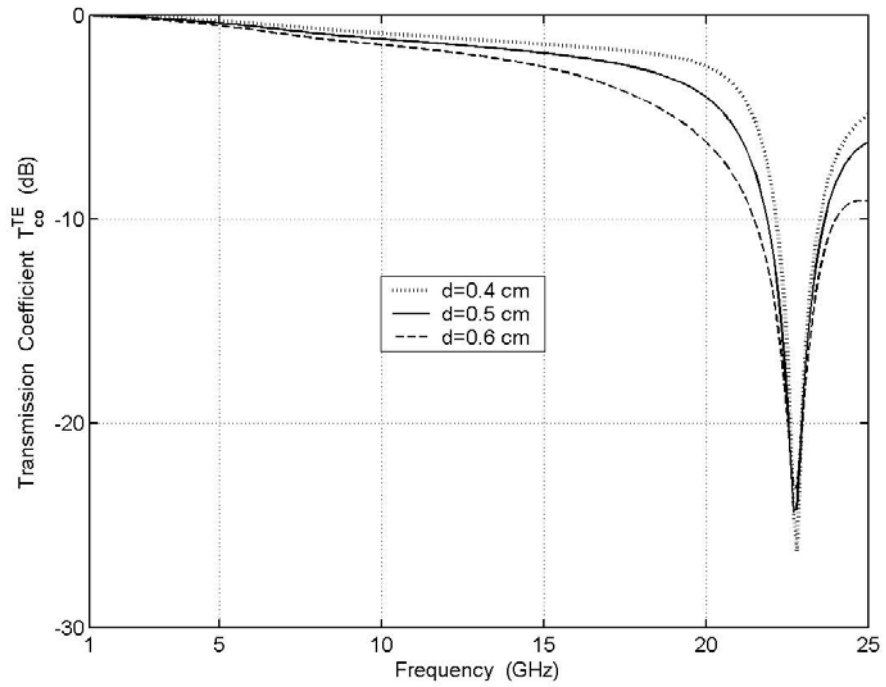
(*a*)
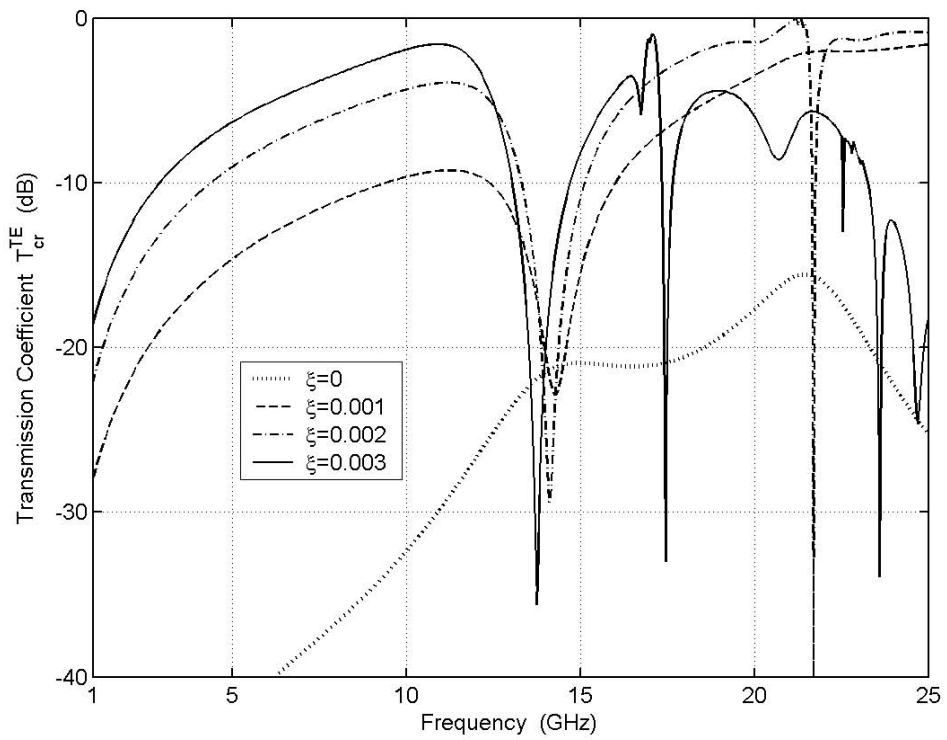
(b)
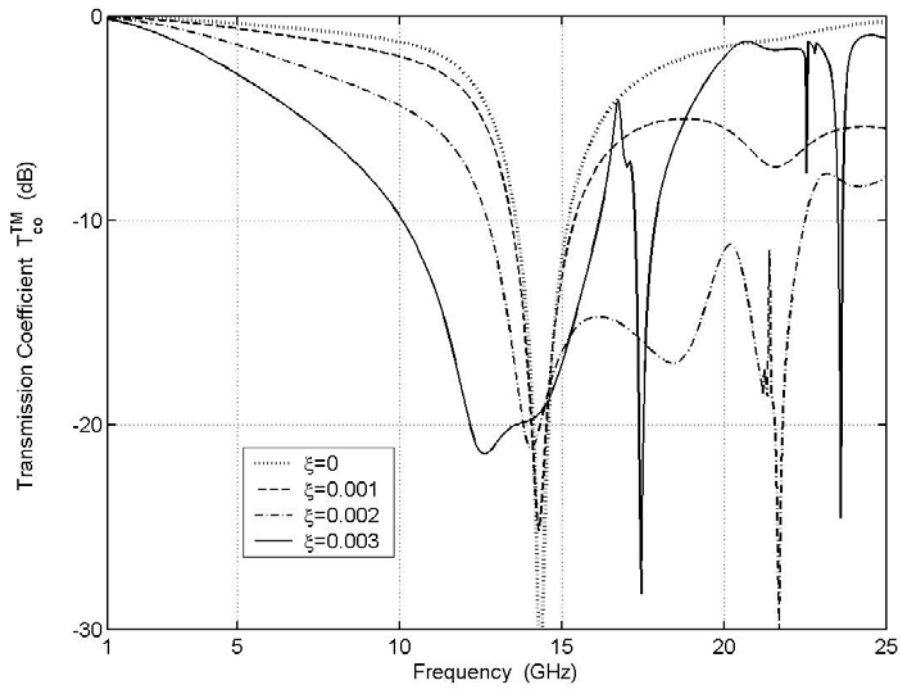
(c)

Figure 2.16 Reflection and transmission coefficients of one–turn square spiral FSS on a chiral slab at different chirality admittances; TM incidence, $\theta=\phi=0°$, d=0.5 cm, ε_r=1.6, w=0.016 cm, h_1=0.16cm, h_n=n*h_1 cm, n=2,3,4., d_1=d_2=0.73 cm, (*a*) Reflection Coefficient R_{co}^{TM}, (b) Transmission Coefficient T_{cr}^{TE}, (c) Transmission Coefficient T_{co}^{TM}
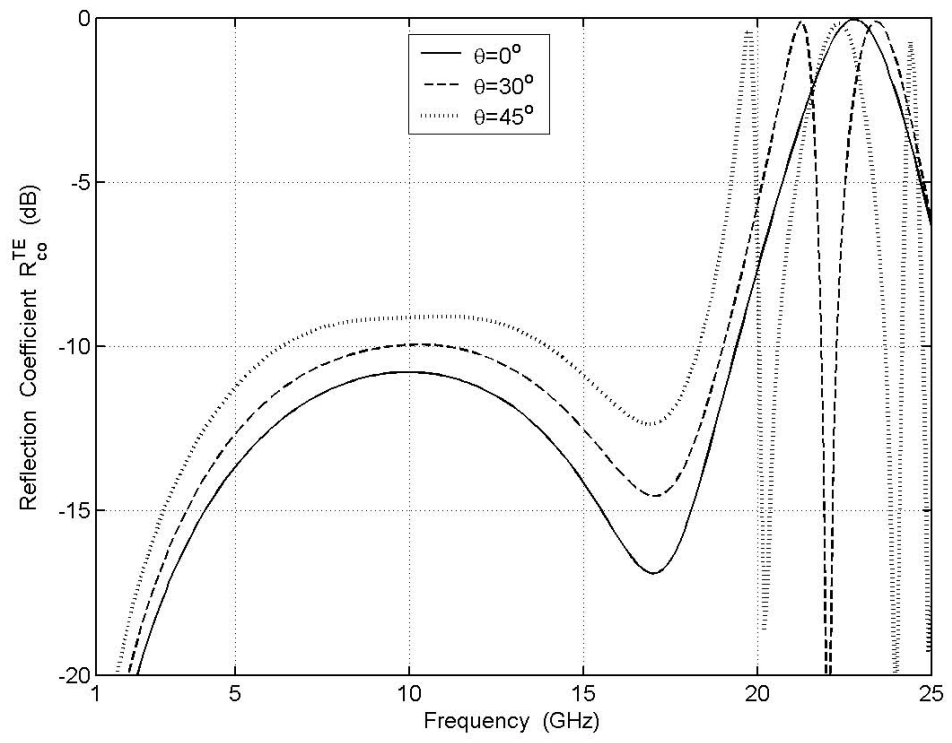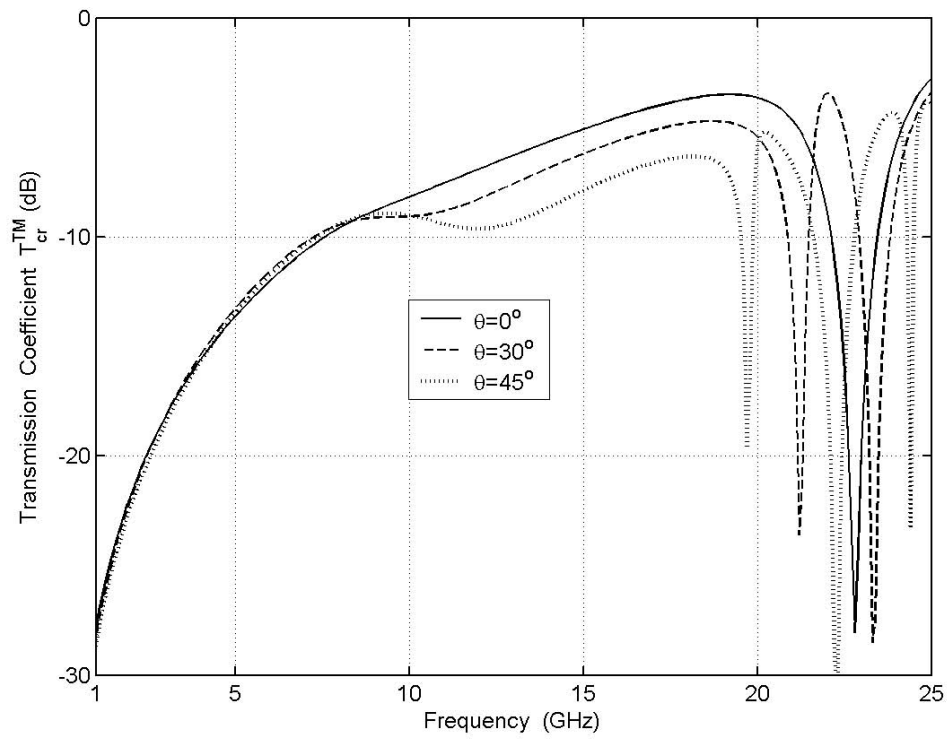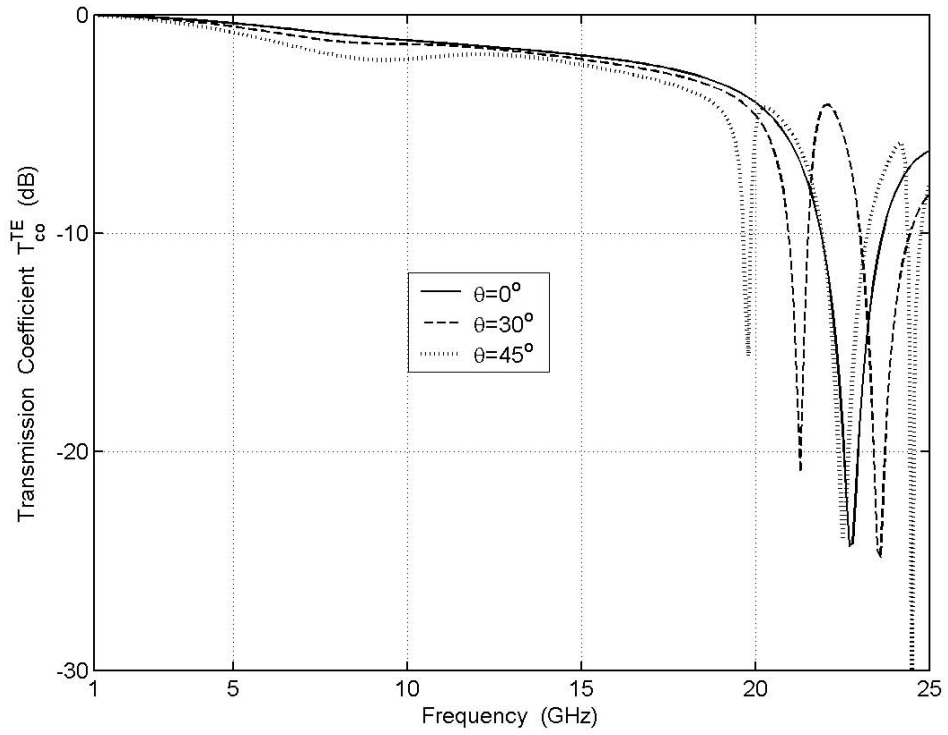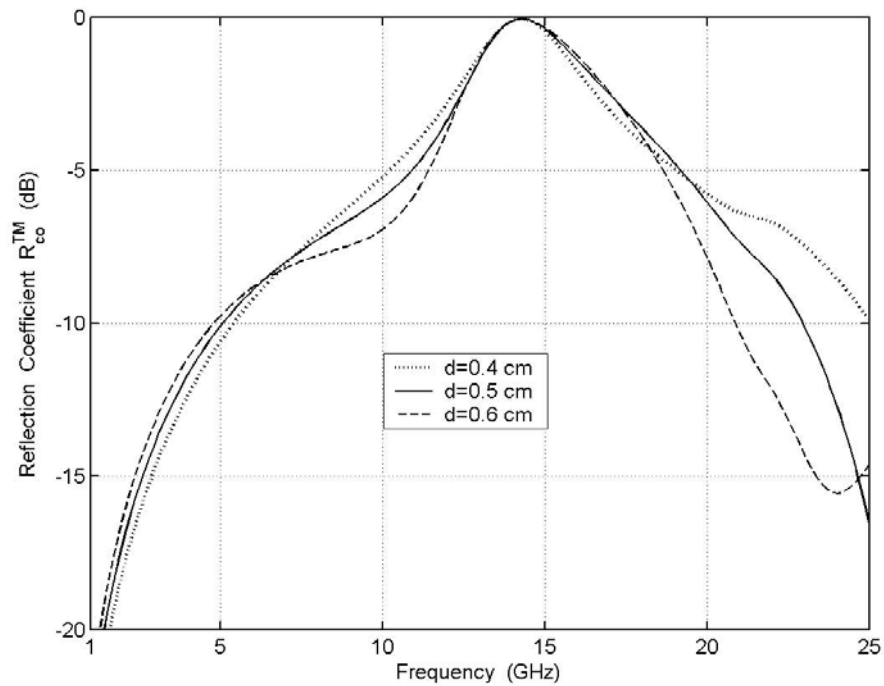

(*a*)
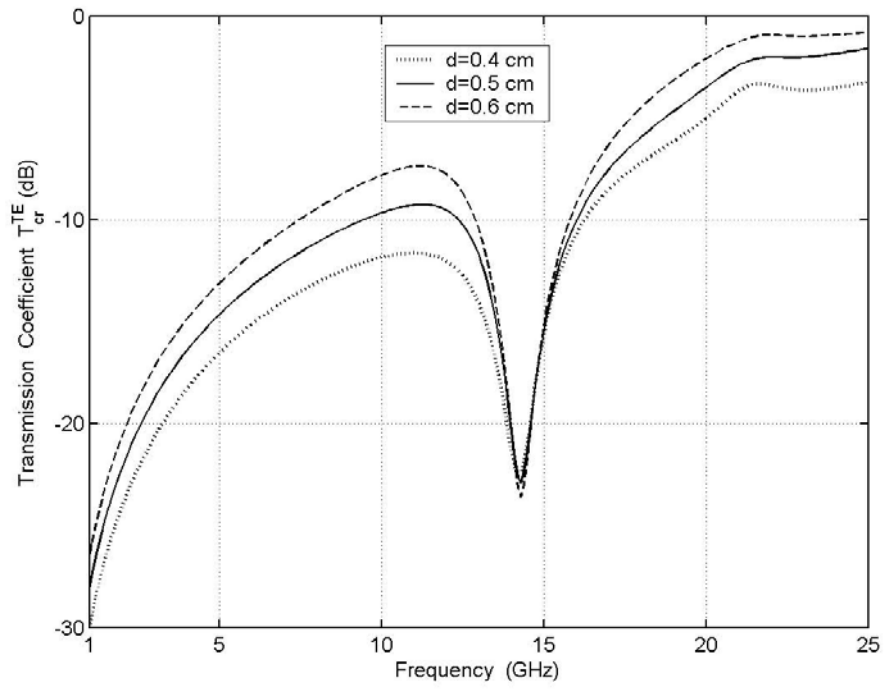
(b)
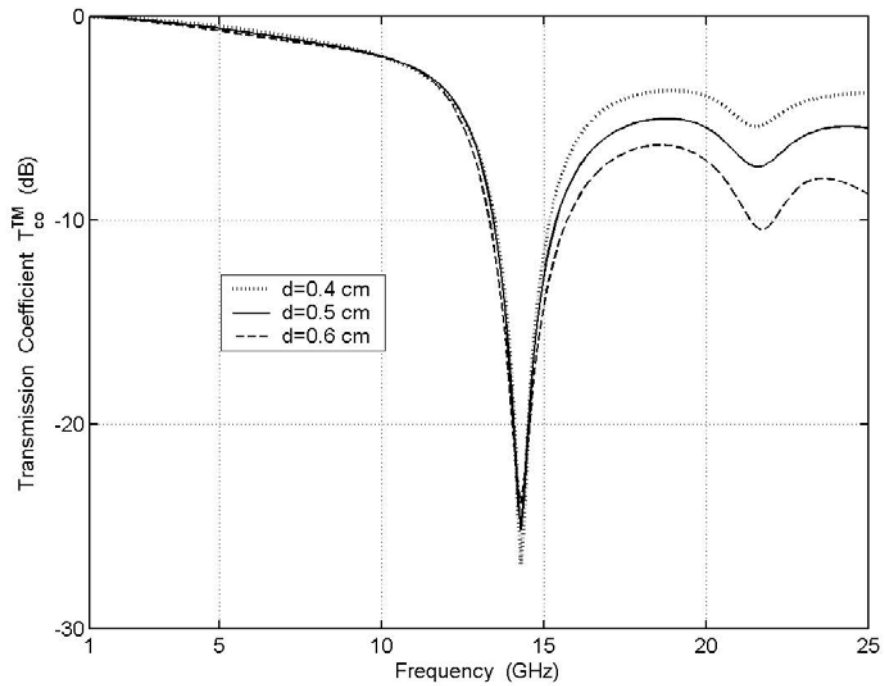
(c)

Figure 2.17 Reflection and transmission coefficients of one–turn square spiral FSS on a chiral slab at different slab thicknesses; TM incidence, ϕ=0°, ξ=0.001 S, d=0.5 cm, ε_r=1.6, w=0.016 cm, h_1=0.16cm, h_n=n*h_1 cm, n=2,3,4., d_1=d_2=0.73 cm, (*a*) Reflection Coefficient R_{co}^{TM}, (b) Transmission Coefficient T_{cr}^{TE}, (c) Transmission Coefficient T_{co}^{TM}
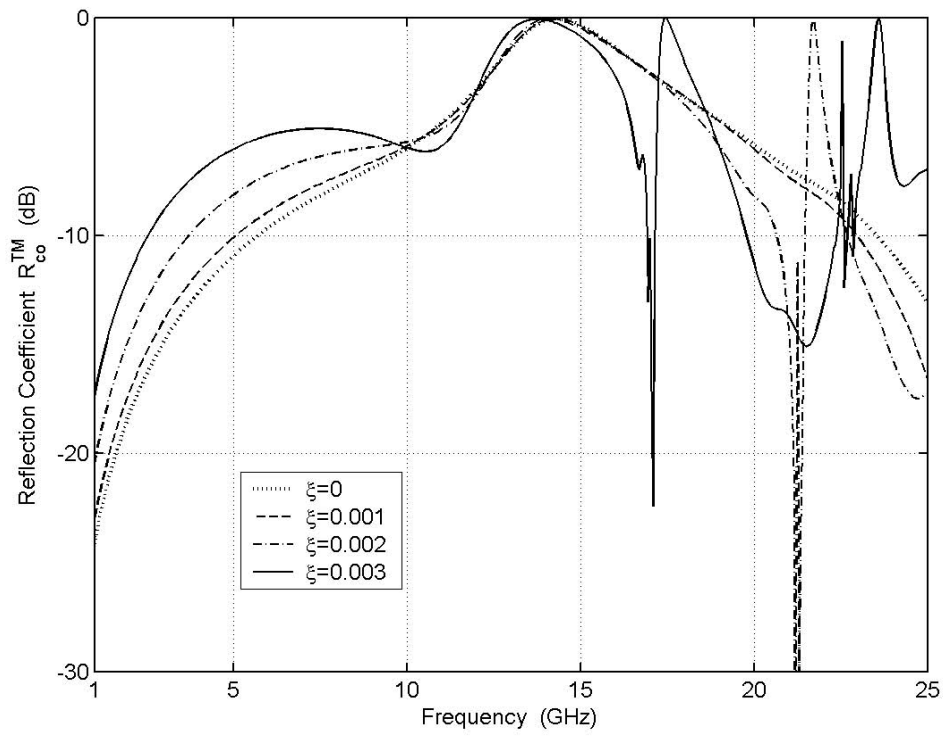
77

(*a*)

(b)

(c)

Figure 2.18 Reflection and transmission coefficients of one–turn square spiral FSS on a chiral slab at different incident angles; TM incidence, $\phi=0°$, $\xi=0.001$ S, $d=0.5$ cm, $\varepsilon_r=1.6$, $w=0.016$ cm, $h_1=0.16$ cm, $h_n=n^*h_1$ cm, n=2,3,4., $d_1=d_2=0.73$ cm, (a) Reflection Coefficient R_{co}^{TM}, (b) Transmission Coefficient T_{cr}^{TE}, (c) Transmission Coefficient T_{co}^{TM}
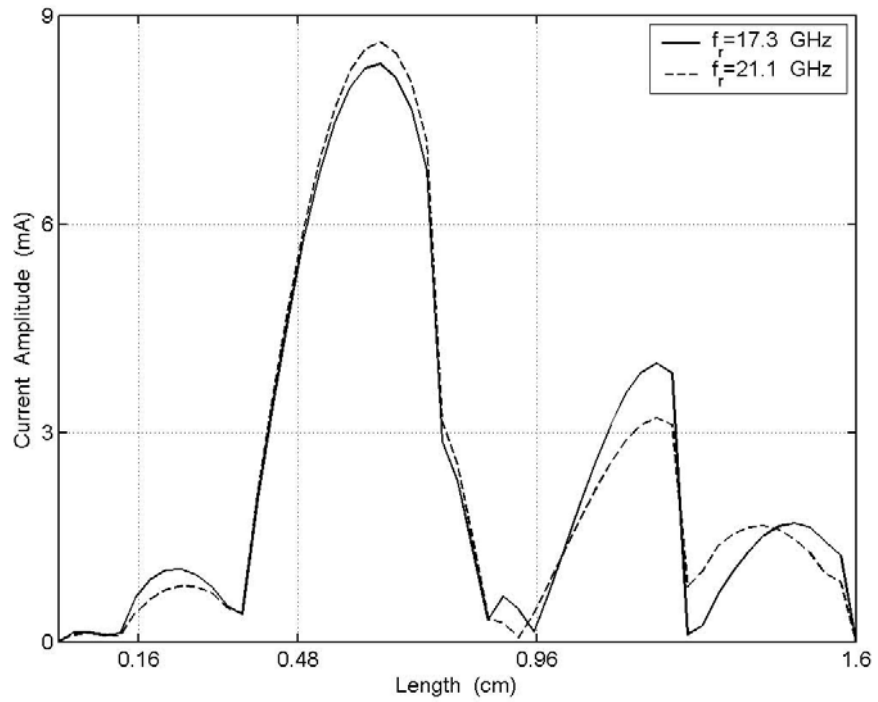
Figure 2.19 Current amplitude versus length at resonant frequencies of one–turn square spiral FSS on a chiral slab for TE incidence: $\theta=\phi=0°$, $\xi=0.003$ S, $d=0.5$ cm, $\varepsilon_r=1.6$, $w=0.016$ cm, $h_1=0.16$ cm, $h_n=n*h_1$ cm, n=2,3,4. $d_1=d_2=0.7$ cm
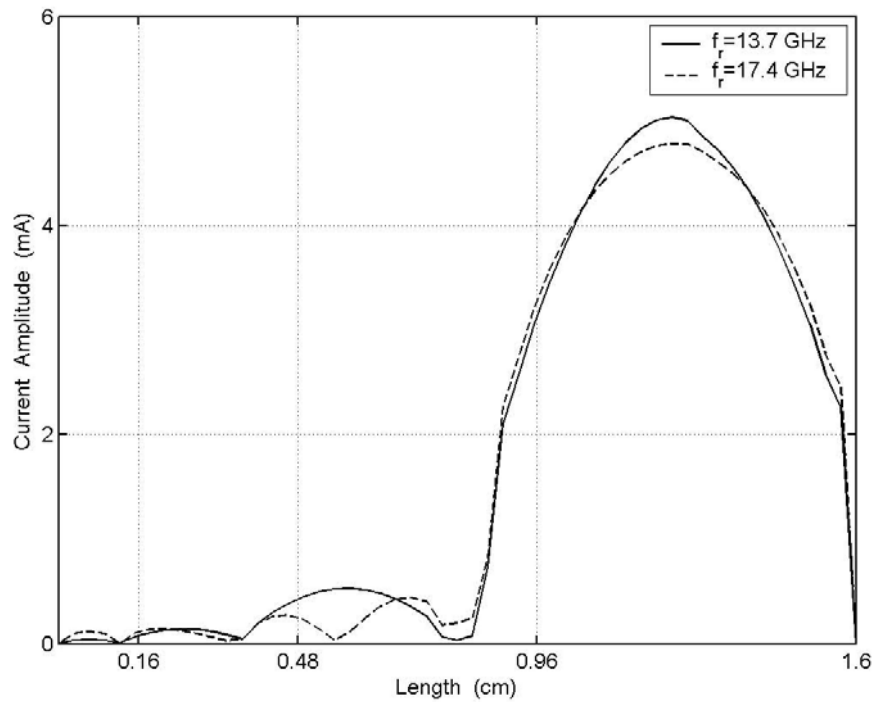
Figure 2.20 Current amplitude versus length at resonant frequencies of one–turn square spiral FSS on a chiral slab for TM incidence: $\theta=\phi=0°$, $\xi=0.003$ S, $d=0.5$ cm, $\varepsilon_r=1.6$, $w=0.016$ cm, $h_1=0.16$ cm, $h_n=n*h_1$ cm, n=2,3,4. $d_1=d_2=0.73$ cm

80

2.2.4 Numerical Results of Two–Turn Square Spiral FSS on a Chiral Slab

The numerical results of FSS comprised of periodic arrays of two–turn square spiral shaped conductors in the case of TE and TM incident waves are presented from Figure 2.21 to 2.28. The co– and cross–polarized reflection and transmission coefficients are plotted with respect to frequency for different values of chirality admittance, slab thickness and incident angle. The length of the first segment is $h_1=0.1$ cm. The lengths of the other segments can be found from the relation $h_n=n*h_1$ for $n=2,3,\ldots,8$. The width of the two–turn square spiral was chosen as $h_1/10$. The inter–element spacings are 0.83 cm. The periodic cells are arranged in square dimension. The overall length of the spiral is 3.6 cm. The number of basis functions required to estimate the unknown current coefficients is taken as 56. The number of Floquet modes used in the computations is 961. This number is obtained by inclusion of more Floquet modes until there is little change in the results.

Figure 2.21 shows the effect of chirality admittance variations at normal incidence of TE wave. In Figure 2.21a, it is seen that, two resonant frequencies exist for different values of ξ. In the region of frequency from 1 to 12 GHz, the magnitude of R_{co}^{TE} increases for increasing values of ξ. No variation was observed in the reflection curves in the 11.5–13.5 GHz. There is a small shift in the first resonant frequency, which happens at around 15.5 GHz. The bandwidth of second resonance is wider than the first one for $\xi=0$ and $\xi=0.001$ values. For $\xi=0.0018$ the magnitude of T_{cr}^{TM} is seen to be unity at three different frequencies as shown in Figure 2.21b. There is no polarization conversion (anti–resonance) for other chirality admittances and the magnitude of R_{co}^{TE} is very low at the anti–resonant frequency. In the frequency region of 1–15 GHz, the magnitude of T_{co}^{TE} decreases for increasing values of ξ, as illustrated in Figure 2.21c. The magnitude of R_{cr}^{TM} is very low in the frequency region of 1–13 GHz and it varies between –10 to –60 dB in the 15–25 GHz as can be depicted in Figure 2.21d.

81

Figure 2.22 illustrates the slab thickness variations at normal incidence. Two resonant frequencies are seen for three different slab thicknesses, as shown in Figure 2.22a. The resonant frequencies are not affected from the variation of slab thickness. An anti–resonance is seen at about 20 GHz for increasing value of slab thickness, as given in Figure 2.22b. In Figure 2.22c, there is a small decrease in the magnitude of T_{co}^{TE} up to about 16.5 GHz.

The reflection and transmission coefficients of two–turn square spiral FSS for oblique incidence variations are shown in Figure 2.23. There is a small shift in resonant frequency which happens at around 16.5 GHz as illustrated in Figure 2.23a. There is a gradual increase in magnitude of R_{co}^{TE} at oblique incidence variations up to resonant frequency. However, for an angle of 45°, the second resonant frequency disappears. No anti–resonance is observed for oblique incidence as shown in Figure 2.23b. As illustrated in Figure 2.23c, there is a small decrease in the magnitude of T_{co}^{TE} in the frequency range of 1–15 GHz and multiple peaks occur at higher frequencies.

(*a*)

(b)

83
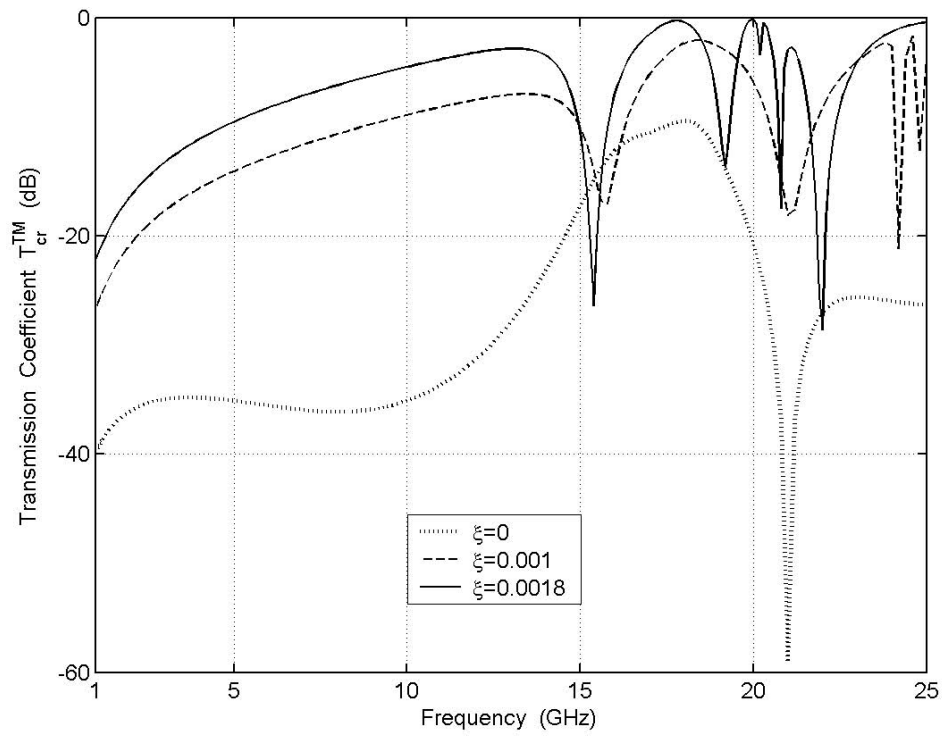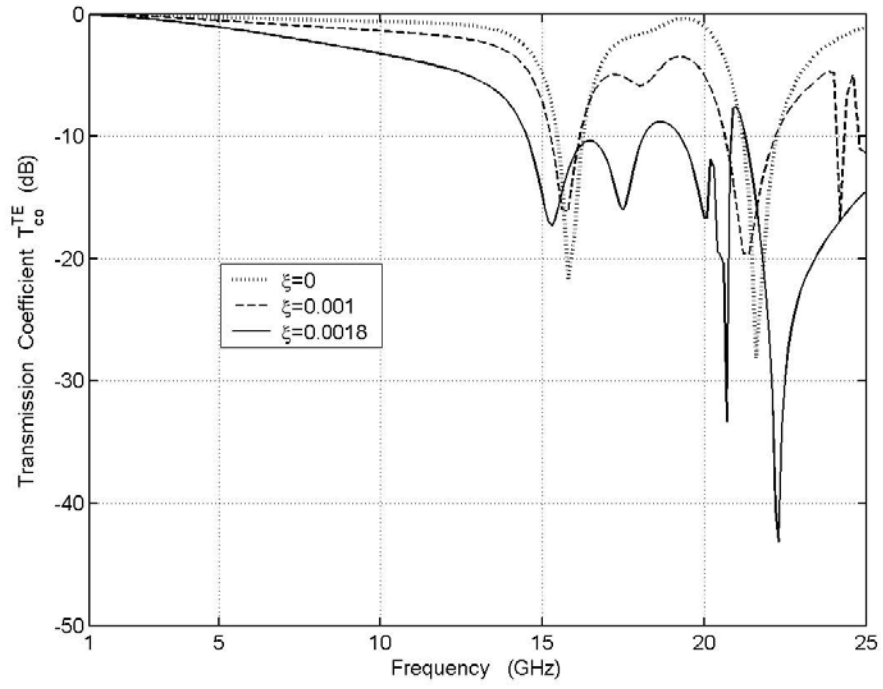
(c)

(d)

Figure 2.21 Reflection and transmission coefficients of two–turn square spiral FSS on a chiral slab at different chirality admittances; TE incidence, $\theta=\phi=0°$, d=0.5 cm, ε_r=1.6, w=0.01 cm, h_1=0.1 cm, h_n=n*h_1 cm, n=2,3,…,8., d_1=d_2=0.83 cm, (*a*) Reflection Coefficient R_{co}^{TE}, (b) Transmission Coefficient T_{cr}^{TM}, (c) Transmission Coefficient T_{co}^{TE}, (d) Reflection Coefficient R_{cr}^{TM}
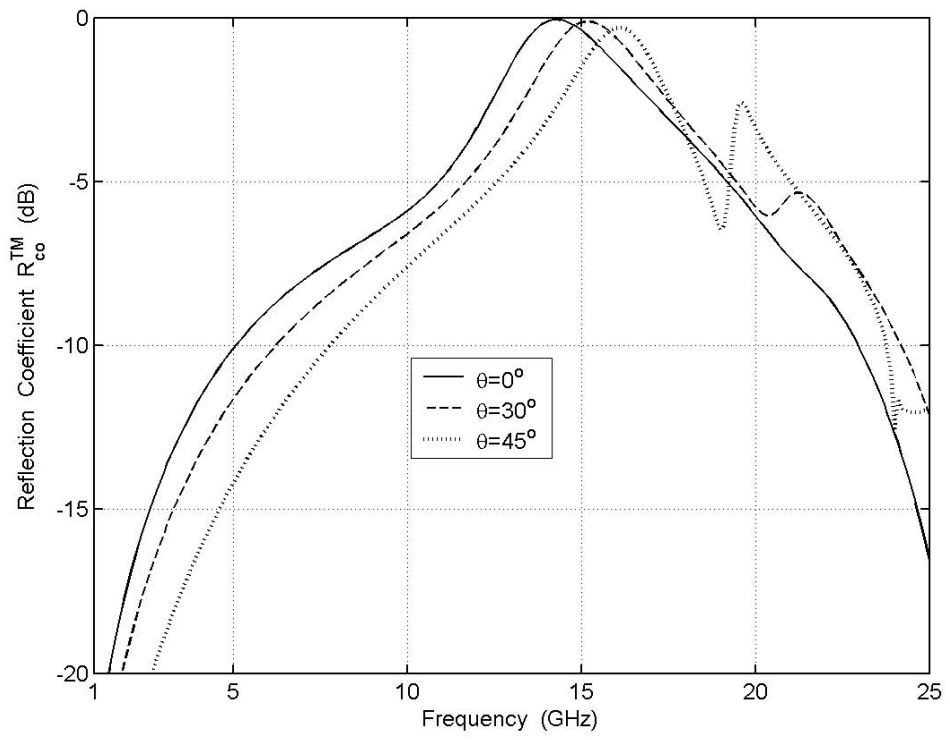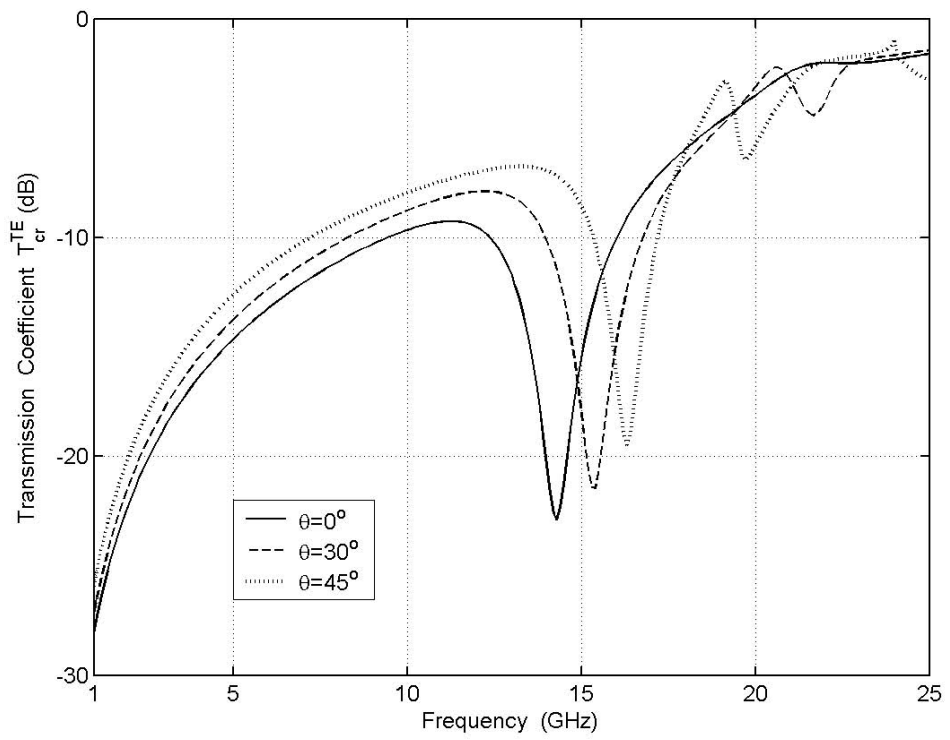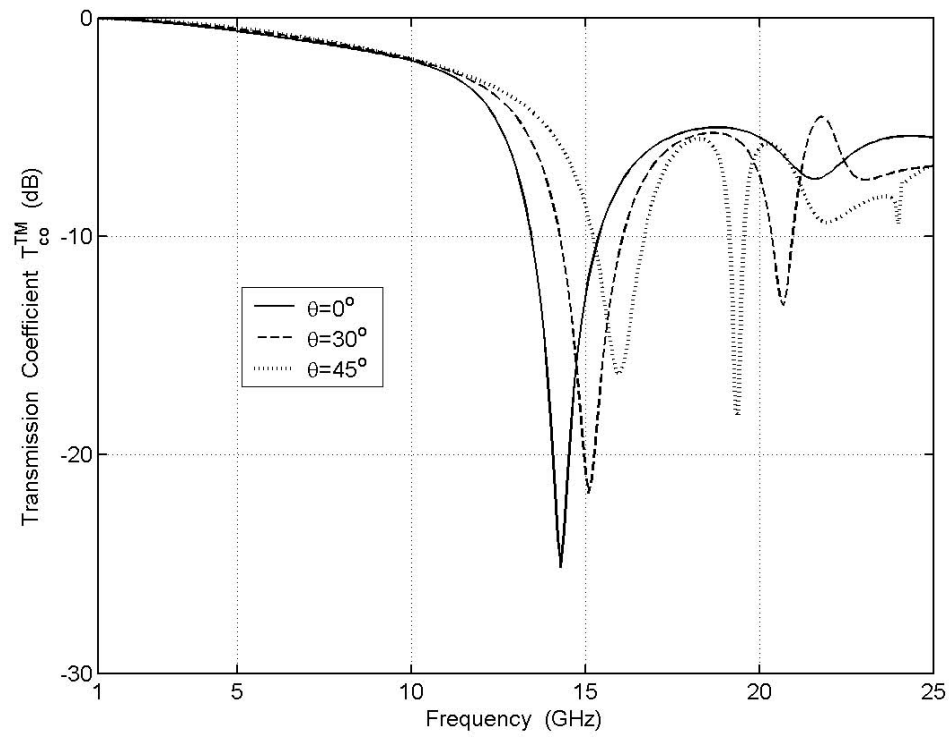
84

(*a*)

(b)

(c)

Figure 2.22 Reflection and transmission coefficients of two–turn square spiral FSS on a chiral slab at different slab thicknesses; TE incidence, $\theta=\phi=0°$, $\xi=0.001$ S, $\varepsilon_r=1.2$, $w=0.01$ cm, $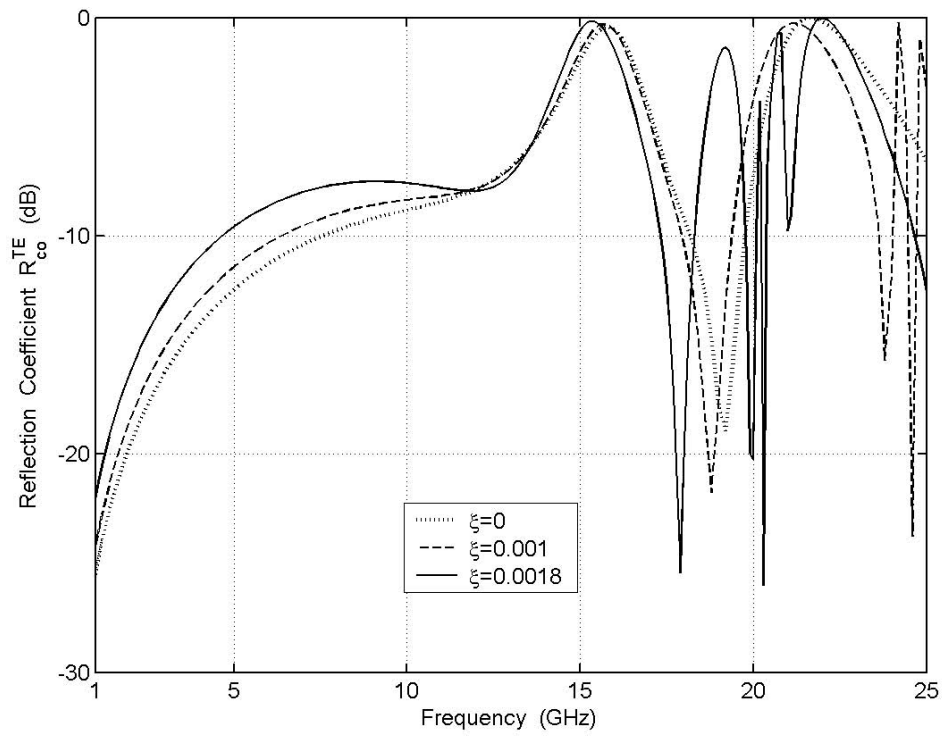h_1=0.1$ cm, $h_n=n*h_1$ cm, n=2,3,...,8., $d_1=d_2=0.83$ cm, (*a*) Reflection Coefficient R_{co}^{TE}, (b) Transmission Coefficient T_{cr}^{TM}, (c) Transmission Coefficient T_{co}^{TE}

(*a*)

(b)

(c)

Figure 2.23 Reflection and transmission coefficients of two–turn square spiral FSS on a chiral slab at different incident angles; TE incidence, $\phi=0°$, $\xi=0.001$ S, $d=0.5$ cm, $\varepsilon_r=1.2$, $w=0.01$ cm, $h_1=0.1$ cm, $h_n=n*h_1$ cm, n=2,3,…,8., $d_1=d_2=0.83$ cm, (*a*) Reflection Coefficient R_{co}^{TE}, (b) Transmission Coefficient T_{cr}^{TM}, (c) Transmission Coefficient T_{co}^{TE}

87

Figure 2.24 illustrates the effect of chirality admittance variations at normal incidence of TM wave. The resonance at about 3 GHz is not affected from the variation of chirality admittance, as shown in Figure 2.24a. The second peak increases in magnitude and shifts to lower frequency as ξ increases. The second resonance happens at 17.8 GHz and is narrower than the first one, for ξ=0.0018. In Figure 2.24b, the T_{cr}^{TE} has null at resonant frequency. Anti–resonances appear for ξ=0.0018 value of chirality admittance in the frequency regions of 15–25 GHz. The magnitude of T_{co}^{TM} is not changed in S–band frequency region, as depicted in Figure 2.24c. It also decreases in the frequency region of 6–17 GHz for an increasing value of ξ. The magnitude of R_{cr}^{TE} is the same with R_{cr}^{TM} which is plotted in Figure 2.21d.

The magnitude of reflection and transmission coefficients versus frequency is plotted for different values of slab thickness, as shown in Figure 2.25. Two resonant peaks, which are not affected by the variation of slab thickness, appear as given in Figure 2.25a. In Figure 2.25b, the magnitude of T_{cr}^{TE} increases corresponding to increasing value of slab thickness, except the region around resonant frequency. The T_{cr}^{TE} has nulls at resonant frequencies. The T_{co}^{TM} has also nulls at resonant frequencies as shown in Figure 2.25c. In S–band frequency region, there is no change in magnitude. The magnitude of T_{co}^{TM} reduces in the frequency regions of 7–19 GHz and 21–25 GHz, as the slab thickness increases.

The oblique incidence variations are plotted in Figure 2.26 for different values of incident angles. In Figure 2.26a, there is a slight shift at the first resonant frequency. The magnitude of second resonance reduces and disappears for obliquely incident angles. As can be seen in Figure 2.26b, there is no anti–resonance for ξ=0.001. As shown in Figure 2.26c, there is a slight change up to 10 GHz and no variation was observed in the frequency range of 10–17 GHz.

The normalized current amplitude versus stretched out length for two–turn square spiral is depicted in Figures 2.27 and 2.28 for TE and TM plane waves, respectively. Although the amplitude of currents is different at resonant frequencies, their amplitudes are normalized to unity. The vertical grids illustrate the corners of the two–turn square spiral. The current has one greater peak at one parallel segment with respect to other segments for both type of polarization. At f_r=2.8 GHz most of the current is induced at the longest segment for TM case as shown in Figure 2.28.
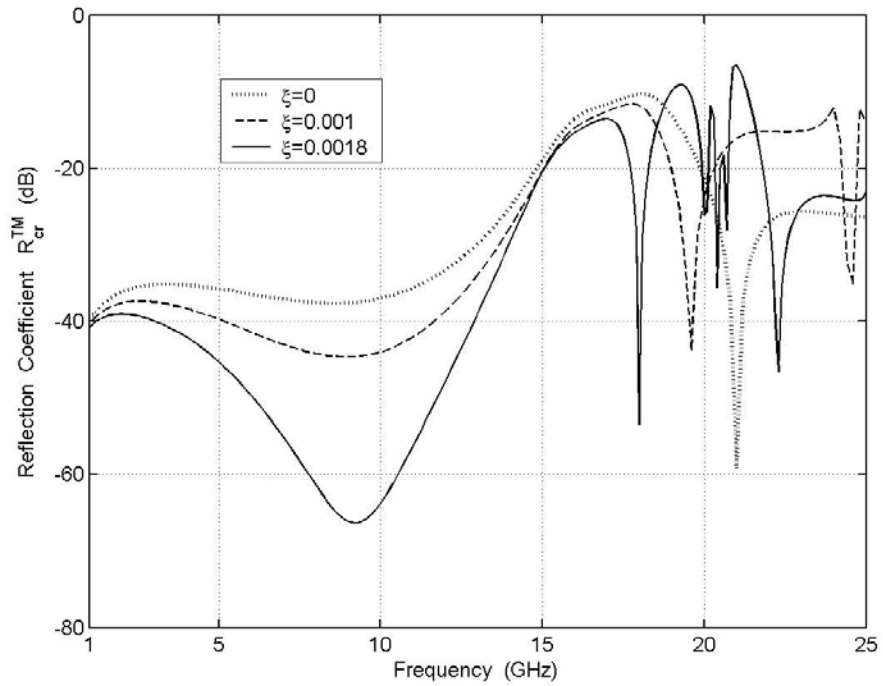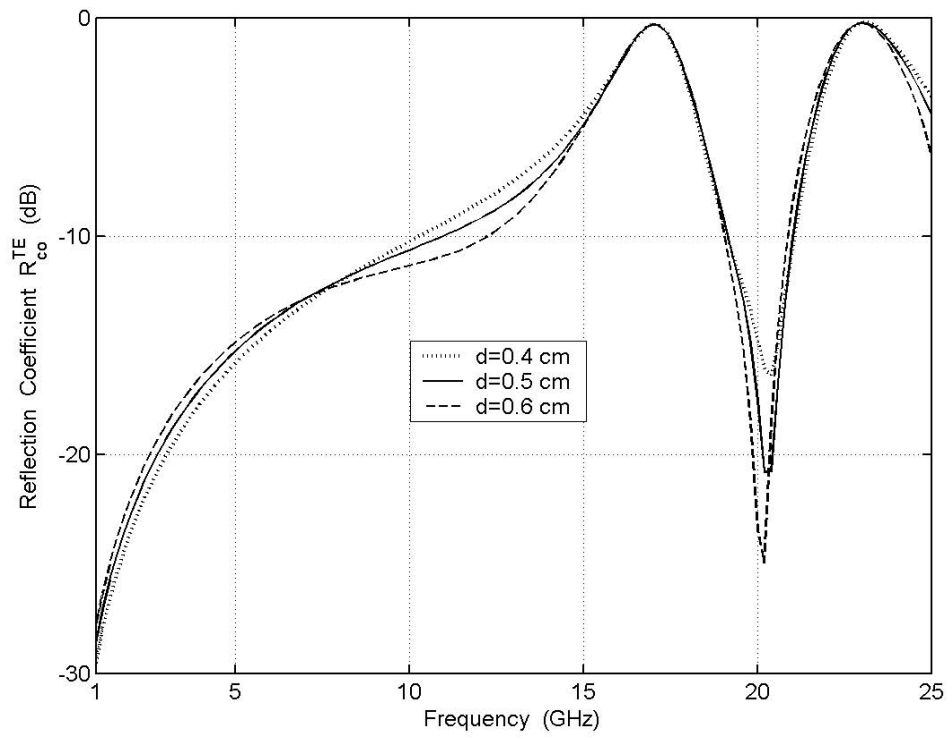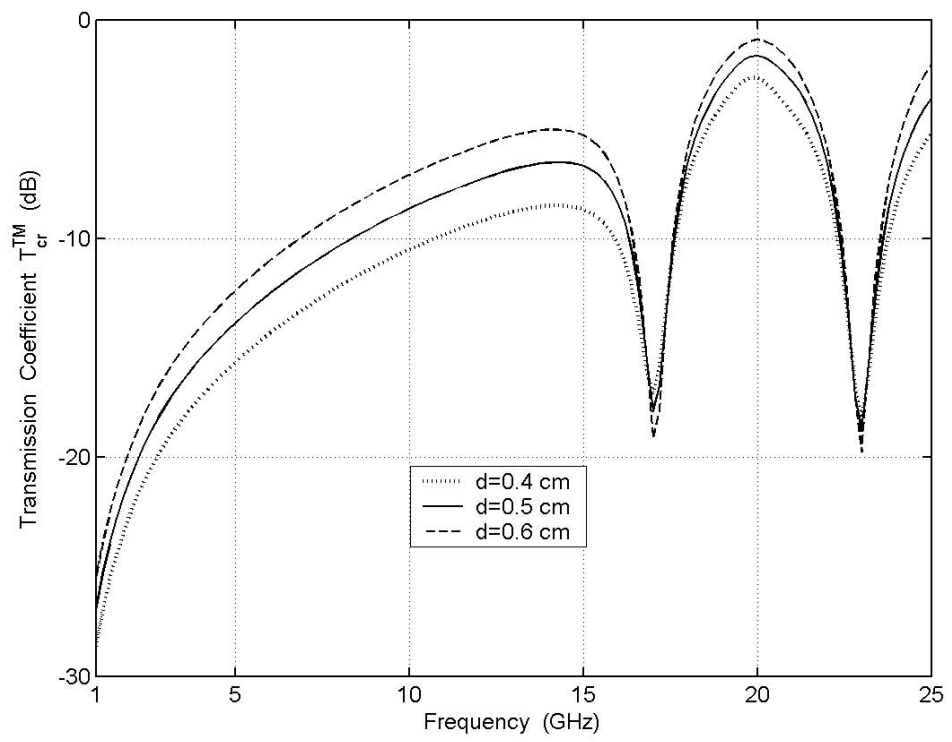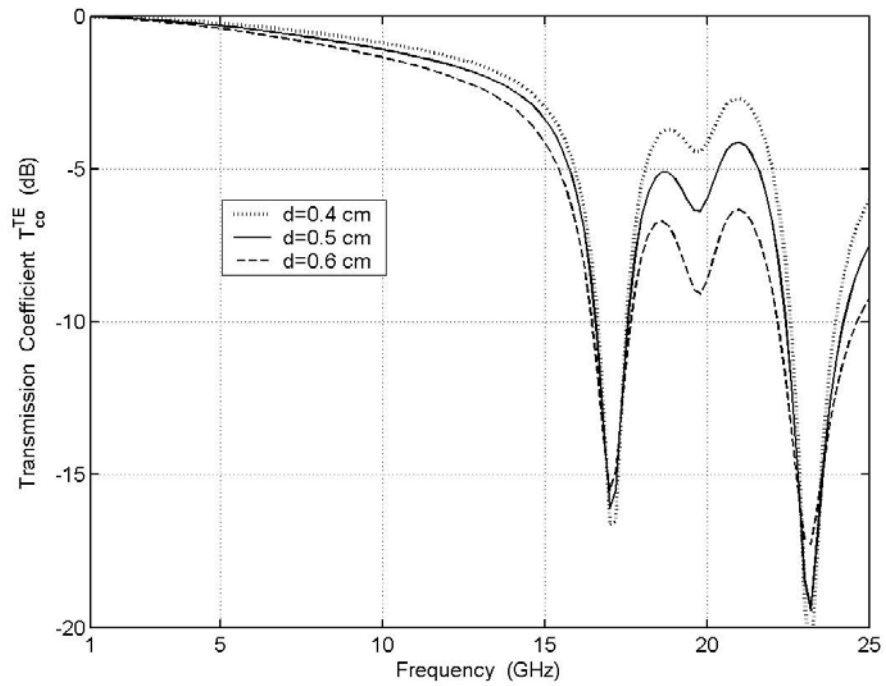
(*a*)
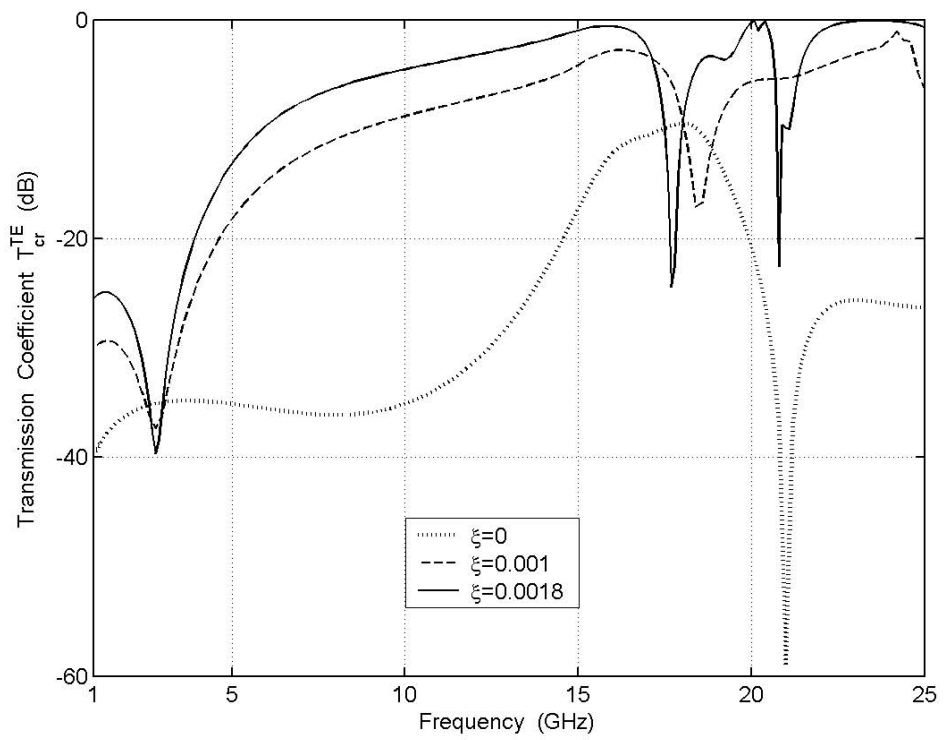
(b)
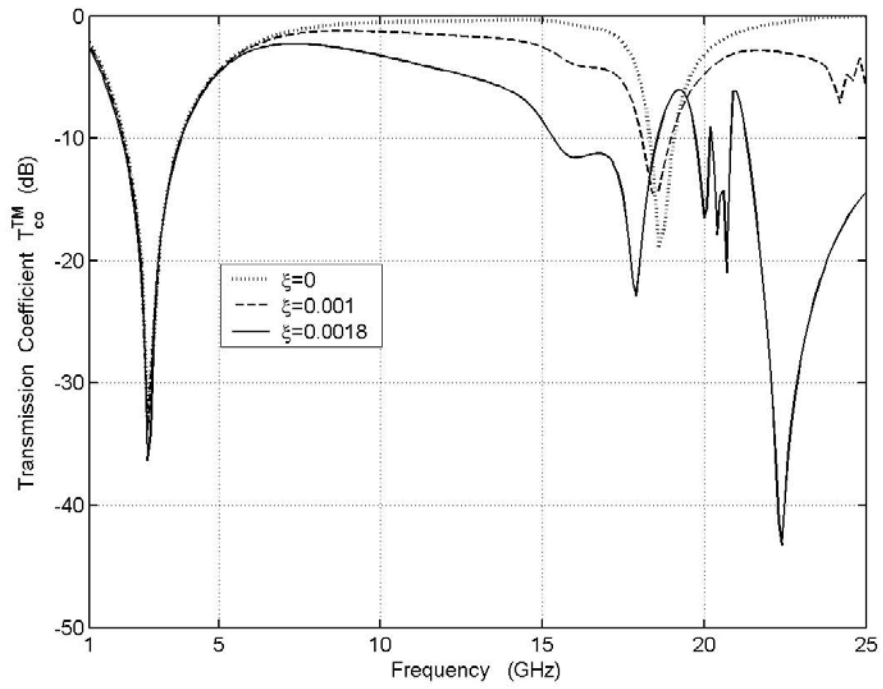
(c)
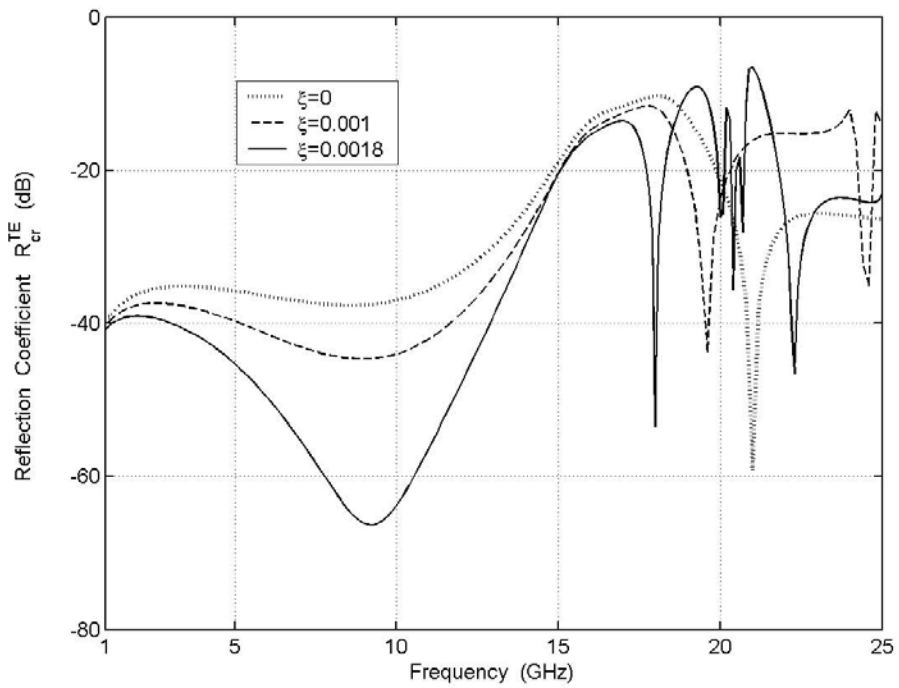
(d)

Figure 2.24 Reflection and transmission coefficients of two–turn square spiral FSS on a chiral slab at different chirality admittances; TM incidence, $\theta=\phi=0°$, d=0.5 cm, ε_r=1.6, w=0.01 cm, h_1=0.1 cm, h_n=n*h_1 cm, n=2,3,…,8., d_1=d_2=0.83 cm, (*a*) Reflection Coefficient R_{co}^{TM} , (b) Transmission Coefficient T_{cr}^{TE} , (c) Transmission Coefficient T_{co}^{TM} , (d) Reflection Coefficient R_{cr}^{TE}
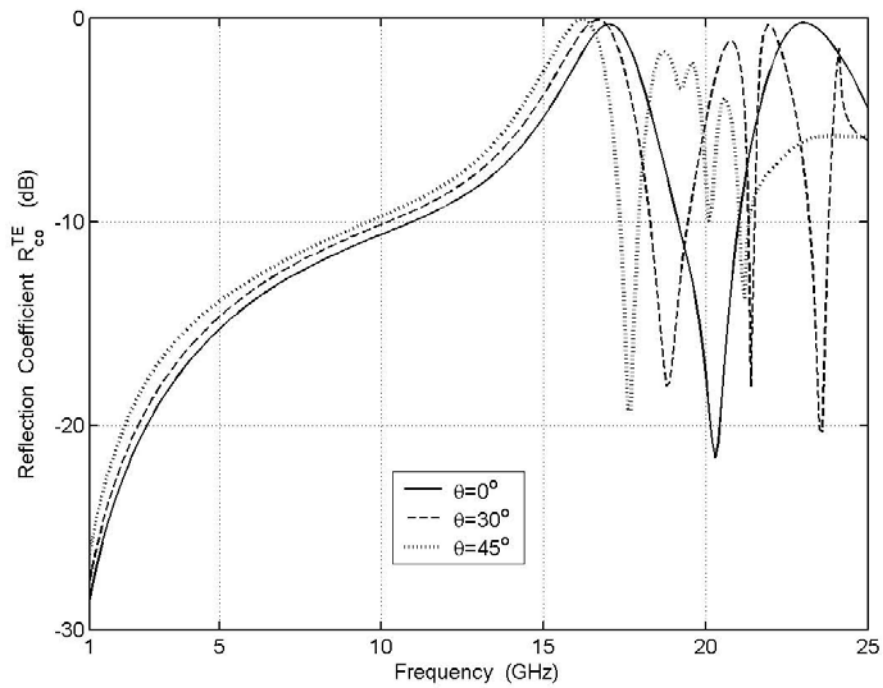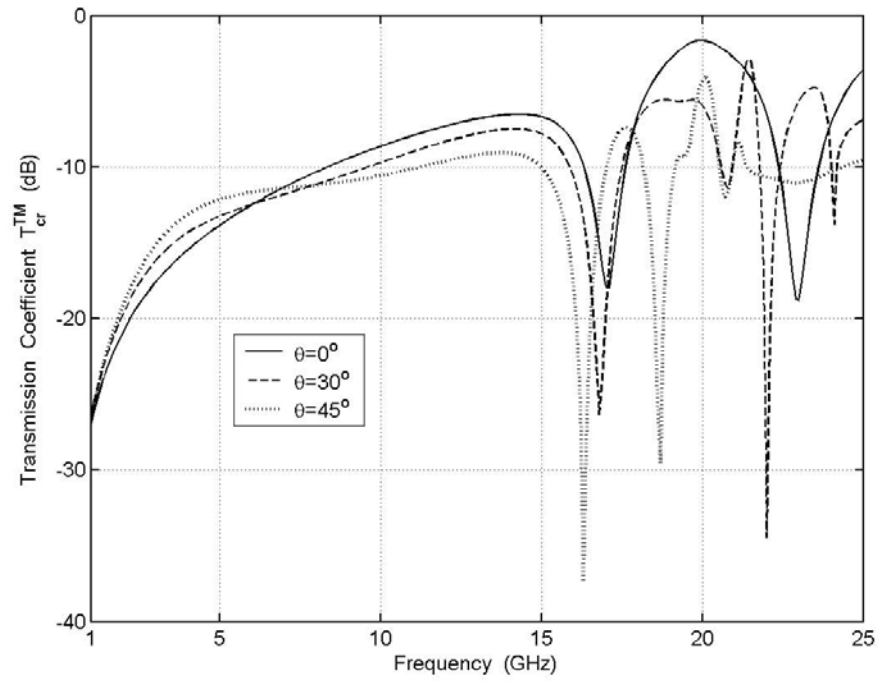
90
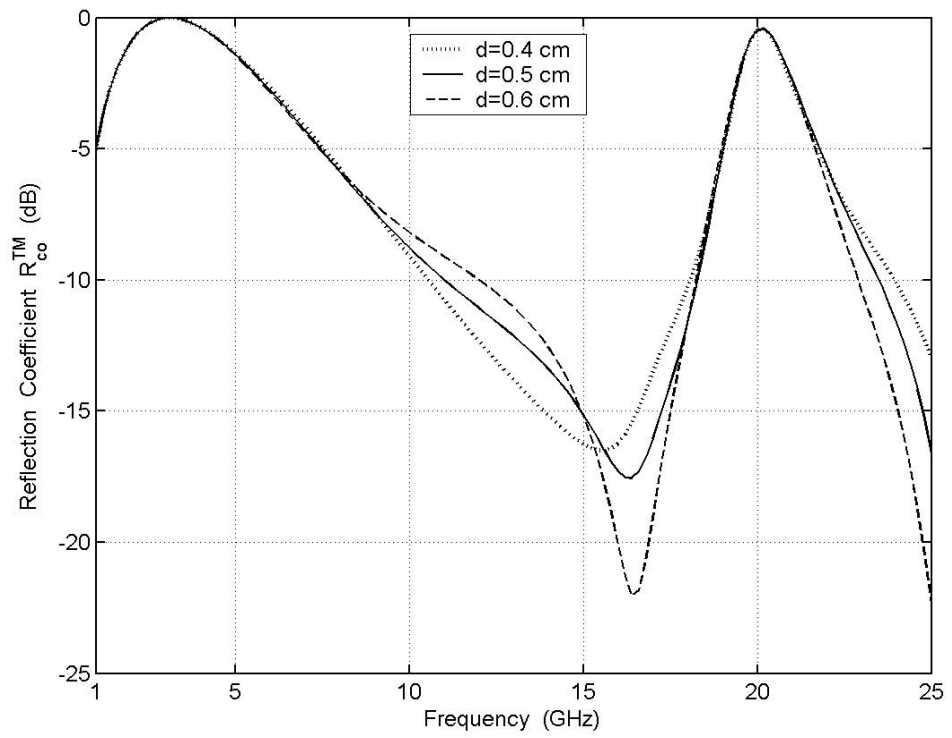
(*a*)
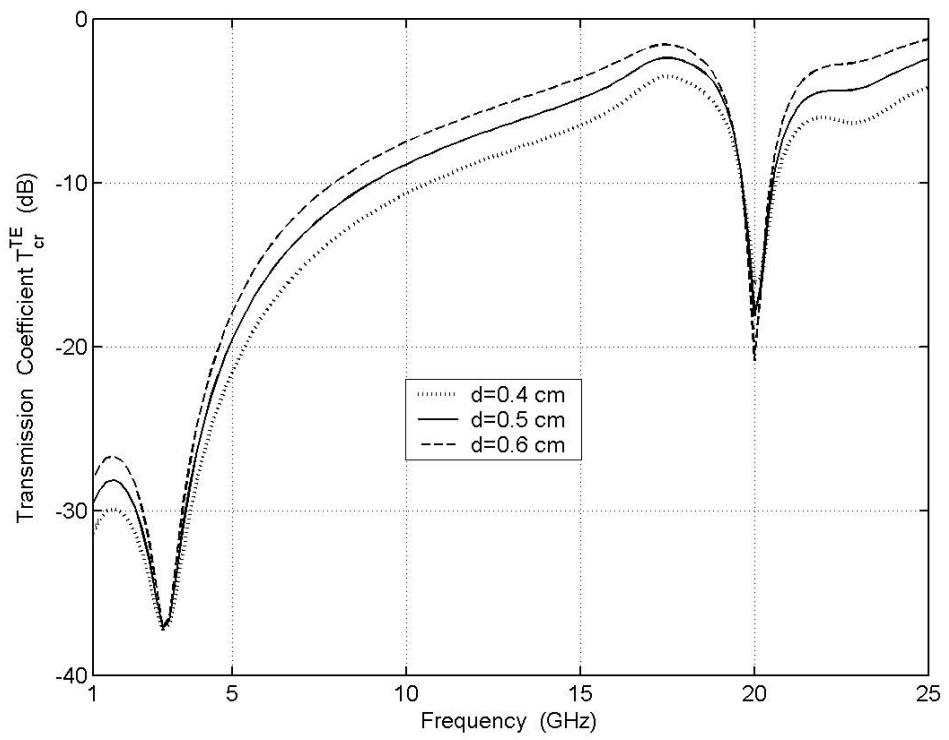
(b)
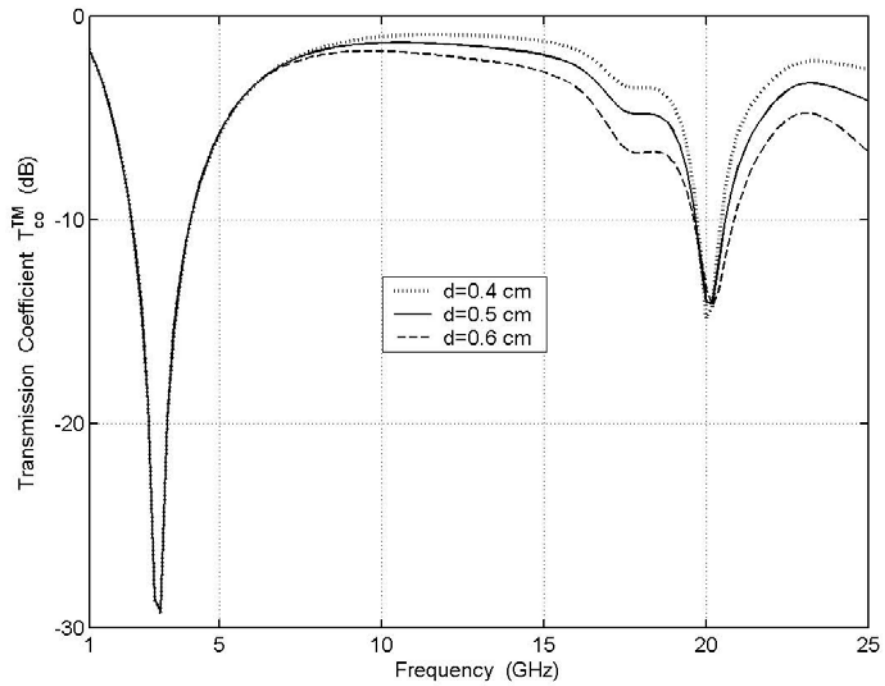
(c)

Figure 2.25 Reflection and transmission coefficients of two–turn square spiral FSS on a chiral slab at different slab thciknesses; TM incidence, $\theta=\phi=0°$, $\xi=0.001$ S, $\varepsilon_r=1.2$, $w=0.01$ cm, $h_1=0.1$ cm, $h_n=n*h_1$ cm, n=2,3,…,8., $d_1=d_2=0.83$ cm, (a) Reflection Coefficient R_{co}^{TM}, (b) Transmission Coefficient T_{cr}^{TE}, (c) Transmission Coefficient T_{co}^{TM}
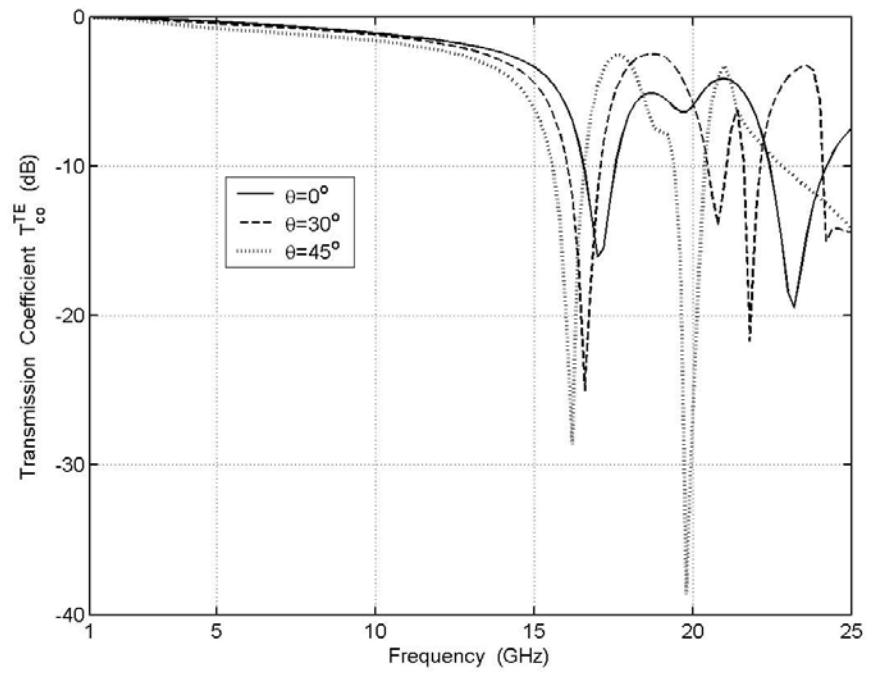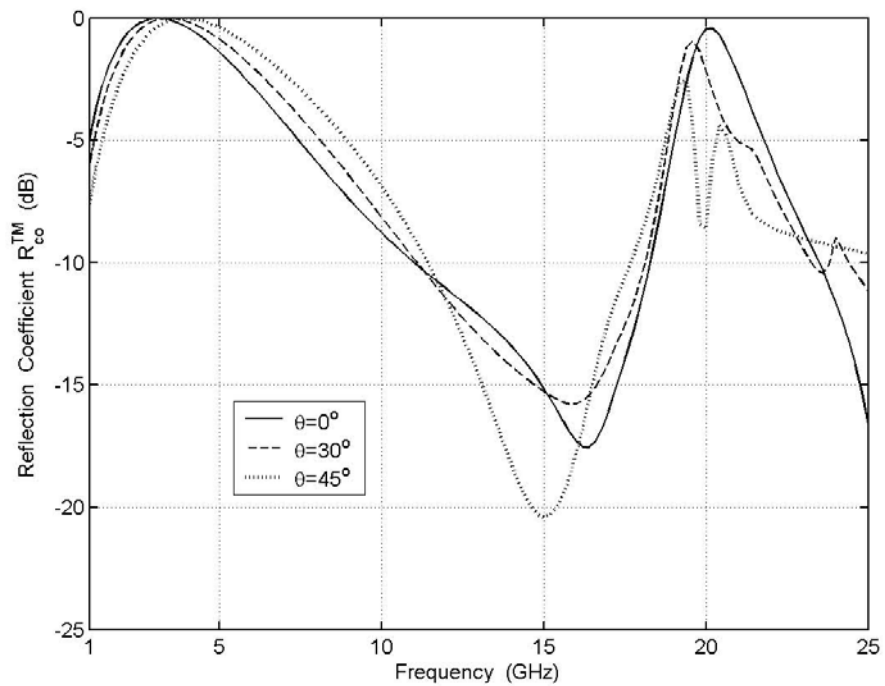

(a)
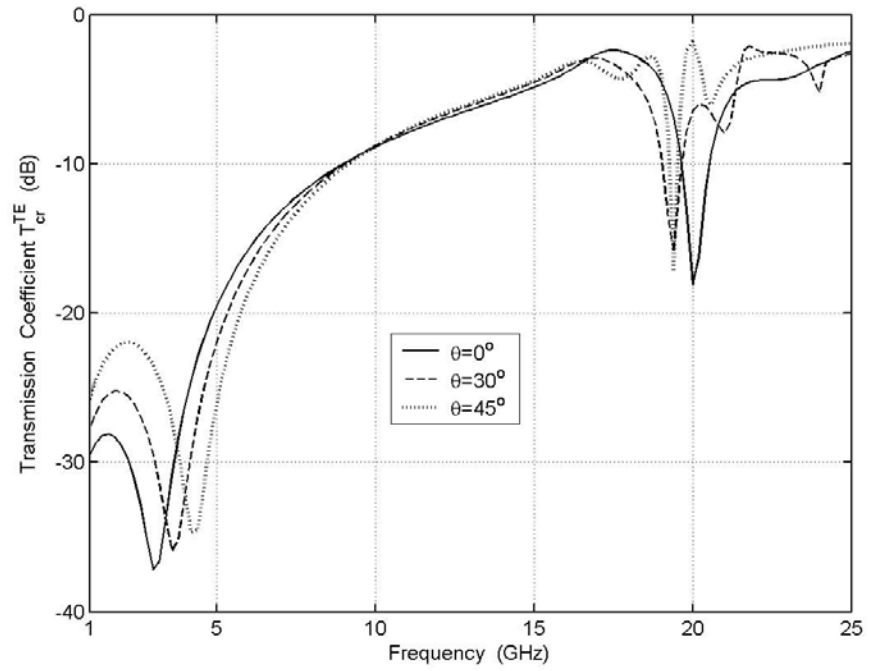
(b)
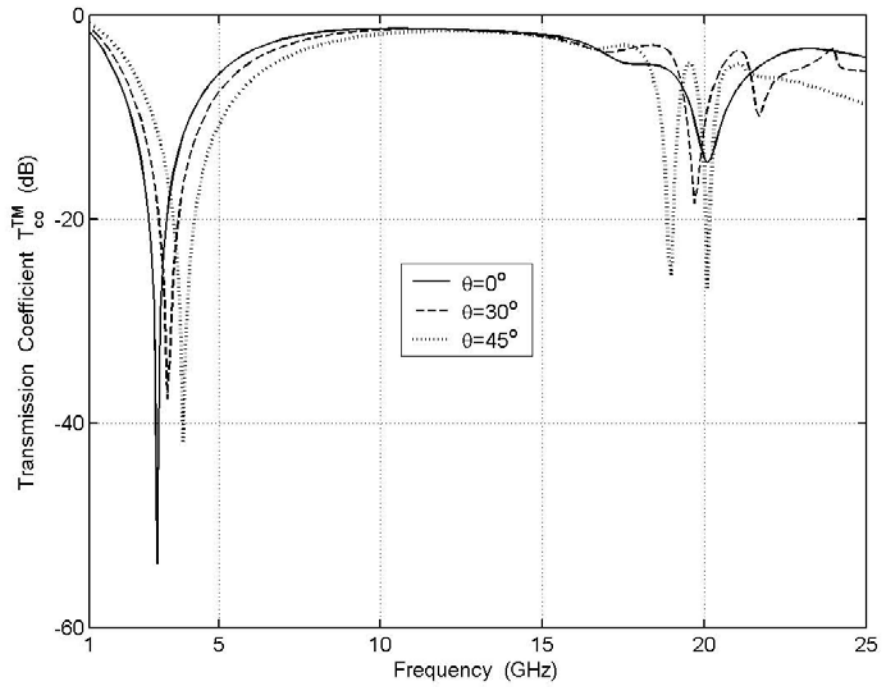
(c)

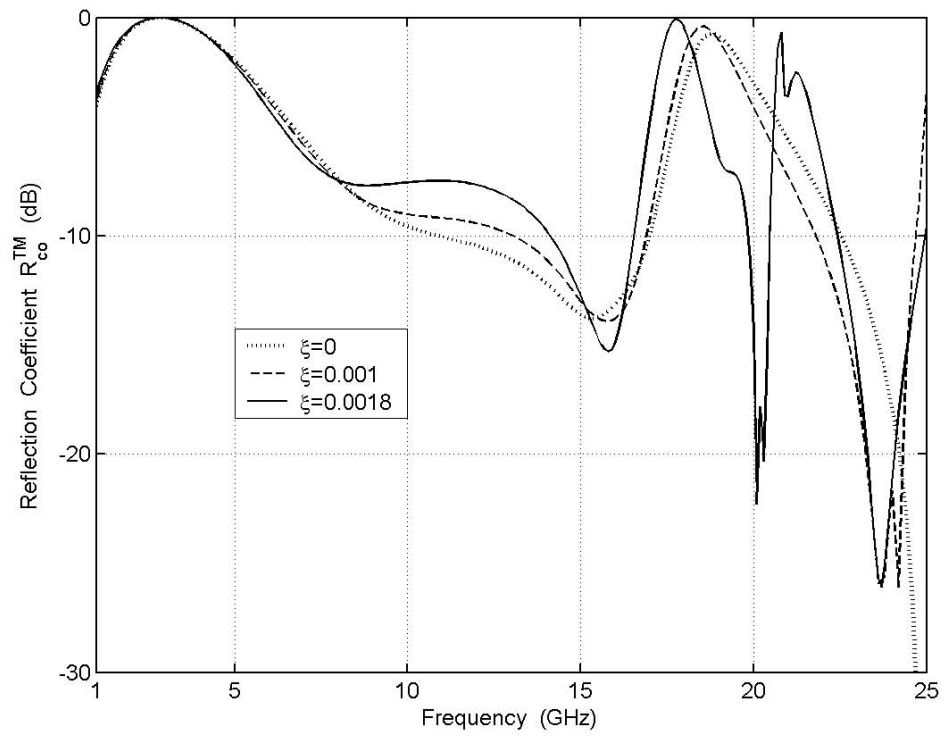**Figure 2.26** Reflection and transmission coefficients of two–turn square spiral FSS on a chiral slab at different incident angles; TM incidence, $\phi=0°$, $\xi=0.001$ S, $d=0.5$ cm, $\varepsilon_r=1.2$, $w=0.01$ cm, $h_1=0.1$ cm, $h_n=n*h_1$ cm, n=2,3,…,8., $d_1=d_2=0.83$ cm, (*a*) Reflection Coefficient R_{co}^{TM} , (b) Transmission Coefficient T_{cr}^{TE} , (c) Transmission Coefficient T_{co}^{TM}

93
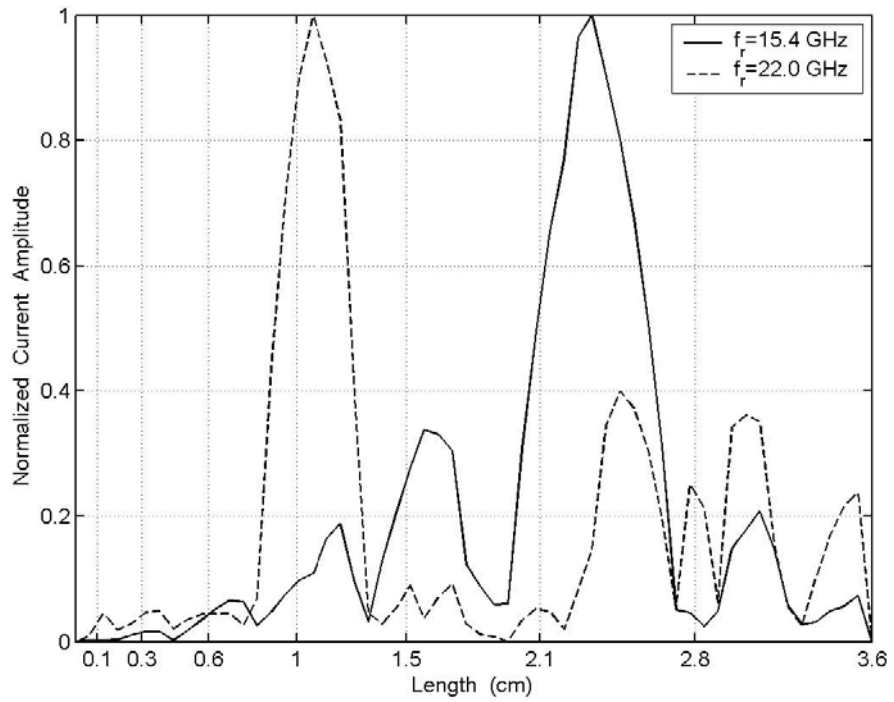
Figure 2.27 Normalized current amplitude versus length at resonant frequencies of two–turn square spiral FSS on a chiral slab for TE incidence: $\theta=\phi=0°$, $\xi=0.0018$ S, $d=0.5$ cm, $\varepsilon_r=1.6$, $w=0.01$ cm, $h_1=0.1$ cm, $h_n=n*h_1$ cm, n=2,3,…,8., $d_1=d_2=0.83$ cm
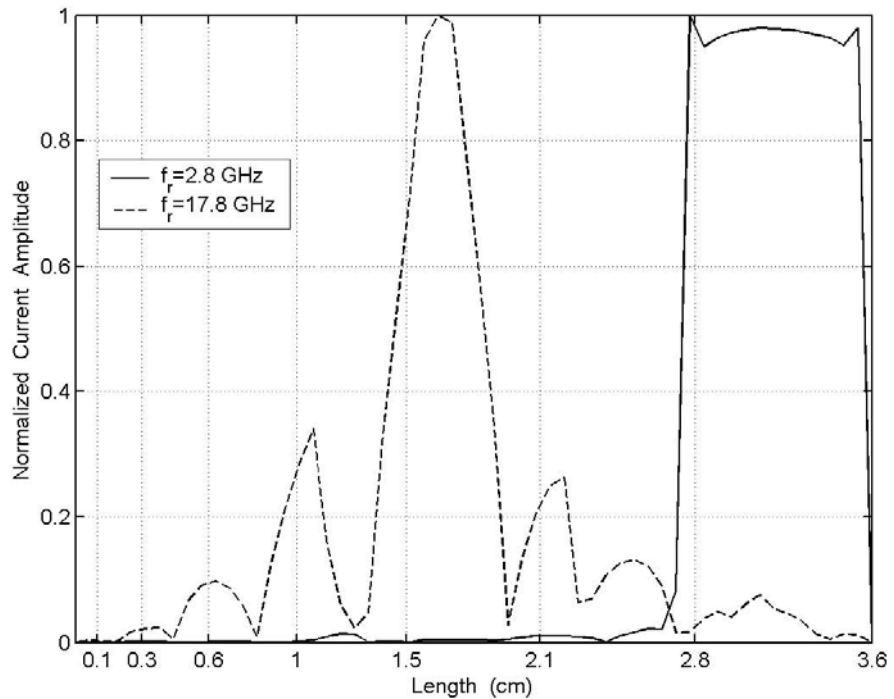
Figure 2.28 Normalized current amplitude versus length at resonant frequencies of two–turn square spiral FSS on a chiral slab for TM incidence: $\theta=\phi=0°$, $\xi=0.0018$ S, $d=0.5$ cm, $\varepsilon_r=1.6$, $w=0.01$ cm, $h_1=0.1$ cm, $h_n=n*h_1$ cm, n=2,3,…,8., $d_1=d_2=0.83$ cm

94

CHAPTER 3

CONCLUSIONS

This study addresses new FSS element geometries that have not been studied earlier. The major contribution of this study is in fact the presented scattering properties of L–shaped, one– and two–turn square spiral FSS elements backed by planar dielectric and chiral slabs.

3.1   Conclusion to Dielectric Backed FSSs

The scattering of electromagnetic waves from freestanding and dielectric backed FSS elements are investigated in Chapter 1. An improved subsectional current approximation model of PWS basis is proposed to expand the induced current. The MM is employed to determine the reflection and transmission coefficients. The Floquet modes are included until there is little difference in results. The amplitude of element currents along the stretched out wire is plotted for dielectric backed FSSs. The reflection coefficient versus frequency is plotted for different values of incident angle, dielectric slab thickness and dielectric constant.

The correctness of the algorithm is ensured by comparing the numerical results with the experimental results in the literature for an FSS composed of strips and proved to be as good. Another check for the correctness is that at normal incidence, the amplitude of reflection and transmission coefficients with reference to L–shaped FSS elements are the same without regard to TE or TM wave excitations. The correctness of one– and two–turn square spirals is also satisfied by interchanging the x– and y–axis. It has been observed that each FSS element has different resonant frequencies and bandwidths, showing band stop filter characteristics at different frequency regions. These structures are used as passive electromagnetic filters. FSS with two–turn square spiral array can be used as a band–stop filter at different

frequencies for TE and TM wave incidences. There is an anti–resonance at S–band and Ku–band frequency regions. Therefore, it can be made into both reflecting and transparent FSS.

A good FSS element should be small in terms of wavelength. A quality element should have a stable resonant frequency with angle of incidence. The primary reason for this is simply that the inter–element spacings are kept as small as possible. Further increase in inter–element spacing will lead to early onset of grating modes which always push the fundamental resonance downward with angle of incidence. Grating modes only depend on inter–element spacings and the incident angle. Keeping d_1 and d_2 small delays the onset of grating modes. For three FSS elements, the only propagating mode is the zero order Floquet mode.

It is seen that adding dielectric to periodic surfaces lowers the resonant frequency. The bandwidth varies more with polarization. There is no need to increase the number of turns since addition of more turns will increase the inter–element spacing, which will cause the resonant frequency to reduce and trigger the onset of grating modes.

3.2   Conclusion to Chiral Backed FSSs

In Chapter 2, the co– and cross–polarized reflection and transmission coefficients, which are strongly sensitive to the frequency of the incident wave, are plotted with respect to frequency for the variation of medium parameters and oblique incident angle. Numerical results illustrate that the chirality admittance of the slab causes a significant polarization rotation of the scattered fields. At low chirality admittances, there is no polarization conversion. Multiple resonances are seen for high value of chirality admittance because one wave number becomes very high at that value. The number of resonances depends on the slab thickness, dielectric constant and chirality admittance of the chiral medium. Anti–resonances which correspond to mode conversion are seen in cross–polarized transmission, for both types of polarization. This feature can have potential applications in design of novel devices such as TE $\leftrightarrow$ TM converters and polarization filters. In the reflection

characteristics of FSS elements on chiral slab, the resonances are separated with a deep minimum which shows a very good isolation between the resonances. As we increase the chirality admittance, the transmitted power is virtually switched from one mode to the other. This feature can be intuitively explained by recalling that the polarization of the electric field transverse components "rotates" as the wave traverses the chiral slab.

The resonant frequency is not affected from the variation of slab thickness for one– and two–turn square spiral elements. There is a small shift at resonant frequency for L–shaped FSS. The resonant frequency shifts for the variation of dielectric constant. At normal incidence, chiral medium behaves differently with TE and TM waves. For one–turn square spiral FSS, as the oblique angle increases multiple resonances appear in TE case but there is only one resonant frequency in TM case. The first resonant frequency shifts to the lower end and the second resonance disappears at oblique angle of incidence for two–turn square spiral but no anti–resonance is observed.

3.3 Recommendations for Future Work

The present study permits the reflection and transmission coefficients of L–shaped, one– and two–turn square spiral FSSs backed by planar dielectric and chiral slabs. The study is open to further developments. Future works can be the following:

- A spiral with circular turns can be investigated on planar dielectric and chiral slabs;
- FSS with spiral square–shaped turn elements can be cascaded to form multilayer dielectric or chiral slab;
- FSS with spiral circular turn elements can be cascaded to form multilayer dielectric or chiral slab;
- A spiral with circular turns or spiral with square–shaped turns of finite extent on dielectric or chiral slabs can be investigated;
- The square spiral element on chiral slab can be used as a FSS element [3];
- Bifilar or quadfilar spiral FSS elements can be investigated on a dielectric or chiral slab.

APPENDIX

The full expressions for the coefficients of TM wave on a chiral slab appearing in equation (2.18)–(2.25) are given below.

$$D_{1pq} = \left\{ (Y^l_{2pq}(1+r1_{pq}) + Y^r_{2pq}r3_{pq})b1_{pq} + (Y^r_{2pq}(1+r4_{pq}) + Y^l_{2pq}r2_{pq})b3_{pq} \right\} / Y_c$$

$$D_{2pq} = \left\{ (Y^l_{2pq}(1+r1_{pq}) + Y^r_{2pq}r3_{pq})b2_{pq} + (Y^r_{2pq}(1+r4_{pq}) + Y^l_{2pq}r2_{pq})b4_{pq} \right\} / Y_c$$

$$D_{3pq} = b1_{pq}(1-r1_{pq}+r3_{pq}) + b3_{pq}(-1-r2_{pq}+r4_{pq})$$

$$D_{4pq} = b2_{pq}(1-r1_{pq}+r3_{pq}) + b4_{pq}(-1-r2_{pq}+r4_{pq})$$

$$K_{1pq} = \frac{Y_c}{Y_{100}} \left[b1_{00}(cl - r1_{00}\,clj - r3_{00}\,crj) + b3_{00}(cr - r2_{00}\,clj - r4_{00}\,crj) \right]$$

$$K_{2pq} = \frac{Y_c}{Y_{100}} \left[b2_{00}(cl - r1_{00}\,clj - r3_{00}\,crj) + b4_{00}(cr - r2_{00}\,clj - r4_{00}\,crj) \right]$$

$$K_{3pq} = b1_{00}(cl - r1_{00}\,clj + r3_{00}\,crj) + b3_{00}(-cr - r2_{00}\,clj + r4_{00}\,crj)$$

$$K_{4pq} = b2_{00}(cl - r1_{00}\,clj + r3_{00}\,crj) + b4_{00}(-cr - r2_{00}\,clj + r4_{00}\,crj)$$

$$\begin{bmatrix} b_1 & b_2 \\ b_3 & b_4 \end{bmatrix} = \begin{bmatrix} b_{11} & b_{12} \\ b_{21} & -b_{22} \end{bmatrix}^{-1} \begin{bmatrix} -Y_c \\ j \end{bmatrix} \quad cl = e^{-j\gamma^l_{00}d} \quad cr = e^{-j\gamma^r_{00}d} \quad clj = cl^* \quad crj = cr^*$$

$$b_{11} = (Y_{1pq} + Y^l_{1pq})Y^l_{2pq} + (Y_{1pq} - Y^l_{1pq})Y^l_{2pq}r1_{pq} + (Y_{1pq} - Y^r_{1pq})Y^r_{2pq}r3_{pq}$$

$$b_{12} = (Y_{1pq} + Y^r_{1pq})Y^r_{2pq} + (Y_{1pq} - Y^l_{1pq})Y^l_{2pq}r2_{pq} + (Y_{1pq} - Y^r_{1pq})Y^r_{2pq}r4_{pq}$$

$$b_{21} = (Y_{2pq} + Y^l_{2pq}) - (Y_{2pq} - Y^l_{2pq})r1_{pq} + (Y_{2pq} - Y^r_{2pq})r3_{pq}$$

$$b_{22} = (Y_{2pq} + Y^r_{2pq}) + (Y_{2pq} - Y^l_{2pq})r2_{pq} - (Y_{2pq} - Y^r_{2pq})r4_{pq}$$

$$r1_{pq} = \left((Y_0^2 + Y_c^2)(Y^r_{2pq} - Y^l_{2pq}) + 2Y_c^2 Y_{2pq} - 2Y_{1pq}Y^l_{2pq}Y^r_{2pq} \right) e^{-j2\gamma^l_{pq}d} / \Delta_1$$

$$r2_{pq} = 2Y^r_{2pq}(Y_c^2 - Y_0^2)e^{-j(\gamma^l_{pq}+\gamma^r_{pq})d} / \Delta_1$$

$$r3_{pq} = 2ylte_{pq}(Y_c^2 - Y_0^2)e^{-j(\gamma^l_{pq}+\gamma^r_{pq})d} / \Delta_1$$

$$r4_{pq} = \left((Y_0^2 + Y_c^2)(Y^l_{2pq} - Y^r_{2pq}) + 2Y_c^2 Y_{2pq} - 2Y_{1pq}Y^l_{2pq}Y^r_{2pq} \right) e^{-j2\gamma^r_{pq}d} / \Delta_1$$

$$\Delta_1 = Y^l_{2pq}(Y_{1pq} + Y^l_{1pq})(Y_{2pq} + Y^r_{2pq}) + Y^r_{2pq}(Y_{2pq} + Y^l_{2pq})(Y_{1pq} + Y^r_{1pq})$$

$$Y_{1pq} = Y_o k_o / \gamma^o_{pq} \qquad Y_{2pq} = Y_o \gamma^o_{pq} / k_o \qquad Y^l_{1pq} = Y_c k_l / \gamma^l_{pq} \qquad Y^l_{2pq} = Y_c \gamma^l_{pq} / k_l$$

$$Y^r_{1pq} = Y_c k_r / \gamma^r_{pq} \qquad Y^r_{2pq} = Y_c \gamma^r_{pq} / k_r \qquad Y_c = \sqrt{\dfrac{\varepsilon}{\mu_o} + \xi^2}$$

The full expressions for the coefficients of TE wave on a chiral slab

$$C_{1pq} = t1_{pq}(-1 - s1_{pq} + s3_{pq}) + t3_{pq}(1 - s2_{pq} + s4_{pq})$$

$$C_{2pq} = t2_{pq}(-1 - s1_{pq} + s3_{pq}) + t4_{pq}(1 - s2_{pq} + s4_{pq})$$

$$C_{3pq} = \left\{ (Y^l_{2pq}(1 - s1_{pq}) - Y^r_{2pq}s3_{pq})t1_{pq} + (Y^r_{2pq}(1 - s4_{pq}) - Y^l_{2pq}s2_{pq})t3_{pq} \right\} / Y_c$$

$$C_{4pq} = \left\{ (Y^l_{2pq}(1 - s1_{pq}) - Y^r_{2pq}s3_{pq})t2_{pq} + (Y^r_{2pq}(1 - s4_{pq}) - Y^l_{2pq}s2_{pq})t4_{pq} \right\} / Y_c$$

$$P_{1pq} = t1_{00}(-cl - s1_{00}\,clj + s3_{00}\,crj) + t3_{00}(cr - s2_{00}\,clj + s4_{00}\,crj)$$

$$P_{2pq} = t2_{00}(-cl - s1_{00}\,clj + s3_{00}\,crj) + t4_{00}(cr - s2_{00}\,clj + s4_{00}\,crj)$$

$$P_{3pq} = \dfrac{Y_c}{Y_{100}}\left[t1_{00}(cl + s1_{00}\,clj + s3_{00}\,crj) + t3_{00}(cr + s2_{00}\,clj + s4_{00}\,crj) \right]$$

$$P_{4pq} = \dfrac{Y_c}{Y_{100}}\left[t2_{00}(cl + s1_{00}\,clj + s3_{00}\,crj) + t4_{00}(cr + s2_{00}\,clj + s4_{00}\,crj) \right]$$

$$\begin{bmatrix} t_2 & t_1 \\ t_4 & t_3 \end{bmatrix} = \begin{bmatrix} t_{11} & t_{12} \\ t_{21} & -t_{22} \end{bmatrix}^{-1} \begin{bmatrix} jY_c \\ 1 \end{bmatrix}$$

$$t_{11} = (Y_{100} + Y^l_{1pq})Y^l_{2pq} - (Y_{100} - Y^l_{1pq})Y^l_{2pq}s1_{pq} - (Y_{100} - Y^r_{1pq})Y^r_{2pq}s3_{pq}$$

$$t_{12} = (Y_{1pq} + Y^r_{1pq})Y^r_{2pq} - (Y_{1pq} - Y^l_{1pq})Y^l_{2pq}s2_{pq} - (Y_{1pq} - Y^r_{1pq})Y^r_{2pq}s4_{pq}$$

$$t_{21} = (Y_{2pq} + Y^l_{2pq}) + (Y_{2pq} - Y^l_{2pq})s1_{pq} - (Y_{2pq} - Y^r_{2pq})s3_{pq}$$

$$t_{22} = (Y_{2pq} + Y^r_{2pq}) - (Y_{2pq} - Y^l_{2pq})s2_{pq} + (Y_{2pq} - Y^r_{2pq})s4_{pq}$$

$$s1_{pq} = \left[(Y^2_0 + Y^2_c)(Y^r_{1pq} - Y^l_{1pq}) + 2Y^2_c Y_{1pq} - 2Y_{2pq}Y^l_{1pq}Y^r_{1pq} \right] e^{-j2\gamma^l_{pq}d} / \Delta_2$$

$$s2_{pq} = 2Y^l_{1pq}(Y^2_0 - Y^2_c)e^{-j(\gamma^l_{pq} + \gamma^r_{pq})d} / \Delta_2$$

$$s3_{pq} = 2Y^r_{1pq}(Y^2_0 - Y^2_c)e^{-j(\gamma^l_{pq} + \gamma^r_{pq})d} / \Delta_2$$

$$s4_{pq} = \left[-(Y^2_0 + Y^2_c)(Y^r_{1pq} - Y^l_{1pq}) + 2Y^2_c Y_{1pq} - 2Y_{2pq}Y^l_{1pq}Y^r_{1pq} \right] e^{-j2\gamma^r_{pq}d} / \Delta_2$$

$$\Delta_2 = Y^l_{1pq}(Y_{1pq} + Y^r_{1pq})(Y_{2pq} + Y^l_{2pq}) + Y^r_{1pq}(Y_{1pq} + Y^l_{1pq})(Y_{2pq} + Y^r_{2pq})$$

REFERENCES

[1] Mittra, R., Chan, C.H. and Cwik, T. (1988). Techniques for analyzing frequency selective surfaces– A review. *IEEE Proceedings*, **76,** 12, 1593–1615

[2] Vardaxoglu J. C. (1997). *Frequency Selective Surfaces: Analysis and Design*, Wiley, New York.

[3] Munk B. A. (2000). *Frequency Selective Surfaces: Theory and Design*, Wiley, New York.

[4] Ott, R.H., Kouyoumjian, R.G. and Peters, J. (1967). Scattering by a two dimensional periodic array of narrow plates. *Raido Sci.,* **2**, 1347–1349

[5] Agrawal, V.D. and Imbriale, W.A. (1979). Design of a Dichroic Cassegrain Subreflector. *IEEE Trans. AP*, **27**,4, 466–473

[6] Vardaxoglu, J.C. and Parker E.A. (1983). Performance of two tripole arrays as frequency selective surfaces. *Electron Lett.*, 19, 709–710

[7] Bornemann J. (1983). Double square frequency selective surfaces and their equivalent circuit. *Electron Lett.*, 19, 675–677

[8] Tsao, C.H. and Mittra, R. (1984). Spectral domain analysis of frequency selective surfaces comprised of periodic arrays of cross dipoles and Jerusalem crosses. *IEEE Trans. AP*, **32**, 478–486

[9] Jin, J.M. and Volakis, J.I. (1990). Electromagnetic scattering by a perfectly conducting patch array on a dielectric slab. *IEEE Trans. AP*, 38, 4, 556–563

[10] Schimert, T.R., Brouns, A.J., Chan, C.H. and Mittra, R. (1991) Investigation of millimeter–wave scattering from frequency selective surfaces. *IEEE Trans. Microw. Theory & Tech.* 39, 315–322

[11] Zimmerman M.L., Lee, S.W. and G. Fujikawa G. (1992). Analysis of Reflector antenna system including Frequency selective surfaces. *IEEE Trans. AP*, **40**, 10, 1264–1266

[12] Rahmat–Samii, Y. and Tulintseff, A.N. (1993). Diffraction analysis of Frequency selective reflector antennas. *IEEE Trans. AP*, **41**, 4, 476–487

[13] Campos A.L.P.S., Assuncao A.G. and Mendonca, L.M. (2002). Scattering by FSS on anisotropic substrate for TE and TM excitation. *IEEE Trans. Microw. Theory&Tech.* **50**, 1, 72–76

[14] Huang, J., Wu, T.K. and Lee, S.W. (1994). Tri–band frequency selective surface with circular ring elements. *IEEE Trans. AP*, **42**, 166–175

[15] Lee, Y.L.R., Chauraya, A., Lockyer, D.S., and Vardaxoglu, J.C. (2000). Dipole and tripole metallodielectric photonic bandgap (MPBG) structures for microwave filter and antenna applications. *IEE Proc. –Optoelectron*. **147**, 395–400

[16] Bassiri, S., Papas C.H. and Engheta, N. (1988). Electromagnetic Wave Propagation through a Dielectric–Chiral Interface and through a Chiral Slab. *J. Opt. Soc. Am. A*, **5**, 1450–1459

[17] Engheta, N. and Jaggard, D.L. (1988). Electromagnetic Chirality and its Applications. *IEEE AP–S Newslett.,* **30**, 6–12

[18] Lindell, I.V., Sihvola, A.H., Tretyakov, S.A. and Viitanen, A.J. (1994). Electromagnetic Waves in Chiral and Bi–Isotropic Media, Norwood, MA.

[19] Viitanen, A.J. and Lindell, I.V. (1998). Chiral slab polarization transformer for aperture antennas. *IEEE Trans. AP*, **46**, 9, 1395–1397

[20] Jaggard, D.L. and Engheta, N. (1989). Chirosorb as an invisible medium. *Electron. Lett.* **25**, 3, 173–174

[21] Lakhtakia, A., Varadan, V.K. and Varadan, V.V. (1989) Scattering by periodic achiral–chiral interface. *J. Opt. Soc. Am. A.* **11**, 1675–1681

[22] Pelet, P. and Engheta, N. (1990). The theory of chirowaveguides. *IEEE Trans. AP*, **38**, 1, 90–98

[23] Cory, H. and Rosenhouse, I. (1992). Some applications of multi–layered chiral structures. *Electron. Lett.* **28**, 1051–1053

[24] Pozar, D.M. (1992). Microstrip antennas and arrays on chiral substrates. *IEEE Trans. AP*, **40**, 1260–1263

[25] Saadoun M.M.I. and Engheta N. (1994). Theoretical study of variation of propagation constant in a cylindrical waveguide due to chirality: Chiro–phase shifting. *IEEE Trans. Microw. Theory & Tech.* **42**, 9, 1690–1694

[26] Allam, A.M.M. (2000). Chiral absorbing material. *17th National Radio Science Conference,* Minufiya University, Egypt.

[27] Koca, A. O. (1997) *Analysis of Frequency Selective Surfaces on Chiral Slab* PhD Dissertation, University of Gaziantep.

[28] Nakano, H. (1987*). Helical and Spiral Antennas: A Numerical Approach*, Wiley, New York.

[29] Harrington, R.F. (1968). *Field Computation by Moment Methods*, MacMillan, New York.

[30] Delihacıoglu, K. and Uckun S. (2003). Power reflection and transmission coefficients for Meander–Line polarizers with a chiral slab, *ETRI Journal*, **25**, 1, 41–48

[31] Amitay, N., Galindo, V. and Wu, C.P. (1972). *Theory and analysis of phased array antennas.* Wiley–Intersection, New York.

[32] Montgomery, J.P. (1975). Scattering by an infinite periodic array of thin conductors on a dielectric sheet. *IEEE Trans. AP,* **23**, 70–75

[33] Webb, K.J., Grounds, P.W. and Mittra, R. (1990). Convergence in the spectral domain formulation of waveguide and scattering problems. *IEEE Trans. AP*, **38**, 869–877

[34] Delihacıoğlu, K., Uçkun, S., Ege, T. (2005). L–şeklindeki ve bir döngü biçimindeki frekans seçici yüzeylerin saçılma karakteristikleri, *Elektrik–Elektronik–Bilgisayar Mühendisliği 11.Ulusal Kongresi*, YTU, İstanbul

[35] Delihacıoğlu, K., Uçkun, S., Ege, T. (2007). Scattering characteristics of FSS comprised of L–shaped and one–turn helix shaped conductors for TE and TM excitation. *Electrical Engineering*, **89**, 3, 177–181

[36] Delihacıoğlu, K., Uçkun, S., Ege, T. (2006). FSS comprised of one– and two–turn square spiral shaped conductors on dielectric slab, *IVth International Workshop on Electromagnetic Wave Scattering*, September 18–22, Gebze, Turkiye

[37] Delihacıoğlu, K., Uçkun, S., Ege, T. (2007). Frequency selective surfaces comprised of periodic arrays of two–turn square spiral shaped conductors. *Int. J. Electron. Commun.(AEÜ)*, **61**, 3, 182–185

[38] Delihacıoğlu, K., Uçkun, S., Ege, T. (2006). Bakışımsız levhaya periyodik konulan şerit ve L–şeklindeki metal iletkenlerin Frekans Seçici yüzey olarak kullanımı, *URSI–TÜRKİYE 2006* Hacettepe Üniversitesi, Ankara

[39] Delihacıoğlu, K., Uçkun, S., Ege, T. (2006). L–shaped frequency selective surfaces as conducting elements on chiral slab. *Journal of Optoelectronics and Advanced Materials*, **8**, 4, 1398–1401

CURRICULUM VITAE

PERSONAL INFORMATION

Surname, Name: DELİHACIOĞLU Kemal

Nationality: Turkish (TC)

Date and Place of Birth: 01 January 1971 , Kilis

Marital Status: Married

Phone: +90 342 3172131

Fax: +90 537 411 05 47

email: kemal@gantep.edu.tr

EDUCATION

Degree	Institution	Year of Graduation
MS	University of Gaziantep	1998
BS	University of Gaziantep	1995
High School	Kilis High School	1989

WORK EXPERIENCE

Year	Place	Enrollment
1995– Present	University of Gaziantep	Research Assistant

FOREIGN LANGUAGES

English

PUBLICATIONS

International Journal Papers

Delihacıoğlu, K., Uçkun, S., Ege, T. (2007). Frequency selective surfaces comprised of periodic arrays of two–turn square spiral shaped conductors. *Int. J. Electron. Commun. (AEÜ)*, 61, 3, 182–185

Delihacıoğlu, K., Uçkun, S., Ege, T. (2007). Scattering characteristics of FSS comprised of L–shaped and one–turn helix shaped conductors for TE and TM excitation. *Electrical Engineering*, 89, 3, 177–181

Delihacıoğlu, K., Uçkun, S., Ege, T. (2006). L–shaped frequency selective surfaces as conducting elements on chiral slab. *Journal of Optoelectronics and Advanced Materials*, 8, 4, 1398–1401

Delihacıoğlu, K., (2003). Meander-line Polarizer on a chiral slab (transverse electric case). *Electrical Engineering*, 85, 5, 241-245

Delihacıoğlu, K., Uçkun, S. (2003). Power reflection and transmission coefficients for Meander–Line polarizers with a chiral slab. *ETRI Journal*, 25, 1, 41–48

International Conference Papers

Delihacıoğlu, K., Uçkun, S., Ege, T. (2006). FSS comprised of one– and two–turn square spiral shaped conductors on dielectric slab, *IVth International Workshop on Electromagnetic Wave Scattering*, September 18–22, Gebze, Turkiye

Delihacioğlu K., Uçkun, S. (2002). Power reflection and transmission coefficients for meander-line polarizer with chiral slab, *NATO Advanced Research Workshop, BIANISOTROPICS 2002, 9th International Conference on Electromagnetics of Complex Media*, Marrakech, Morocco

Delihacioğlu, K., Uçkun, S. (1998). Calculation of reflection and transmission powers of chiral slab for TE and TM wave excitations, *8th International Crimean Microwave Conference*, Sevastopol State Technical University, Crimea, Ukraine

National Conference Papers

Delihacıoğlu, K., Uçkun, S., Ege, T. (2006). Bakışımsız levhaya periyodik konulan şerit ve L–şeklindeki metal iletkenlerin Frekans Seçici yüzey olarak kullanımı, *URSI–TÜRKİYE 2006* Hacettepe Üniversitesi, Ankara

Delihacıoğlu, K., Uçkun, S., Ege, T. (2005). L–şeklindeki ve bir döngü biçimindeki frekans seçici yüzeylerin saçılma karakteristikleri, *Elektrik–Elektronik–Bilgisayar Mühendisliği 11.Ulusal Kongresi*, YTU, İstanbul

Delihacıoğlu, K., Uçkun, S., Ege, T. (2004). Dielektrik levha üzerine periyodik olarak yerleştirilen kare helezonların akım dağılımının bulunması. *URSI 2.Ulusal Kongresi*, Bilkent Üniversitesi, Ankara

Delihacioğlu, K., Uçkun, S. (2002). Bakışımsız levhada menderes bicimli polarizor, *URSI-TURKİYE'2002, 1. Ulusal Kongresi*, ITU, Istanbul

Delihacioğlu, K., Uçkun, S. (2002). TE modu için bakışımsız levhada menderes-biçimli polarizörün yansıma ve geçme güç katsayıları, *ELECO 2002, Elektrik-Elektronik-Bilgisayar Mühendisliği Sempozyumu*, Bursa

Delihacioğlu, K., Uçkun, S. (1999). Bakışımsız levhadan yansıma ve iletim güç katsayılarının bulunması, *Elektrik-Elektronik-Bilgisayar Muhendisligi 8. Ulusal Kongresi*, Gaziantep Universitesi, Gaziantep